Micro-chaos in digitally controlled mechanical systems

PhD dissertation written at the Department of Applied Mechanics,
Budapest University of Technology and Economics
Under the supervision of Dr. Gábor Csernák

MICRO-CHAOS IN DIGITALLY CONTROLLED MECHANICAL SYSTEMS

PhD dissertation

Gergely Gyebrószki

Supervisor: Dr. Gábor Csernák
Department of Applied Mechanics,
Budapest University of Technology and Economics

2018, Budapest

this page is intentionally left blank

To my wonderful wife Gitta,
and my curious son Lóci

this page is intentionally left blank

Acknowledgements

First, I would like to express my gratitude to my supervisor *Dr. Gábor Csernák* for his patience, motivation, immense knowledge and ability to overcome my occasional habit of procrastination. His guidance helped me in all the time of research and writing of this thesis. His words often inspired me which was an invaluable aid in more difficult moments.

Besides my supervisor, I would like to thank to *Prof. Gábor Stépán*, for his inspirative power during my BSc and MSc studies and his encouragement to pursue the PhD degree.

I also thank *my colleagues* at the Department of Applied Mechanics for the stimulating discussions of various research and educational topics, which often incented me to widen my perspectives, and for all the fun we have had in the last few years.

Last but not the least, I would like to thank *my wife, Gitta*, for supporting me spiritually throughout the writing of this thesis and during our life together in general.

Contents

Abstract

This dissertation aims to collect and present the most significant results in the field of *micro-chaos*, discovered during my years of pursuing the PhD degree.

Briefly, *micro-chaos* is a phenomenon, when a combination of digital effects – like sampling, rounding and delay – cause small amplitude chaotic oscillations, often resulting in multiple disconnected chaotic attractors or chaotic oscillations superposed on a recurrent orbit. This dissertation is restricted to simple digitally controlled mechanical systems with sampling and quantization. The effect of processing delay is not examined.

Chapter 1 presents the past and current state of the corresponding research area which served as an entry point for my own research.

Chapter 2 gives an overall picture about the 2D micro-chaos map corresponding to a digitally controlled 1-DoF mechanical oscillator. Various properties are shown and a simple classification of the possible cases is presented. Finally, certain results are generalized to multi-DoF systems.

Chapter 3 introduces an extension to the Simple Cell Mapping method, which allows adaptive expansion of the analysed state space region along with the opportunity of parallel execution.

Chapter 4 analyses the effect of twofold quantization: when both the input and output of the digital controller are affected by rounding.

Chapter 5 formulates the hybrid-switching micro-chaos map that describes the effect of dry friction on the motion of a 1-DoF digitally controlled oscillator. Besides the quantization-related switching events – that happen at the sampling instants – the friction-related switching events are also incorporated in the model that can be extended to the consideration of impact-like events, too.

Before proceeding, I would like to thank You, dear Reader, for taking the time to look into this work, I greatly appreciate any response or ideas regarding the concepts within this dissertation and those beyond.

1

Introduction

This chapter provides a brief overview of the research field of digitally controlled systems. These systems often can be modeled by piecewise smooth maps and specifically, by the so-called *micro-chaos map*. Control engineers usually handle the systems described by these maps in the frequency domain, while mathematicians do their examinations in the time domain, but often without connection to a real-world problem. From my *engineering* point of view, the goal would be to bring the best of both worlds together. The following sections introduce some key publications and present their fundamental results.
First, different approaches to describe quantization and sampling are listed, then the one-dimensional micro-chaos map is introduced. The focus is then shifted towards micro-chaos maps in higher dimensions and some key numerical approaches are shown, which are frequently used in the analysis of such maps.

1.1 Various approaches to the description of digital effects

In the past 50 years, with the appearance of digital electronic devices, a new challenge was introduced in the field of control engineering and computational science: dealing with the so-called *digital effects*.

The main digital effects are sampling, delay and quantization. Sampling arises from the fact, that processors operate in a periodic manner, they process one operation per cycle. Since the computation of control feedback takes time, processing delay between signal measurement and control effort output is unavoidable. Integer and floating-point numbers in computers are mostly represented in finite amount of bits, therefore they have a given precision, which leads to rounding (or with a more technical term, quantization) in calculations. Furthermore, many digital components like converters and filters can introduce one or more of these digital effects. For example, an analog-to-digital converter (ADC) can be treated as a composition of a quantizer and a sampler.

It is important to note, that *digital effects* also appear in many real world systems indirectly. In several applications, human-work related operations happen in a non-continuous manner – usually periodically – during the working hours. Similarly, many real world concepts and devices exhibit quantization. Consider the Kerr dam (Montana, US, see Fig. 1.1), which is adjusted one or two times daily and has 14 doors to let the water flow through. From the viewpoint of water throughput this is a sampled and quantized system. Quantization and

Figure 1.1: The Kerr Dam as an example of real-world sampling and quantization, image source: Wikipedia, EN: Kerr Dam *article.*

sampling also appears in logistics due to fixed schedule and size of trucks or package boxes. These "digital" effects can occur at several levels in financial systems, too: the stock market opens in fixed time intervals, companies announce earnings and pay dividends in a periodic manner and the shares represent quantization of value. In this case, a secondary digital effect, the quantization of currencies can be also found which resembles to the quantization of floating point numbers in computers.

In control engineering, one of the most significant books – Widrow and Kollár [52] – provides a sophisticated way to deal with sampling and quantization in the frequency domain. The book develops the *theory of quantization* analogously to the sampling theory, and focuses on uniform quantization. The statistical analysis of quantization leads to the *Pseudo Quantization Noise* (PQN) model. Various properties and application conditions of the PQN model are discussed in details. The recovery of original signal properties from quantized signals and analysis of quantization in feedback systems are discussed. The book also covers floating-point quantization and extends the corresponding quantization theory. Additionally, various examples of quantization in feedback control systems and filters are presented.

While the quantization theory offers a great way to analyse statistical properties of complex systems including analog-to-digital conversions or floating point calculations, chaos and chaotic systems are often easier to analyse in the time domain rather than in the frequency domain.

Mathematicians – Berkolaiko, Boyarsky, Góra, Domokos, see the citations in the upcoming paragraphs – studied quantized and sampled systems as piecewise linear or nonlinear maps, often with hysteresis. Many fundamental properties and intricate details of these maps have been elaborated, but corresponding practical applications are often not included and sometimes hard to find.

G. Berkolaiko analysed piecewise linear maps with hysteresis (PLMH) [2] and examined their basic properties (continuity, topological expansivity, discontinuity points and sets), proved the existence of a global attractor and formulated several theorems corresponding to the limit sets of these maps. Many of these results were later found to be in close resemblance to the results of G. Csernák in [8], see Figure 1.2.

P. Góra, A. Boyarsky and M. Jabłoński [32, 38] thoroughly studied one dimensional maps exhibiting chaotic behaviour, introduced an algorithm to control chaos [32], examined round-off errors introduced by computers and questioned the fact of often treating it as random noise [31]. They have provided in-depth studies about invariant measures for piecewise smooth maps and in general, the existence of such measure(s).

G. Domokos and D. Szász thoroughly studied the effects of rounding introduced by computers in numerical simulation of chaotic maps [20]. They have proposed an approach to

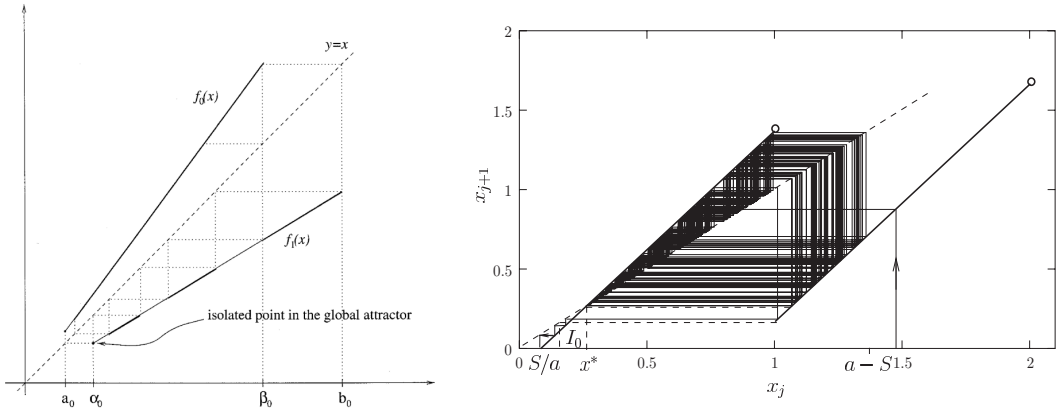

Figure 1.2: Two very similar piecewise linear maps with chaotic oscillations. Left: *Global attractor of a PLMH, taken from the paper of Berkolaiko [2].* Right: *Long transient chaotic trajectory of a micro-chaos map, taken from the paper of Csernák and Stépán [8].*

compute invariant measures of chaotic systems, which, in general cannot be preserved due to the fact, that simulations generate only a finite set with finite period. The effect of this secondary quantization was also found by G. Csernák in [6].

Cs. Budai, L. Kovács, J. Kövecses and G. Stépán [3] examined the stabilization effect of Coulomb-friction in an otherwise unstable mechanical system with digital control and sampling. They present a qualitative picture of the time history of the corresponding vibrations (concave envelope curve) which can be recognized in position control applications. Limit cycles, thorough stability analysis and experimental validation is also presented.

As it can be seen, there were many opportunities for mechanical engineers to gain ideas from analytical and numerical approaches used by control engineers and mathematicians during the analysis of computer-controlled systems. Several researchers focused on simple mechanical models – low degree of freedom linear oscillators – since the qualitative results could be generalized to more realistic cases. Moreover, digital effects can be analysed and algorithmic approaches can be developed effectively using simple mechanical systems. An invaluable benefit of this approach is that the solution of the linear equation of motion can be determined analytically. In these cases, the consideration of sampling and quantization leads to a piecewise linear map: the *micro-chaos map*.

1.2 The 1D micro-chaos map

The term *micro-chaos* (or μ-chaos) was first introduced by G. Stépán in 1994, then examined by G. Haller [33] and E. Enikov [21] (who were his PhD students at that time). They found that digital effects (sampling, rounding and delay) can lead to very small amplitude – hence the *micro* prefix – chaotic oscillations.

Few years earlier D.F. Delchamps [18] also made similar observations during the analysis of control strategies for linear systems with quantized state feedback. He found that quantized feedback systems behave chaotically and his quantitative statistical analysis revealed the existence of an invariant probability measure on the state space.

The first results showing micro-chaotic behaviour opened up a new perspective in control engineering. In many cases, computer control was designed with an analog model in mind. From a mechanical engineering point of view, digital effects often seemed to be negligible

due to their high frequency (in case of sampling) or small amount (of delay and round-off). However, it turned out that these slight digital effects can lead to a completely unexpected state space configuration with several coexisting chaotic attractors or repellors.

In [33] a simple stick-slip control system is analysed ($C = 0$, $\omega_0 = 0$ case of the polishing model in Fig. 1.3.), where the quantization of the velocity measurement and sampling with zero-order-hold leads to the 1D *micro-chaos map*:

$$y_{i+1} = a\, y_i - b\, \mathrm{Int}(y_i), \qquad i = 1, 2, \ldots . \tag{1.1}$$

The *micro-chaos map* is composed of the solution of the equation of motion at sampling time instants (denoted by i) and quantization of the state variable appears in the form of the $\mathrm{Int}(y_i)$. Only the relative velocity y at the contact is measured and controlled in the model, while the position is assumed to vary according to the controlled velocity. The instability of the uncontrolled system in the $y = 0$ state follows from the velocity-weakening characteristic of the friction coefficient.

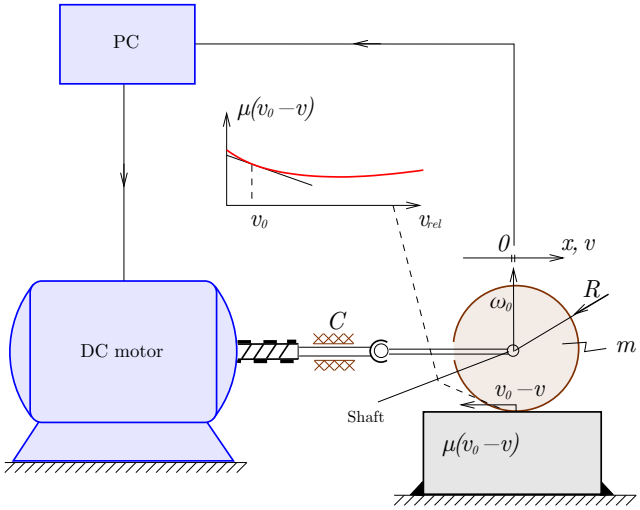

Figure 1.3: Polishing model used as an example for micro-chaos, taken from the paper of Csernák and Stépán [8]. C denotes the maximal dry friction force, ω_0 is the angular velocity of the polishing disk of radius R, v is the feed rate and $v_0 = \omega_0 R$.

Here, and throughout the dissertation, $\mathrm{Int}(x)$ denotes the integer part function[1], that is, a mid-tread, double-deadzone quantization, see Fig. 1.4. The different possible values taken by the integer part function correspond to different control efforts.

G. Haller and G. Stépán provided a mathematical proof in [33] for the chaotic nature of the 1D micro-chaos map: the sensitive dependence on initial conditions was shown, the existence of an attractive invariant set was presented, and it was proven, that the micro-chaos map is topologically transitive on the set. Parameter domains were given, for which the attracting set is a hyperbolic strange attractor. It was highlighted, that micro-chaos can cause relatively large static errors in positioning.

[1]Of course, there are many different rounding functions; e.g., rounding directly to an integer, up, down, towards zero or towards infinity, or rounding to the nearest integer instead in a similar fashion (upwards, downwards, to zero or to infinity). One could even analyse a shifted rounding function to reflect asymmetries in real measurement situations. The advantages of using the double-deadzone mid-tread variant are its symmetry and largest possible deadzone.

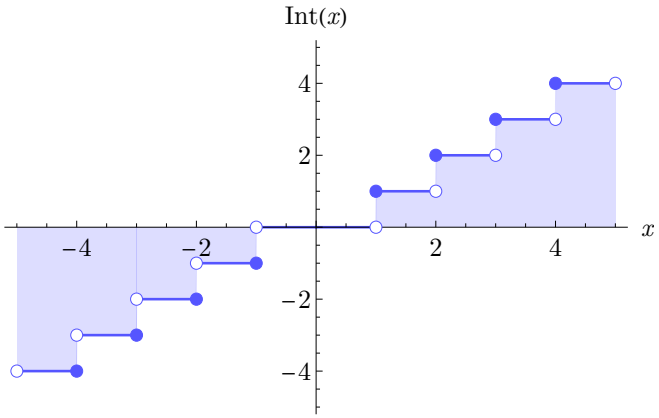

Figure 1.4: Integer part function, rounding towards zero. (Mid-tread, double-deadzone quantization.)

In realistic situations, the chaotic motion of a dynamical system usually disappears after a sufficiently long time. This phenomenon – the *transient chaos* – differs from sustained (or permanent) chaos by having a finite lifetime [42]. The variation of parameters may turn a chaotic system to a transient chaotic one via a crisis bifurcation. During this event, the chaotic attractor opens up and loses its global attracting property, i.e., trajectories are allowed to escape from it after a finite-time chaotic motion – this is why the remaining strange set is referred to as a *repellor*. Since the probability of finding the system in the chaotic state (in the repellor) decreases exponentially in time, the lifetime of transient chaos is characterised by the corresponding exponent, the *escape rate*.

In works of G. Csernák, transient chaos is thoroughly examined when friction is added to the previously mentioned stick-slip model. The escape rate and mean lifetime are estimated based on the fractal dimension of the repellor [12]. A recursive procedure for life expectancy (mean kickout number) calculation was also provided in [8, 13]. Again, these results can be clearly correlated to results obtained in the field of mathematics, see Fig. 1.5.

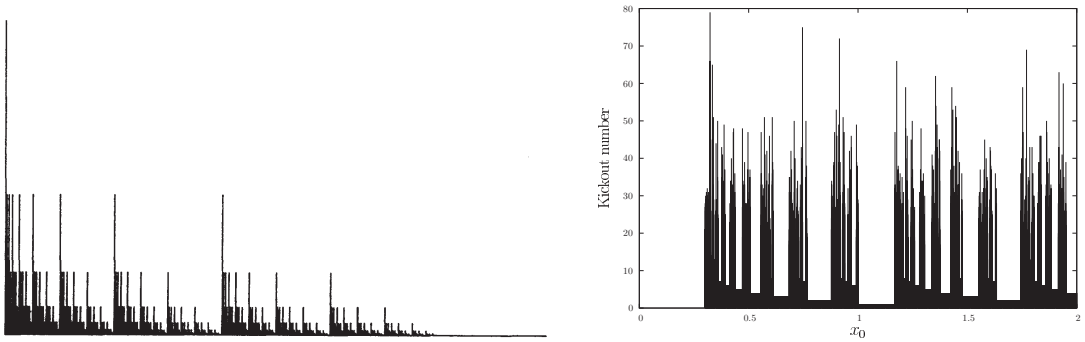

Figure 1.5: Invariant sets of piecewise smooth maps. Left*: globally attractive set (probability density vs. initial state), taken from the paper of Jabłoński et al. [38].* Right*: transient chaotic repellor (kickout number vs. initial conditions), taken from the paper of Csernák and Stépán [12].*

1.3 Micro-chaos map in higher dimensions

From practical point of view, micro-chaos maps corresponding to multi degree of freedom systems are more important compared to the one-dimensional case. These maps, however, are more challenging to analyse, starting from the visualisation of trajectories and invariant sets to the proof of certain properties.

The two-dimensional micro-chaos map obtained by taking processing delay into account was first presented by G. Csernák [9] using some of the formalism from [21]:

$$\begin{bmatrix} y_i \\ y_{i+1} \end{bmatrix} = F\left(\begin{bmatrix} y_{i-1} \\ y_i \end{bmatrix}\right) = \begin{bmatrix} y_i \\ a\,y_i - b\,\mathrm{Int}(y_{i-1}) \end{bmatrix}. \tag{1.2}$$

Note, that similarly to Eq. (1.1), y is related to the velocity of the 1DoF oscillator. Fundamental properties of the 2D micro-chaos map (1.2) were shown: fixed points and basic branches of the map were identified and chaos was proven by separately proving the following statements:

- The map has sensitive dependence on initial conditions.
- A so-called absorbing state-space domain (absorbing sphere) exists, from where solutions cannot leave after they enter. For the proof of chaos, finding an absorbing sphere is necessary since a strange attractor must reside inside the absorbing sphere.
- The dynamical system, described by Eq. (1.2) is topologically transitive. This property means that the attractor can be partitioned in an irreducible way and every partition can be reached from any other partition, having at least one, whose image fully covers at least two other partitions. (Or shortly, trajectories withing the attractor are *mixing*.)

It is worth noting, that mapping (1.2) can be also considered as a piecewise linear map with hysteresis, see Fig. 1.6. Recall, that G. Berkolaiko [2], and B. Garay, R. Csikja and J. Tóth [22] studied similar maps.

In [10], a 2D micro-chaos map corresponding to a PD-controlled inverted pendulum was introduced and analysed. The map is formulated as

$$\mathbf{y}_{i+1} = \mathbf{U}\,\mathbf{y}_i + \mathbf{b}\,\mathrm{Int}(\mathbf{k}\,\mathbf{y}_i), \quad \text{where} \tag{1.3}$$

$$\mathbf{U} = \begin{bmatrix} \mathrm{ch}(\beta) & \mathrm{sh}(\beta)/\beta \\ \beta\,\mathrm{sh}(\beta) & \mathrm{ch}(\beta) \end{bmatrix}, \quad \mathbf{b} = \begin{bmatrix} (1-\mathrm{ch}(\beta))/\beta^2 \\ -\mathrm{sh}(\beta)/\beta \end{bmatrix}, \quad \mathbf{k} = \begin{bmatrix} P \\ D \end{bmatrix}, \quad \mathbf{y}_i = \begin{bmatrix} y_i \\ y_i' \end{bmatrix},$$

y_i is the dimensionless angular position, y_i' is the angular velocity, β is the characteristic constant corresponding to the negative stiffness, while P and D are control parameters. The image of a strange attractor spanning over multiple control effort bands in the state space is shown in Fig. 1.7. As it can be seen, the control effort $m \equiv \mathrm{Int}(\mathbf{k}\,\mathbf{y}_i)$ assumes different values in parallel bands of the phase-plane.

In [21], E. Enikov and G. Stépán presented the analysis of a pendulum-on-a-cart model which yields the following 3D micro-chaos map:

$$\mathbf{y}_{i+1} = \mathbf{U}\,\mathbf{y}_i + \mathbf{b}\,\mathrm{Int}(\mathbf{k}\,\mathbf{y}_i), \quad \text{where} \tag{1.4}$$

$$\mathbf{U} = \begin{bmatrix} \mathrm{ch}(\beta) & \mathrm{sh}(\beta)/\beta & (\mathrm{ch}(\beta)-1)/\beta^2 \\ \beta\,\mathrm{sh}(\beta) & \mathrm{ch}(\beta) & \mathrm{sh}(\beta)/\beta \\ 0 & 0 & 0 \end{bmatrix}, \quad \mathbf{b} = \begin{bmatrix} 0 \\ 0 \\ -\gamma \end{bmatrix},$$

$$\mathbf{k} = \begin{bmatrix} P \\ D \\ 0 \end{bmatrix}, \quad \mathbf{y}_i = \begin{bmatrix} y_i \\ y_i' \\ P y_{i-1} + D y_{i-1}' \end{bmatrix}.$$

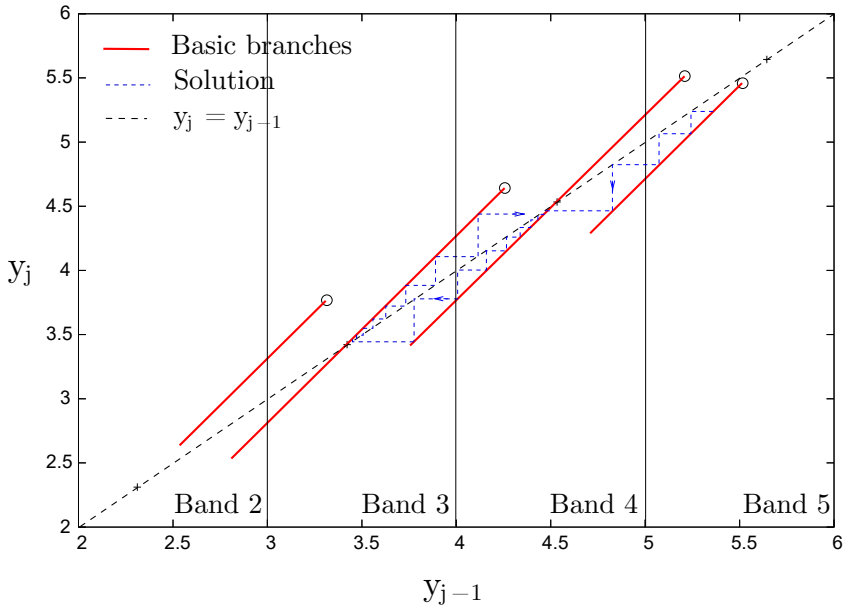

Figure 1.6: Repellor of the 2D micro-chaos map (1.2), taken from the paper of Csernák and Stépán [8]. The domain of definition is divided into parallel bands, according to the value of the control effort.

β is, again, the characteristic constant corresponding to the negative stiffness, γ is a system parameter characterising the mass distribution, while P and D are control parameters. The effect of processing delay is also considered in the model, this is why the control effort appears in the state vector $\mathbf{y}_i$, besides the dimensionless angular position y_i and angular velocity y_i'. A detailed analysis is provided, including the existence of an absorbing sphere and an invariant set, to the proof of sensitivity on initial conditions. Topological transitivity was not proven, but from a practical point of view one can use a naive, less strict definition of chaos, which does not require the topological transitivity. One could also argue that a really long periodic orbit cannot be distinguished from chaotic behaviour in real applications. The chaotic attractor of Map (1.4) is shown in Figure 1.8.

In [14], the generalisation of micro-chaos maps for digitally controlled linear systems with arbitrary feedback with or without delay and zero order hold control is introduced. The so-called *state-space model of micro-chaos* is formulated, and several configurations of digital effects – e.g., sampling with rounding at the input (measured state) and/or output (control effort) of the controller, with or without additional processing delay – are presented. Dependence on one or more past state variables can be used to formulate multiple delays, or numerical derivatives. It was shown that the behaviour of the considered class of systems can be given in the form

$$\mathbf{y}_{i+1} = \mathbf{U}\,\mathbf{y}_i + \mathbf{d}_i, \tag{1.5}$$

where $\mathbf{U}$ corresponds to the original, unstable, uncontrolled dynamics and $\mathbf{d}_i$ is the control effort influenced by digital effects. Map (1.5) – the generalized micro-chaos map – can be reformulated as

$$\mathbf{y}_{i+1} = \mathbf{S}\,\mathbf{y}_i - \mathbf{c}_i, \tag{1.6}$$

where $\mathbf{S}$ corresponds to stable, controlled dynamics of the system without quantization, and $\mathbf{c}_i$ is a correction term representing quantization.

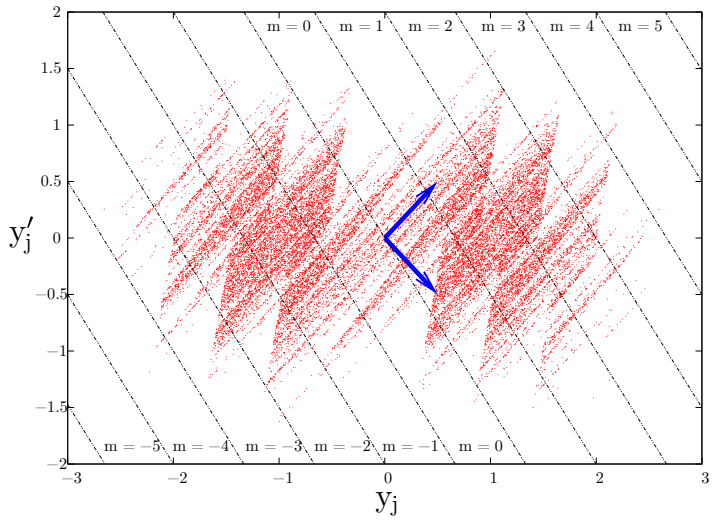

Figure 1.7: Chaotic attractor spanning over multiple bands that are separated by switching lines; taken from the paper of Csernák and Stépán [10].

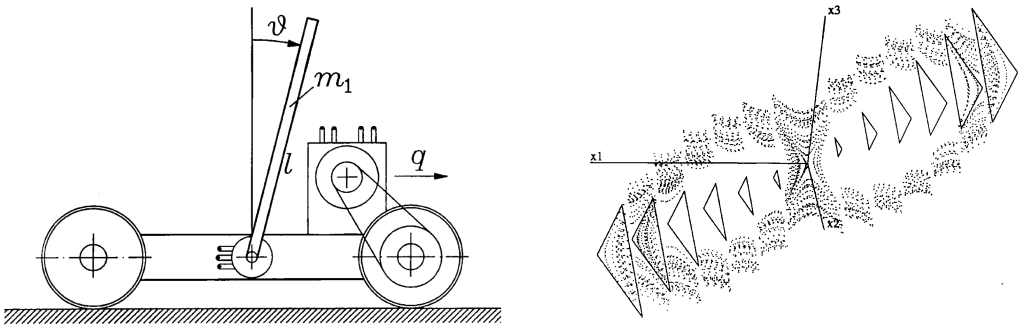

Figure 1.8: Left*: Pendulum-on-a-cart, whose equation of motion leads to a 3D micro-chaos map.* Right*: chaotic attractor in the state space of Map (1.4), taken from the paper of Enikov and Stepan [21].*

Formula (1.5) emphasizes the small-scale, locally unstable behaviour of the trajectories, while the globally stable behaviour of the controlled system is better described by (1.6).

This statement is illustrated with Fig. 1.9 that shows the large-scale and small-scale dynamics of a 1D micro-chaos map (1.1).

At every point of the phase-space, the matrix $\mathbf{U}$ is the coefficient matrix of the locally linearized micro-chaos map. Consequently, for this class of maps the *Lyapunov exponents* can be directly calculated as the eigenvalues of matrix $\mathbf{U}$, allowing one to quickly determine the sensitivity on initial conditions.

Similarly to the result obtained by Enikov and Stépán [21], one can also express the *maximum error* introduced by the map, which yields the size of the smallest absorbing sphere. Since the maximum error is a global property of the map, it can be conveniently expressed based on formula (1.6):

$$\|\mathbf{y}_\infty\| = \max_{\mathbf{c}_i} \left\| \sum_{i=0}^{\infty} \mathbf{S}^i \, \mathbf{c}_i \right\| = \max_{\chi_i} \left\| \sum_{i=0}^{\infty} \mathbf{S}^i \, \mathbf{b} \, \chi_i \right\|, \qquad \chi_i \in (-1, 1). \tag{1.7}$$

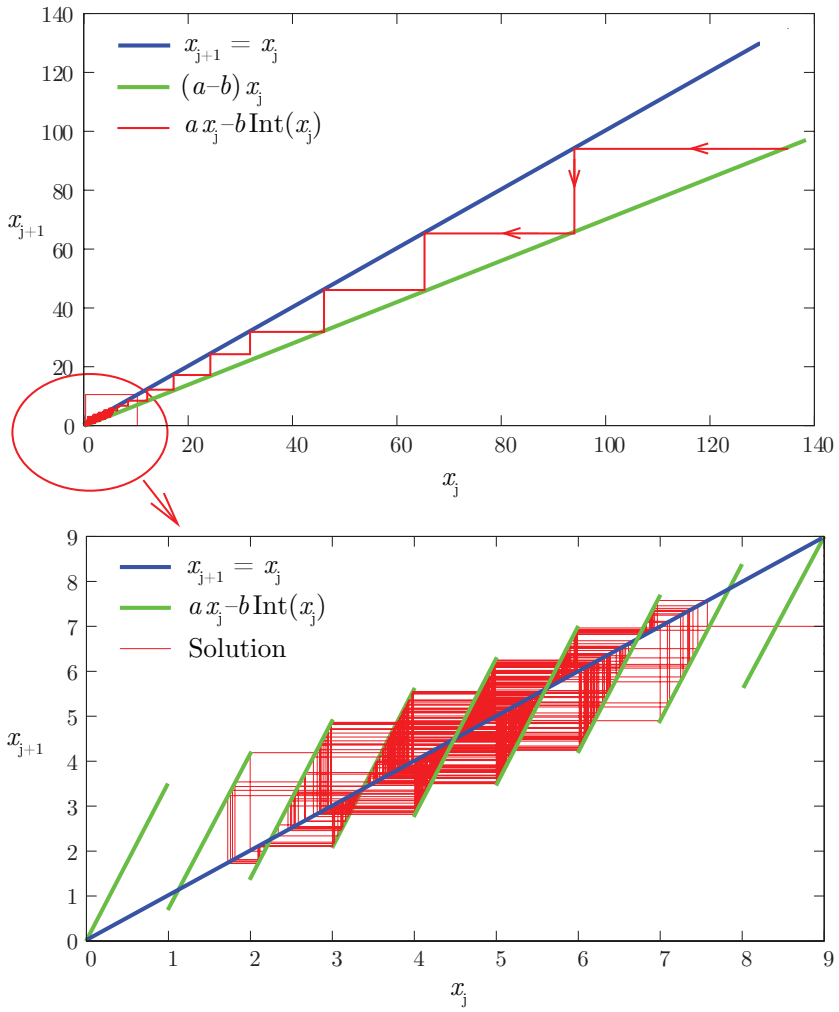

Figure 1.9: The large-scale and small-scale behaviour of the 1D micro-chaos map at $a = 3.5$ *and* $b = 2.8$.

Here χ_i denotes the neglected fractional part during quantization, while vector $\mathbf{b}$ characterizes the effect of the control effort on the state variables – see Eqs. (1.3) and (1.4).

As it will be shown in Chapter 2, the calculation of $\|\mathbf{y}_\infty\|$ is often rather challenging due to the non-normality of the coefficient matrix $\mathbf{S}$.

1.4 Characterisation of micro-chaos

During the analysis of micro-chaos maps, the usual goal is to determine the following properties and locate the following state space objects:

- largest Lyapunov exponent to determine the sensitivity on initial conditions,
- topological transitivity that is related to the mixing property,
- absorbing region (absorbing sphere) in the state space, whose size corresponds to the maximal control error, after transients are settled,
- periodic orbits (and as a 1-periodic case, fixed points),
- topological entropy,
- chaotic attractors and/or repellors and their properties (e.g., fractal dimension).

Many of the above tasks are not trivial to carry out analytically, therefore a set of numerical methods is frequently used.

It is important to note, that in case of the micro-chaos maps presented in this dissertation, the only non-linearity is originated from the quantization and otherwise the solution of the equation of motion is known.

Lyapunov exponents can be directly calculated as they are the eigenvalues of matrix $\mathbf{U}$, see Equation (1.5).

Topological transitivity shows the mixing of trajectories on the invariant set (attractor). It is required for having chaotic behaviour according to the most accepted definition [19]. For the proof of topological transitivity, a non-trivial partitioning of the state space is usually necessary, along with the introduction of a symbolic dynamics.

Periodic orbits can be found using symbolic dynamics, where the alphabet of symbols corresponds to the quantized values of control efforts. The application of this method is described in Section 2.4.3. An important property of chaotic systems is that many physical properties can be efficiently averaged on the unstable periodic orbits [15].

Topological entropy shows the growth of the number of periodic orbits with increasing period. In [5], the topological entropy is calculated using an algorithm which analyses the pre-images of line sections taken from the vicinity of the invariant set. Topological entropy can also be determined by simply counting the number of periodic orbits, moreover – in some metric spaces – it is directly related to topological transitivity.

The size of the *absorbing region or absorbing sphere* can be formulated using Eq. (1.7) which estimates the total amount of error introduced by digital effects in the map. It was shown in [7] that the infinite series is convergent and yields the radius of the absorbing state space region. The challenging part is, however, to determine the proper combination of fractional parts ($\mathbf{c}_j$) which maximize the series. The suggested solution to this problem is described in Section 2.4.2.

Fractal dimension of chaotic attractors can be calculated by the traditional *box counting* method [15], or using time series analysis [34].

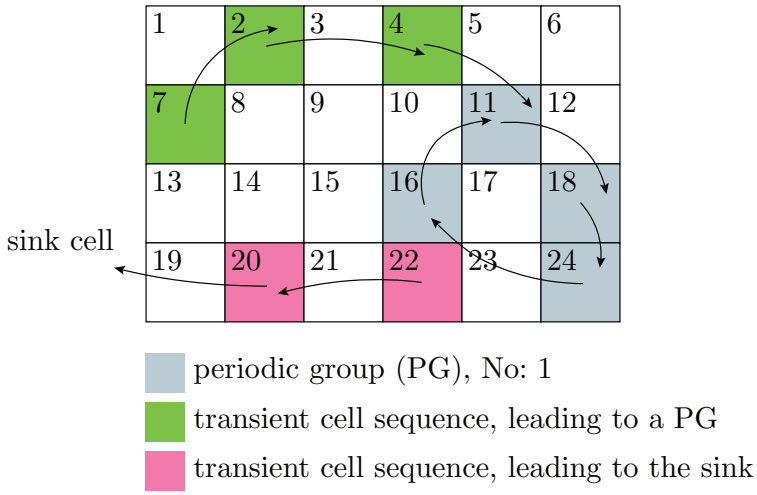

Figure 1.10: Illustration of simple cell mapping.

State space objects can be reliably discovered by Cell Mapping methods [35]. Simple Cell Mapping (SCM) is able to find fixed points and periodic orbits in a selected state space region, along with their basins of attraction. In SCM, the state space is discretized; divided

into cells, as shown in Fig. 1.10. For every cell a single image cell is determined, where the dynamics lead from the center point of the cell.

Following the images of cells, one can formulate a graph, which contains cycles (periodic cell groups) and transient cell sequences leading to either a periodic group or to the area outside the analysed domain – the sink cell. Chaotic attractors or repellors are usually covered by one or more high period cell groups [35].

2

The micro-chaos map

This chapter introduces the micro-chaos map corresponding to a single degree-of-freedom digitally controlled mechanical oscillator. Two digital effects – sampling and quantization – are taken into account: sampling *converts* the continuous flow to a 2D map and quantization results in piecewise smooth control efforts.
The general classification of 2D micro-chaos maps is presented and the case of negative stiffness oscillators with quantization on the control effort is thoroughly analysed. Finally, certain results are generalized to multi degree-of-freedom cases.

Throughout this chapter, a restriction is made to the digitally controlled oscillator with linearized equation of motion. The digital controller will implement a feedback control with proportional and derivative terms (shortly PD-control), with sampling and zero-order-hold, i.e., the calculated control effort will be kept constant between two sampling instants (see Fig. 2.1). Another frequently occuring digital effect – the processing delay – is not considered in this chapter. The assumption is made, that measuring certain state variables, calculating the control effort and governing the actuator takes negligible amount of time.

While the aforementioned restrictions could seem to be strict, these assumptions allow one to see a qualitative picture of the effect of sampling and quantization. Since the solution of linear systems are known analytically, the only non-linear term comes from the quantization. The restriction to PD-control has an advantage of having control terms corresponding to the stiffness and damping in the system. Lastly, the state space of two-dimensional maps can be represented conveniently by several numerical methods and is easy to illustrate or show in figures.

2.1 The digitally controlled 1 DoF mechanical oscillator

2.1.1 Solution of the equation of motion

As a consequence of the sampling and zero-order-hold control scheme, the control effort assumes constant values between the subsequent sampling instants. In the present section, the equations of motion and the solutions are formulated for three different linear oscillators under a constant external force. These results provide the basis for the derivation of the corresponding micro-chaos maps by taking into account the digital effects.

Consider the equation of motion of the 1 DoF oscillator with a linear spring and viscous damping and constant external force (see Fig. 2.1):

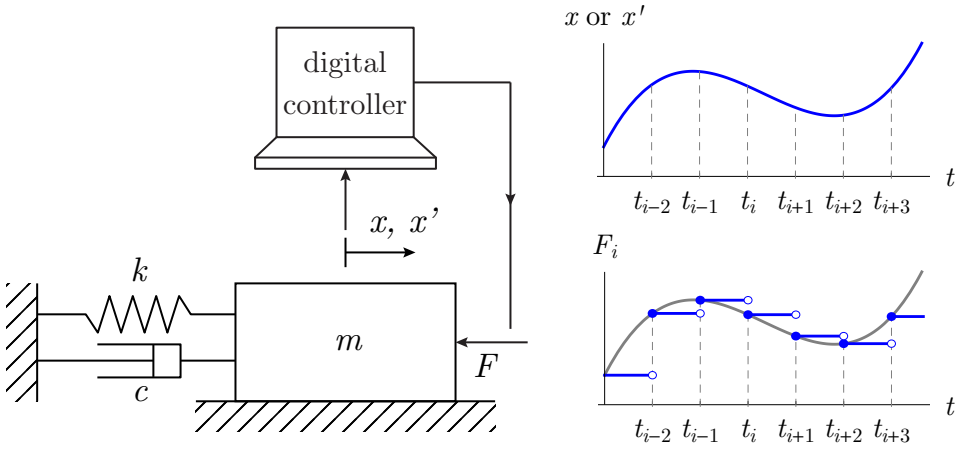

Figure 2.1: One degree-of-freedom mechanical oscillator with digital control. The effect of sampling and zero-order hold is illustrated on the right subfigures.

$$\ddot{x}(t) + 2\,\delta\,\alpha\,\dot{x}(t) + \alpha^2\,x(t) = -F, \quad t \in [i\tau, (i+1)\tau), \tag{2.1}$$

where $\alpha = \sqrt{k/m}$ is the natural angular frequency, $\delta \in [-1, 1]$ is the damping ratio ($2\,\delta\,\alpha = c/m$) and $-F$ is a control effort betwen the i^{th} and $(i+1)^{\text{st}}$ sampling instants. The sampling period is denoted by τ. Rewriting the system as a set of first order differential equations, one can obtain

$$\dot{\mathbf{y}}(t) = \mathbf{A}\,\mathbf{y}(t) + \mathbf{f}, \tag{2.2}$$

where

$$\mathbf{y}(t) = \begin{bmatrix} x(t) \\ \dot{x}(t) \end{bmatrix}, \quad \mathbf{A} = \begin{bmatrix} 0 & 1 \\ -\alpha^2 & -2\,\delta\,\alpha \end{bmatrix} \quad \text{and} \quad \mathbf{f} = \begin{bmatrix} 0 \\ -F \end{bmatrix}. \tag{2.3}$$

The solution of the equation of motion can be formulated as:

$$\mathbf{y}(t) = \mathbf{U}(t)\,\mathbf{y}(0) + \mathbf{b}(t)\,F, \quad t \in [i\tau, (i+1)\tau), \tag{2.4}$$

where

$$\mathbf{U}(t) = \frac{e^{-\delta\alpha t}}{\Gamma} \begin{bmatrix} \Gamma\cos(\alpha\Gamma t) + \delta\sin(\alpha\Gamma t) & \sin(\alpha\Gamma t)/\alpha \\ -\alpha\sin(\alpha\Gamma t) & \Gamma\cos(\alpha\Gamma t) - \delta\sin(\alpha\Gamma t) \end{bmatrix}, \tag{2.5}$$

$$\mathbf{b}(t) = \frac{1}{\alpha^2\Gamma} \begin{bmatrix} \Gamma - e^{-\delta\alpha t}\left(\Gamma\cos(\alpha\Gamma t) + \delta\sin(\alpha\Gamma t)\right) \\ \alpha\, e^{-\delta\alpha t}\sin(\alpha\Gamma t) \end{bmatrix},$$

and $\Gamma = \sqrt{1-\delta^2}$.

Equation (2.4) represents an operator between an initial condition $\mathbf{y}(0)$ and the solution of the system, for a constant control effort $-F$. Since sampling and zero-order-hold will result in constant control effort between two successive sampling instants, no other inhomogenities are considered.

Micro-chaos is expected to appear in cases when the trivial equilibrium of the uncontrolled system is unstable. This situation occurs if either the stiffness or the damping parameter becomes negative.

If the *stiffness* of the system is negative, Eq. (2.1) changes to

$$\ddot{x}(t) + 2\,\delta\,\alpha\,\dot{x}(t) - \alpha^2\,x(t) = -F, \quad t \in [i\tau, (i+1)\tau), \tag{2.6}$$

where $\alpha > 0$ characterizes the negative stiffness, and the corresponding elements of the solution are:

$$\mathbf{U}(t) = \frac{e^{-\delta\alpha t}}{\Gamma}\begin{bmatrix} \Gamma\cosh(\alpha\Gamma t) + \delta\sinh(\alpha\Gamma t) & \sinh(\alpha\Gamma t)/\alpha \\ \alpha\sinh(\alpha\Gamma t) & \Gamma\cosh(\alpha\Gamma t) - \delta\sinh(\alpha\Gamma t) \end{bmatrix}, \tag{2.7}$$

$$\mathbf{b}(t) = \frac{1}{\hat{\alpha}^2\Gamma}\begin{bmatrix} -\Gamma + e^{-\delta\alpha t}\left(\Gamma\cosh(\alpha\Gamma t) + \delta\sinh(\alpha\Gamma t)\right) \\ \alpha\, e^{-\delta\alpha t}\sinh(\alpha\Gamma t) \end{bmatrix},$$

where the definition of Γ changes to $\Gamma = \sqrt{1+\delta^2}$.

Note, that the corresponding matrix $\mathbf{U}(t)$ and vector $\mathbf{b}(t)$ can be derived for the case of zero stiffness, too [11].

If the *damping* of the system is negative, Eq. (2.1) changes to

$$\ddot{x}(t) - 2\,\delta\,\alpha\,\dot{x}(t) + \alpha^2\,x(t) = -F, \quad t \in [i\tau, (i+1)\tau), \tag{2.8}$$

where the damping ratio $\delta > 0$ characterizes the negative damping, and the corresponding elements of the solution are now:

$$\mathbf{U}(t) = \frac{e^{\delta\alpha t}}{\Gamma}\begin{bmatrix} \Gamma\cos(\alpha\Gamma t) - \delta\sin(\alpha\Gamma t) & \sin(\alpha\Gamma t)/\alpha \\ -\alpha\sin(\alpha\Gamma t) & \Gamma\cos(\alpha\Gamma t) - \delta\sin(\alpha\Gamma t) \end{bmatrix}, \tag{2.9}$$

$$\mathbf{b}(t) = \frac{1}{\alpha^2\Gamma}\begin{bmatrix} \Gamma - e^{\delta\alpha t}\left(\Gamma\cos(\alpha\Gamma t) - \delta\sin(\alpha\Gamma t)\right) \\ \alpha\, e^{\delta\alpha t}\sin(\alpha\Gamma t) \end{bmatrix},$$

and $\Gamma = \sqrt{1-\delta^2}$.

2.1.2 Stability of PD-controlled system with sampling but without quantization

If the trivial equilibrium of the oscillator is unstable (negative stiffness or damping cases, Eqs. (2.6)-(2.8)), a proportional-derivative control (or shortly PD-control) is frequently used to stabilize the equilibrium. Since quantization of control effort introduces a nonlinearity which would make stability analysis complicated, the case without quantization is used to obtain a reference stable parameter domain for the micro-chaos map. For the case with sampling and zero-order hold, the corresponding control force in the i-th sampling period is

$$F_i = (P\,x_i + D\,\dot{x}_i). \tag{2.10}$$

To carry out the stability analysis with respect to control parameters P and D, Jury's criterion (that follows from the Routh-Hurwitz criterion) [40] is applied to the sampled system (without quantization)

$$\mathbf{y}_{i+1} = \mathbf{S}\,\mathbf{y}_i, \qquad \mathbf{S} = \mathbf{U} + \mathbf{b}\otimes\mathbf{k}, \tag{2.11}$$

where $\mathbf{k} = [P \quad D]^{\mathrm{T}}$ and $\mathbf{y} = [x \quad \dot{x}]^{\mathrm{T}}$.

If the stiffness is negative, the coefficients of the characteristic polynomial yield the following conditions for the stability of the equilibrium at $x = 0$:

$$\begin{aligned} a_0: &\quad D < \frac{\Gamma\left(\alpha^2\sinh^{-1}(\alpha\delta)(\cosh(\alpha\Gamma) + \cosh(\alpha\delta)) + P\right) - \delta P}{\alpha}, \\ a_1: &\quad D > \frac{\Gamma\left(\left(P - 2\alpha^2\right) + P\sinh^{-1}(\alpha\delta)(\cosh(\alpha\Gamma) - \cosh(\alpha\delta))\right) - \delta P}{\alpha}, \\ a_2: &\quad P > \alpha^2. \end{aligned} \tag{2.12}$$

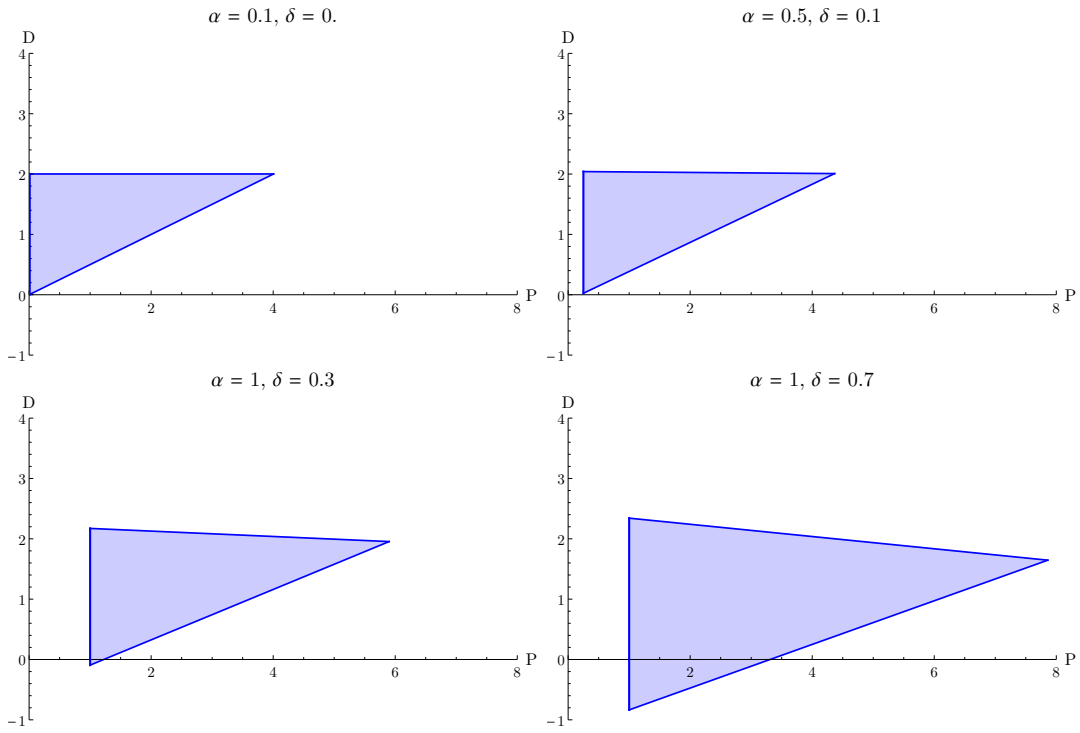

Figure 2.2: Stable parameter domains of the PD-control, in case of negative stiffness.

Conditions (2.12) can be used to illustrate the domain of stable control parameters, see Figure 2.2.

These stable parameter domains will be used as a reference during the analysis of micro-chaos, after taking digital effects into account. For switched systems of this type, the general observation is, that transient chaos appears at the boundary of stability [45, 50].
Throughout this chapter, the assumption is made, that for the global behaviour of micro-chaos maps, the non-quantized case provides a good reference for the domain of stable control parameters.

2.2 The 2D micro-chaos map and its classification

In this section, another digital effect is added to the sampled system: quantization. As it will be presented, the presence of two digital effects (sampling and quantization) will result in chaotic behaviour.

If sampling occurs, with sampling period τ, the following map describes the evolution of the oscillator:

$$\mathbf{y}((i+1)\,\tau) = \mathbf{U}(\tau)\,\mathbf{y}(i\,\tau) + \mathbf{b}(\tau)\,F_i(\mathbf{y}(i\,\tau)), \qquad i \in \mathbb{Z}. \tag{2.13}$$

Here F_i is the control effort calculated at the i^{th} sampling instant from $\mathbf{y}(i\,\tau)$. With re-scaling the time and using $T = t/\tau$, one arrives at the following map:

$$\mathbf{y}_{i+1} = \mathbf{U}(1)\,\mathbf{y}_i + \mathbf{b}(1)\,F_i(\mathbf{y}_i), \qquad i \in \mathbb{Z}. \tag{2.14}$$

In order to match the dimensionless time, the following parameters should be used in $\mathbf{U}$ and $\mathbf{b}$:

$$\hat{\alpha} = \alpha\tau, \quad \hat{P} = P\tau^2, \quad \hat{D} = D\tau. \tag{2.15}$$

Note, that $\hat{\alpha}$ is the composition of two characteristic time constants: the reciprocal of the characteristic time constant (or natural angular frequency in the case of positive stiffness) α and the sampling time τ.

Adding *quantization* (or in other word, rounding) to the control can be done in two ways.

- *Output quantization* is the case, when the calculated control effort (the output of the controller) is quantized with output resolution r_{O}. This means, that the rounding function Int is applied to the control effort F_i/r_{O}, then the result is multiplied with the resolution:

$$\mathbf{y}_{i+1} = \mathbf{U}(1)\,\mathbf{y}_i + \mathbf{b}(1)\,r_{\mathrm{O}}\,\mathrm{Int}\left(\frac{1}{r_{\mathrm{O}}}F_i(\mathbf{y}_i)\right), \qquad i \in \mathbb{Z}. \tag{2.16}$$

- *Input quantization* is the opposite case, when the measured state vector (the input of the controller) is subject to quantization with input resolution $r_{\mathrm{I,i}}$ for the i^{th} component of the state vector. The corresponding map assumes the form

$$\mathbf{y}_{i+1} = \mathbf{U}(1)\,\mathbf{y}_i + \mathbf{b}(1)\,F_i\left(\mathbf{R}_{\mathrm{I}}\,\mathrm{Int}\left(\mathbf{R}_{\mathrm{I}}^{-1}\,\mathbf{y}_i\right)\right), \qquad i \in \mathbb{Z}. \tag{2.17}$$

  Here $\mathbf{R}_{\mathrm{I}} = \mathrm{diag}(r_{\mathrm{I,1}}, r_{\mathrm{I,2}}, \ldots, r_{\mathrm{I,n}})$ is the diagonal matrix of input rounding resolutions.

Maps (2.16) and (2.17) are *micro-chaos maps* since their form corresponds to the formula (1.5). Of course, one can re-scale the space coordinates and therefore eliminate the resolution parameter r_{O} or r_{I}.

Before examining one of the micro-chaos maps in detail, a general classification for the 2D micro-chaos maps corresponding to the 1 DoF mechanical oscillator will be provided. The categorisation is made by the nature of instability and type of quantization, see Table 2.1.

Instability / Quantization	Output	Input	Input and output
Negative stiffness	A	B	
Negative damping	C	D	see Chapter 4.

Table 2.1: The classification of 2D micro-chaos maps with respect to the nature of instability and quantization.

By looking at the standard cases, four simple types of the 2D micro-chaos maps can be distinguished. The twofold quantization cases (when both the input and output are quantized) will be covered later, in Chapter 4. Cases with negative stiffness and negative damping fall back to the negative stiffness cases, as that type of instability dominates.

Although the methods described in this dissertation can be applied to broad classes of micro-chaos maps, most of the calculations were carried out for Case A. Therefore, the following section will focus on the negative stiffness, output quantization situation.

2.3 Inverted pendulum with control effort quantization

Applying the control scheme described by (2.16) to the linearized equation of motion of the inverted pendulum, one obtains

$$\ddot{\varphi}(t) + 2\delta\alpha\dot{\varphi}(t) - \alpha^2\varphi(t) = -r_O\,\mathrm{Int}\left(\frac{P\varphi(t_j)}{r_O} + \frac{D\dot{\varphi}(t_j)}{r_O}\right), \qquad j = 1, 2, \ldots, \tag{2.18}$$

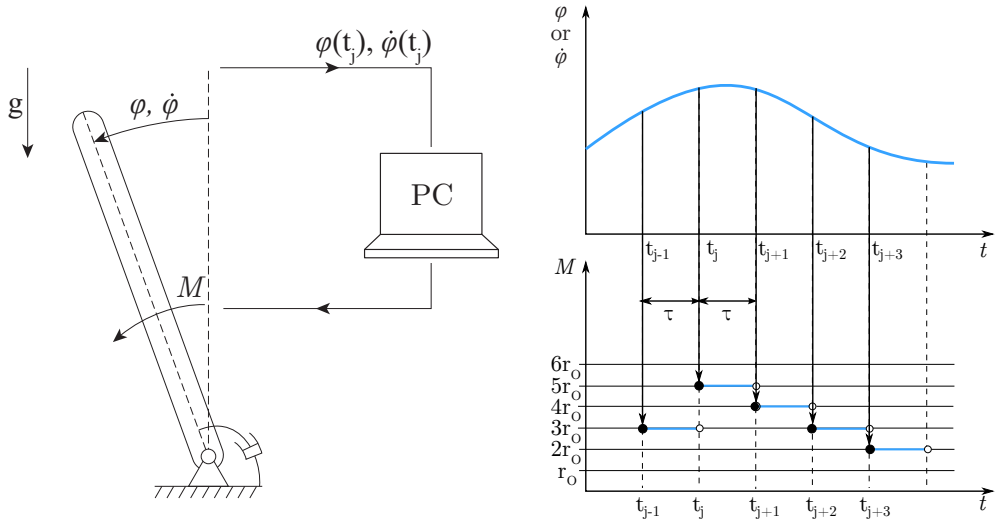

Figure 2.3: Illustration of sampling and quantization and a digitally controlled inverted pendulum.

where α is the inverse of the characteristic time constant that describes the uncontrolled inverted pendulum, δ is the relative damping, P and D are control parameters and r_O is the resolution of the control torque (see Figure 2.3). The rounding is taken into account with the Int() function, which denotes rounding towards the origin, according to Fig. 1.4. Introducing the dimensionless time $T = t/\tau$, system parameters $\hat{\alpha} = \alpha\,\tau$, $\hat{P} = P\,\tau^2$, $\hat{D} = D\,\tau$ and rescaled space coordinate $x = \varphi/(r_O\,\tau^2)$, the resolution parameter can be eliminated. Note, that parameter $\hat{\alpha}$ is the ratio of the sampling period and the characteristic time constant of the oscillator. Its value is usually kept very small in practical applications.

According to the solution of the linearized, dimensionless equation of motion (2.4), the following mapping can be derived between the states at subsequent sampling instants:

$$\begin{aligned} \mathbf{y}_{i+1} &= \mathbf{U}\,\mathbf{y}_i + \mathbf{b}\,F_i, \\ F_i &= \mathrm{Int}(\hat{P}x_i + \hat{D}x_i'), \end{aligned} \tag{2.19}$$

where $\mathbf{y} = [x_i \quad x_i']^T$, and – with the abuse of notation – $\mathbf{U} \equiv \mathbf{U}(1)$, $\mathbf{b} \equiv \mathbf{b}(1)$ from Eq. (2.7).

Equation (2.19) is the micro-chaos map corresponding to the negative stiffness and output quantization case (case A in Table 2.1).

2.3.1 Fixed points, switching lines and topological pattern

Looking at the state space of the micro-chaos map (2.19), one can immediately realise the effect of output-quantization: *control effort bands* appear in the state space corresponding to integer F_i values. From this fact, the existence of multiple unstable saddle points also arises.

The switching lines corresponding to the PD-control, separating control effort bands $F_i = m - 1$ and $F_i = m$ are:

$$\mathrm{Int}(\hat{P}\,x + \hat{D}\,x') = m \quad \Rightarrow \quad \mathrm{SW}_m : x' = \frac{m - \hat{P}\,x}{\hat{D}}, \quad m \in \mathbb{Z}\backslash\{0\}. \tag{2.20}$$

For each control effort $F_i = m$, an unstable equilibrium (saddle point) exists:

$$\mathbf{F}_m = \mathbf{U}\,\mathbf{F}_m + \mathbf{b}\,m. \tag{2.21}$$

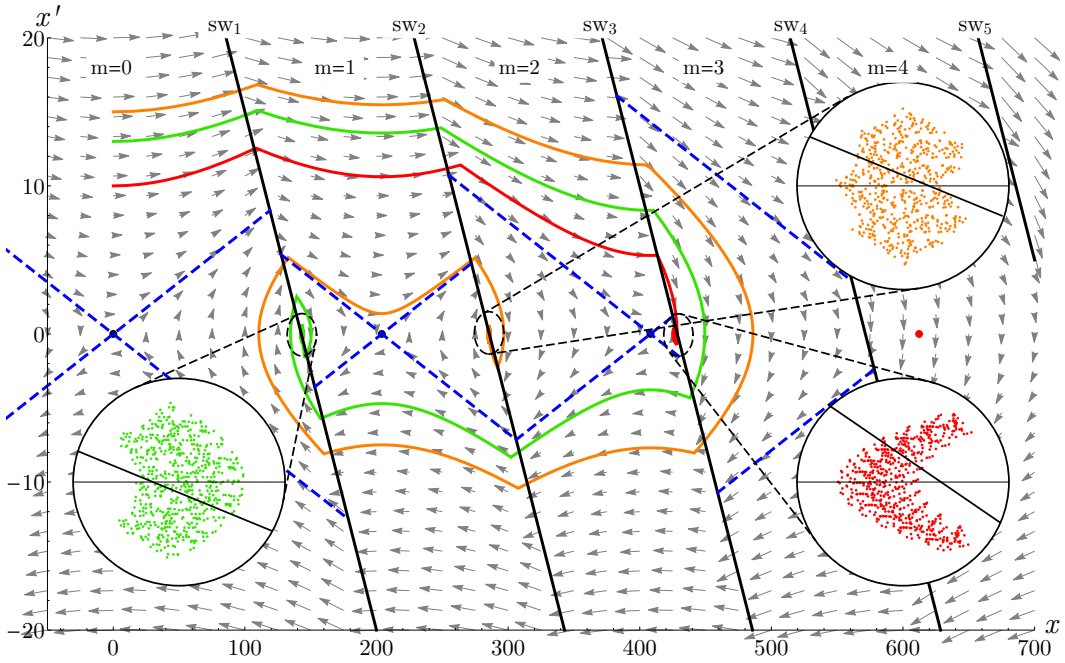

Figure 2.4: The state space of micro-chaos map (2.19). Black lines indicate switching lines, black dots and blue lines are fixed points and their manifolds. Three example trajectories are depicted leading to chaotic attractors, shown in balloons, where states corresponding to sampling instants are shown. The red point in the $m = 4$ band indicates the first virtual fixed point of the map (that is closest to the origin). $\hat{\alpha} = 0.07$, $\delta = 0.03$, $\hat{P} = 0.007$, $\hat{D} = 0.02$.

Fixed points correspond to zero velocity ($\mathbf{F}_m = [x_u^m \quad 0]$), therefore they can be found on the x-axis:

$$\mathrm{Int}(\hat{P}\, x_u^m) = \hat{\alpha}^2\, x_u^m \quad \Rightarrow \quad x_u^m = \frac{m}{\hat{\alpha}^2}, \qquad m \in \mathbb{Z}. \tag{2.22}$$

The corresponding fixed points are denoted by black dots in Figure 2.4. This formula is valid only if x_u^m resides between the m^{th} and $(m+1)^{\text{st}}$ switching lines – since this is required to have a matching control effort value:

$$\frac{|m|}{\hat{P}} \leq \frac{|m|}{\hat{\alpha}^2} < \frac{|m|+1}{\hat{P}}. \tag{2.23}$$

If this condition is not satisfied, the fixed point is said to be *virtual*, see the red dot in Figure 2.4, between the switching lines SW_4 and SW_5.
The stable and unstable manifolds of fixed points are corresponding to the eigenvectors of $\mathbf{U}$:

$$\mathbf{e}_{stable} = \begin{bmatrix} 1 \\ \hat{\alpha}\,(-\Gamma - \delta) \end{bmatrix} \qquad \mathbf{e}_{unstable} = \begin{bmatrix} 1 \\ \hat{\alpha}\,(\Gamma - \delta) \end{bmatrix} \tag{2.24}$$

When varying $\hat{\alpha}$ or $\hat{P}$ parameters, if a fixed point crosses the switching line at $|m|/\hat{\alpha}^2 = (|m|+1)/\hat{P}$, a *border collision* bifurcation occurs and the fixed point becomes virtual. Similarly, if a virtual fixed point crosses the corresponding switching line at $|m|/\hat{P} = |m|/\hat{\alpha}^2$, it turns to a regular fixed point via border collision bifurcation. See Fig. 2.4 and Fig. 2.6.
Iterating the micro-chaos map, these oscillations portray a picture of one or more fractal-like – supposedly chaotic – attractor in the state space, see balloons in Fig. 2.4.
Due to the nature of the dynamics around the unstable saddle points, trajectories are pushed from one control band to the other along the stable and unstable manifolds of the fixed points.

The control effort does not immediately change as a trajectory enters a neighbouring control effort band, it is updated only at the next sampling instant. This allows the trajectories to spend a varying amount of time (until the next sampling occurs) in a neighbouring band with their original dynamics, therefore, irregular oscillation appears between the neighbouring control effort bands, governed by the stable and unstable manifolds of the neighbouring saddle points – if the steps of the map are sufficiently small – see Fig. 2.4.

Therefore, strange sets – chaotic attractors or transient chaotic repellors: conditionally invariant sets corresponding to transient chaos – are expected to be in the neighbourhood of the intersection points of the switching lines and the x axis (see Fig. 2.4):

$$\mathrm{Int}(\hat{P}\, x_{\mathrm{attr}}) = m \quad \Rightarrow \quad x_{\mathrm{attr}} = \frac{m}{\hat{P}}, \qquad m \in \mathbb{Z}\backslash\{0\}. \tag{2.25}$$

Consequently, an alternating pattern of *interesting points* (corresponding to strange sets) and fixed points is present in the state space:

$$\begin{gathered} x_u^0 < x_{\mathrm{attr}}^1 < x_u^1 < x_{\mathrm{attr}}^2 < x_u^2 < \cdots < x_{\mathrm{attr}}^m < x_u^m < \cdots < x_{\mathrm{attr}}^{m_{\max}} \\ 0 < \frac{1}{\hat{P}} < \frac{1}{\hat{\alpha}^2} < \frac{2}{\hat{P}} < \frac{2}{\hat{\alpha}^2} < \cdots < \frac{m}{\hat{P}} < \frac{m}{\hat{\alpha}^2} < \cdots < \frac{m_{\max}}{\hat{P}}. \end{gathered} \tag{2.26}$$

The alternating pattern ends with the first virtual fixed point at $m_{\max}/\hat{\alpha}^2$ that resides in the $(m_{\max}+1)^{\mathrm{st}}$ band.

Restricting the control parameters to the stable domain ($\hat{P} > \hat{\alpha}^2$, see Section 2.1.2), the index $m_{\max}$ of the outermost interesting point can be expressed from Eq. (2.23) :

$$\frac{m}{\hat{\alpha}^2} < \frac{m+1}{\hat{P}} \quad \Rightarrow \quad m\,\frac{\hat{P}-\hat{\alpha}^2}{\hat{P}\,\hat{\alpha}^2} < \frac{1}{\hat{P}} \quad \Rightarrow \quad m < \frac{\hat{\alpha}^2}{\hat{P}-\hat{\alpha}^2}, \tag{2.27}$$

$$m_{\max} = \mathrm{Int}\left(\frac{\hat{\alpha}^2}{\hat{P}-\hat{\alpha}^2}\right). \tag{2.28}$$

Here the function Int – just as in the previous sections – rounds to the next integer towards the zero. In general, the number of fixed points is $\mathrm{N}_{fp} = 2\,m_{\max}+1$, since the origin is also a fixed point, and the number of attractors or repellors is $\mathrm{N}_{\mathrm{attr}} = 2\,m_{\max}$. If $m_{\max} = 0$, the only fixed point is the origin and this pattern does not appear. The condition for this case is:

$$\frac{\hat{\alpha}^2}{\hat{P}-\hat{\alpha}^2} < 1 \quad \Rightarrow \quad 2\,\hat{\alpha}^2 < \hat{P}. \tag{2.29}$$

Based on Condition (2.28), the number of fixed points and interesting points is infinite if $\hat{P} = \hat{\alpha}^2$. Figure 2.6 shows the location of attractors for a case corresponding to realistic system parameters (small $\hat{\alpha}$ and $\hat{P}$ due to relatively small sampling times), where chaotic attractors appear in the neighbourhood of all interesting points. Figure 2.5 illustrates the number of fixed points on the stable domain of control parameters.

In this case, the position of the outermost chaotic attractor can be used to provide a good estimate of the control error. According to Eqs. (2.25) and (2.28), the position of the last interesting point (attractor) can be expressed as:

$$x_{\mathrm{attr,last}} = \frac{m_{\max}}{\hat{P}}, \tag{2.30}$$

which can be considered as an estimation of the maximal control error, since the extent of the chaotic attractors is small.

In order to classify the strange sets at the neighbourhood of *interesting points*, – determine whether they are chaotic attractors or repellors –, the detailed analysis of the vicinity of saddle points is carried out.

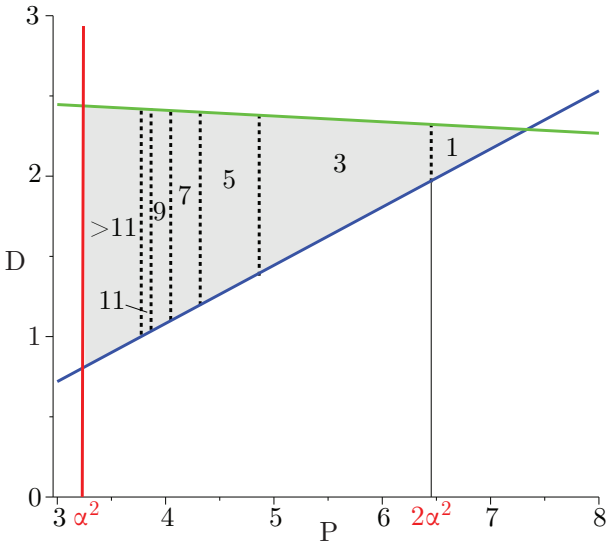

Figure 2.5: The number of fixed points with respect to control parameters, at $\hat{\alpha} = 1.8$ and $\delta = 0.15$. The shaded area is the domain of stability for the sampled system.

2.3.2 Smale horseshoe structures

For the detailed examination of the topology of the phase-space, an attempt is made to find Smale horseshoe structures. As initial domains, parallelograms $Q_r = L \cup R$, defined by the stable and unstable manifolds W_L^S, W_L^U, W_R^S and W_R^U of neighbouring fixed points F_l on the left and F_r on the right are chosen, as depicted in Fig. 2.7. Here $r = l + 1$ denotes the index of the switching line SW_r between the two fixed points. l and r are the integer numbers corresponding to the control effort values in the bands next to the switching line SW_r.
Each parallelogram is divided into two trapezoids (denoted by R on the right and L on the left, see the crosshatched regions in Fig. 2.7) by a switching line. The vertices of the trapezoid L are the fixed point F_l, the intersection point P^{RULS} of the manifolds W_R^U (unstable manifold of the fixed point on the right) and W_L^S (stable manifold of the fixed point on the left), the intersection point P^{RUSW} of W_R^U and the switching line, and the crossing point P^{LUSW} of manifold W_L^U and the switching line, see Fig. 2.7. The vertices of the other trapezoid (R) are the fixed point F_r, and points P^{RUSW}, P^{LUSW} and P^{LURS}, where the notations can be interpreted similarly. The positions of these points can be deteremined by straightforward analytical calculations. The images and pre-images of trapezoids L and R can be calculated by restricting the dynamics to the corresponding band, i.e., to the case $m = l$ or $m = r$. The restricted versions of the micro-chaos map will be denoted by $f_l = f|_{m=l}$ and $f_r = f|_{m=r}$, respectively.
The images of the quadrangles $f_r(R)$ and $f_l(L)$ are stretched along the unstable manifolds, while the pre-images $f_r^{-1}(R)$, $f_l^{-1}(L)$, $f_l^{-1}(R)$ and $f_r^{-1}(L)$ are stretched along the stable manifolds. One must be careful during the determination of pre-images, since e.g. $f_r^{-1}(L) = \tilde{f}_r^{-1}(L) \cap R$, where

$$\tilde{f}_r^{-1}(L) = \left\{ \tilde{\mathbf{y}} \mid \tilde{\mathbf{y}} = \mathbf{U}^{-1}(\mathbf{y} - \mathbf{b}r), \mathbf{y} \in L \right\}. \tag{2.31}$$

Thus, it may happen that some parts of the calculated pre-image set $\tilde{f}_r^{-1}(L)$ are cut away by the switching line SW_r.
It is easy to see in Fig. 2.7 that $f_l(L) \setminus Q_r \neq \emptyset$, i.e., $f_l(L)$ is stretched out from the initial parallelogram at the considered parameter set. Thus, a chaotic repellor with transient chaotic

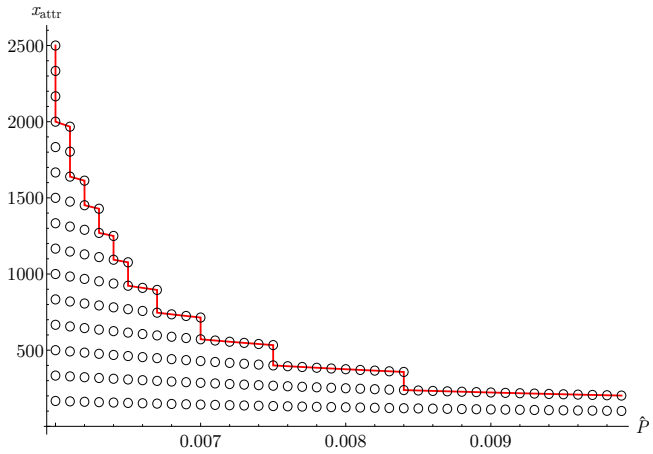

Figure 2.6: Locations of attractors of the micro-chaos map (2.19) with respect of $\hat{P}$, with $\hat{\alpha} = 0.075$, calculated using Eq. (2.25). Increasing $\hat{P}$, the outermost fixed points disappear due to border-collision *which causes the outermost attractors to vanish. (The pattern of attractors and fixed points does not depend on parameters δ and $\hat{D}$.)*

motion exists in this domain.

In general, if there is no trajectory which is able to escape the parallelogram, the horseshoe structure indicates a chaotic attractor. Therefore, the images of corner points of L and R at the switching line SW_r should be analysed, as these states have the highest potential to *jump over* the neighbouring fixed point's manifold.

Figure 2.8 shows four strange sets next to each other. Two of them (at $m = 4$ and $m = 7$) are repellors, while the images of parallelograms do not stretch out from the initial domain at $m = 5, 6$, thus, two separated attractors exist here. In fact, the topology resembles to multiple adjacent baker-maps [7].

The detailed analysis of the images of these points and conditions to classify the strange sets are provided by G. Csernák in [6] and are not covered in this thesis.

It can happen, that two chaotic repellors together form a chaotic attractor in the state space. It is important to note, however, that the horseshoe structures of neighbouring strange sets become entangled in case of extreme jumps passing through multiple control effort bands. The horseshoe structures of neighbouring strange sets become entangled in case of extreme jumps, when trajectories cross multiple control effort bands within a sampling period.

Large $\hat{\alpha}$ corresponds to large sampling period or large amount of inertia and can lead to large jumps away from the origin. Large $\hat{P}$ parameter can be related to excessive control effort and therefore may cause jumps towards the origin – often leading to several control bands into the other half of the phase plane. As a consequence of these jumps, large attractors can be formed in the phase-space, hiding the underlying pattern of saddle points and repellors.

Figure 2.9 shows the transition from separated chaotic attractors to a single chaotic attractor formed by transient chaotic repellors.

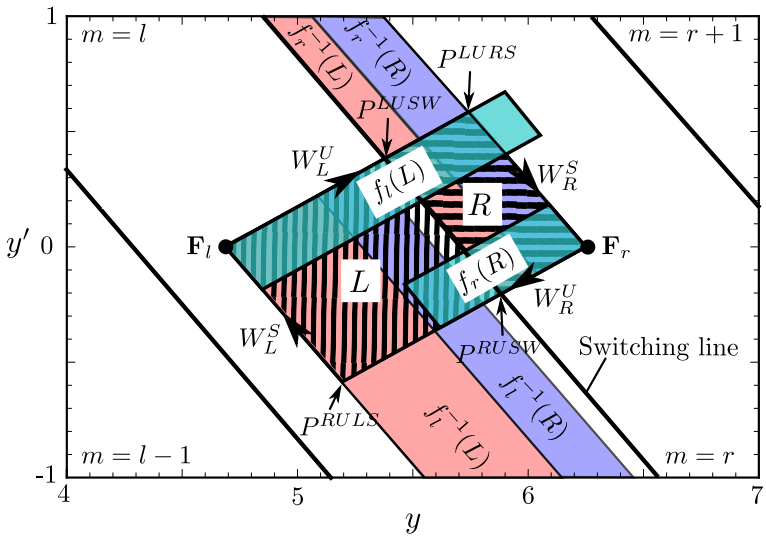

Figure 2.7: The schematic picture of the horseshoe-structure in the parallelogram $Q_r = L \cup R$. Here $r = 4$ and parameter values are $\alpha = 0.8$, $\delta = 0.2$, $P = 0.7$ and $D = 0.6$. Note, that the switching lines and stable manifolds are not necessarily parallel.

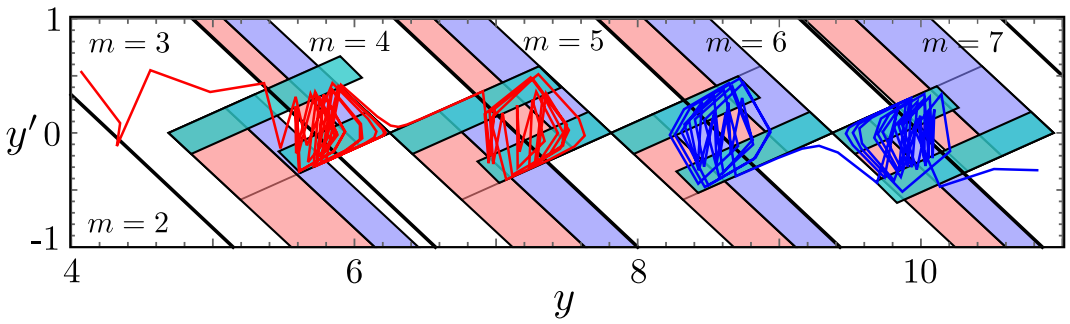

Figure 2.8: The horseshoe structures at the switching lines $m = 4, 5, 6, 7$ at $\alpha = 0.8$, $\delta = 0.2$, $P = 0.7$ and $D = 0.6$. Two trajectories are also shown, leading to disconnected attractors.

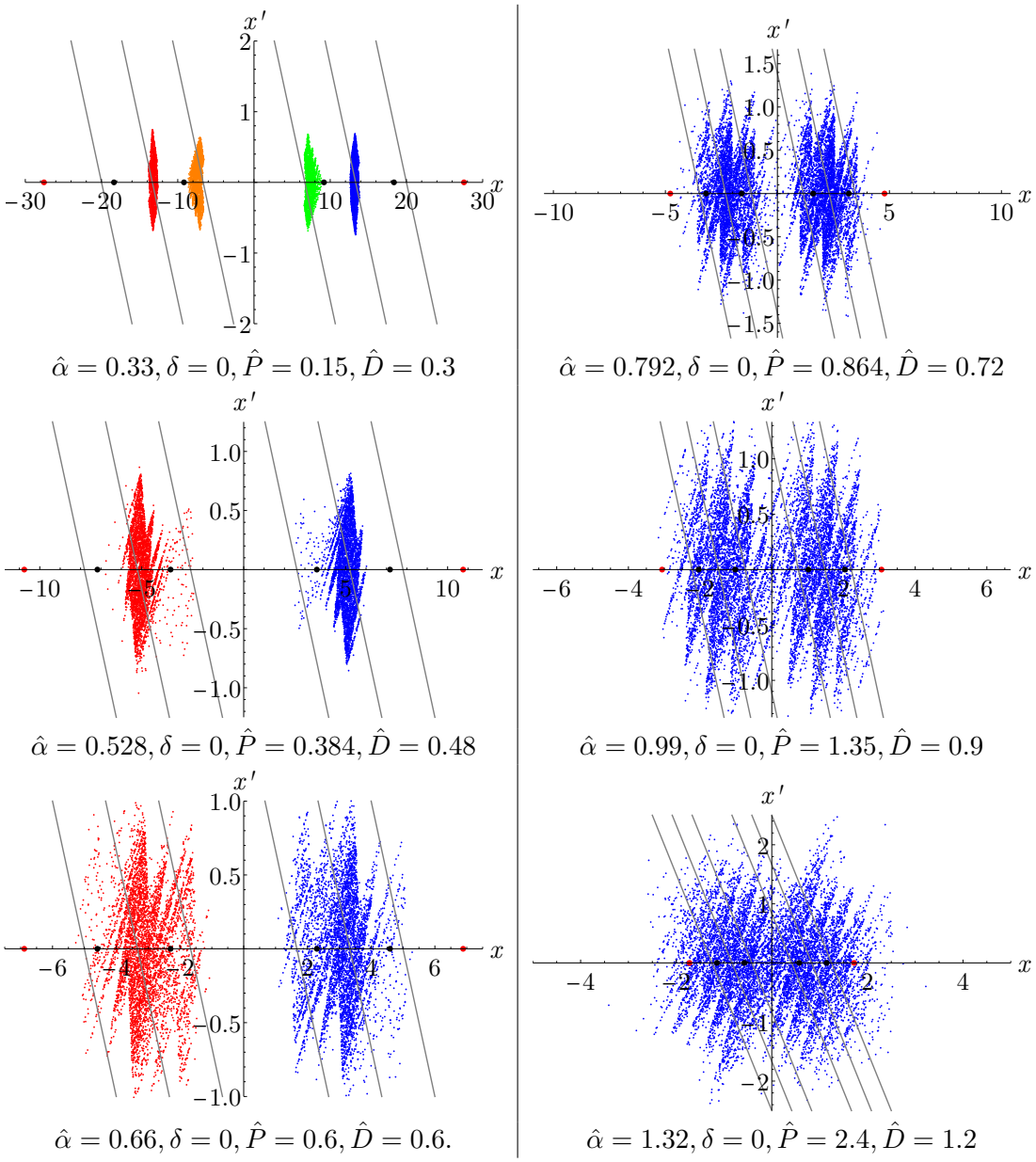

Figure 2.9: The state space of the micro-chaos map when sampling time τ increases.
Left column*: Initially, there are four separated chaotic attractors in the state space. The inner chaotic attractors turn to repellors forming two larger chaotic attractors spanning over multiple control effort bands.*
Right column*: These attractors turn to repellors again forming a single chaotic attractor.*
(Note: only the first 3 switching lines are indicated on either sides, pattern-breaking virtual fixed points are indicated with red dots.)

2.4 Generalisation to multi DoF and control effort quantization

The previous section dealt with the single degree-of-freedom case, introduced a topological pattern of unstable saddle points and *interesting points* – whose neighbourhood contains chaotic attractors or transient chaotic repellors. Smale horseshoe structures were also shown, whose existence solely proves chaos.
For more degrees of freedom and for higher dimensional micro-chaos maps, the overview of state space and finding Smale horseshoe structures is often more difficult. Fortunately, a partial proof of chaos can be done in multi DoF cases by examining the following two properties:

- Sensitive dependence on initial conditions.
- Existence of an absorbing domain.

The above two points correspond to a *mathematically loose, practical* definition of chaos, which lacks the property of topological transitivity.
Additionally, periodic orbits can be provided using a symbolic dynamics approach, independently of the dimension of the micro-chaos map.

2.4.1 Lyapunov exponent

Obtaining the Lyapunov exponents of the micro-chaos map has great importance during the proof of chaos. If the largest Lyapunov exponent (LLE) is larger than 1, the *sensitive dependence on initial conditions* is immediately proven [50, 15].

As it was already mentioned in Section 1.3, the Lyapunov exponents of the micro-chaos map can be directly calculated as the eigenvalues of matrix $\mathbf{U}$.
For example, the Lyapunov exponents in the negative stiffness and output quantization case (Eq. (2.19)) are

$$\lambda^{\mathbf{U}}_{1,2} = \exp(-\delta\,\hat{\alpha} \pm \Gamma\,\hat{\alpha}) = \exp(\hat{\alpha}(-\delta \pm \Gamma)). \tag{2.32}$$

Since $\Gamma = \sqrt{1+\delta^2} > \delta$, one of the eigenvalues is larger than one: $\lambda^{\mathbf{U}}_1 > 1 > \lambda^{\mathbf{U}}_2$. Thus, the micro-chaos map is sensitive to the initial conditions. This result corresponds to the fact that all equilibria are locally unstable saddle points.

2.4.2 Absorbing domain; absorbing cuboid

An *absorbing domain* $\mathcal{A}$ in the state space of the micro-chaos map f can be defined with

- $f(\mathcal{A}) \subset \mathcal{A}$, and
- there is $n > 0$ for every $\mathbf{y}_0$, such that $f^n(\mathbf{y}_0) \in \mathcal{A}$.

That is, the image of the absorbing domain is within itself, and eventually, the map leads to the absorbing domain from all initial conditions. This subsection provides an estimate for the size of the smallest possible absorbing domain of the micro-chaos map.

The micro-chaos map (2.19) expresses an unstable, uncontrolled system, which is stabilized with a quantized control effort:

$$\mathbf{y}_{i+1} = \mathbf{U}\,\mathbf{y}_i + \mathbf{b}\,F_i, \qquad F_i \in \mathbb{Z}. \tag{2.33}$$

As it was already mentioned in Section 1.3, the micro-chaos map can be rewritten as a stabilized system without quantization, from which correction terms corresponding to the neglected fractional parts (χ_i) are subtracted [9].

$$\mathbf{y}_{i+1} = \mathbf{S}\,\mathbf{y}_i - \mathbf{b}\,\chi_i, \qquad \chi_i \in \mathbb{R}. \tag{2.34}$$

Eqs. (2.33) and (2.34) are valid for higher-dimensional micro-chaos maps, too, in the case of output quantization. For the inverted pendulum (2.19),

$$\mathbf{S} = \mathbf{U} + \mathbf{b} \otimes \mathbf{k}, \qquad \mathbf{k} = \begin{bmatrix} P \\ D \end{bmatrix}. \tag{2.35}$$

This formalism allows one to express an estimate for the maximum control error introduced by the digital effects. Applying the micro-chaos map repeatedly, the following expression can be written:

$$\mathbf{y}_{j+1} = \mathbf{S}^j \, \mathbf{y}_0 - \sum_{k=0}^{j-1} \mathbf{S}^k \, \mathbf{b} \, \chi_k. \tag{2.36}$$

If the control parameters are chosen from the stable parameter domain (Sec. 2.1.2), the eigenvalues of $\mathbf{S}$ are inside the unit circle on the complex plane [9], therefore:

$$\lim_{j \to \infty} \|\mathbf{S}^j\| = 0, \tag{2.37}$$

with any kind of norm, meaning that the information originating from the initial state will eventually vanish and solutions will tend towards an absorbing domain in the state space.

It is possible to define a sequence of fractional parts $\chi = \{\chi_1, \chi_2, \dots \chi_k\}$, such that the following series is convergent and tends to the farthest point of the invariant set of the micro-chaos map, or in other words $\mathbf{y}_\infty$ denotes the limit of all possible solutions (after transient behaviour disappears):

$$\|\mathbf{y}_\infty\| = \max_{\chi} \left\| \lim_{j \to \infty} \sum_{k=0}^{j} \mathbf{S}^k \, \mathbf{b} \, \chi_k \right\|, \tag{2.38}$$

where the limit is maximized with respect to the sequence of fractional parts χ. Introducing $\mathbf{D}$ as the diagonal matrix of eigenvalues (λ_i) and $\mathbf{T}$, the matrix formed by the columns of right eigenvectors of $\mathbf{S}$, one can write:

$$\mathbf{y}_\infty = -\mathbf{T} \sum_{k=0}^{\infty} \mathbf{D}^k \, \mathbf{T}^{-1} \, \mathbf{b} \, \chi_k. \tag{2.39}$$

If the diagonalization of $\mathbf{S}$ exists, then (2.39) will converge, since the eigenvalues of $\mathbf{S}$ are within the unit circle on the complex plane by definition [6]. The case, when the diagonalization of $\mathbf{S}$ does not exist is not covered in this thesis, but for reasonable system parameters this does not occur. Let ϕ_i and ρ_i denote the modulus and argument of the i^{th} eigenvalue λ_i, and $\tilde{\mathbf{b}} = \mathbf{T}^{-1} \, \mathbf{b}$. With this notation, Eq. (2.39) can be written as:

$$\mathbf{y}_\infty = -\mathbf{T} \begin{bmatrix} \sum_{k=0}^{\infty} \lambda_1^k \, \chi_k \, \tilde{b}_1 \\ \sum_{k=0}^{\infty} \lambda_2^k \, \chi_k \, \tilde{b}_2 \\ \vdots \\ \sum_{k=0}^{\infty} \lambda_n^k \, \chi_k \, \tilde{b}_n \end{bmatrix} = - \begin{bmatrix} \sum_{k=0}^{\infty} \sum_{j=1}^{n} T_{1,j} \lambda_j^k \, \chi_k \, \tilde{b}_j \\ \sum_{k=0}^{\infty} \sum_{j=1}^{n} T_{2,j} \lambda_j^k \, \chi_k \, \tilde{b}_j \\ \vdots \\ \sum_{k=0}^{\infty} \sum_{j=1}^{n} T_{n,j} \lambda_j^k \, \chi_k \, \tilde{b}_j \end{bmatrix} =$$

$$- \begin{bmatrix} \sum_{k=0}^{\infty} \sum_{j=1}^{n} T_{1,j} \, \rho_j^k \left(\cos(k \, \phi_j) + i \, \sin(k \, \phi_j)\right) \chi_k \, \tilde{b}_j \\ \sum_{k=0}^{\infty} \sum_{j=1}^{n} T_{2,j} \, \rho_j^k \left(\cos(k \, \phi_j) + i \, \sin(k \, \phi_j)\right) \chi_k \, \tilde{b}_j \\ \vdots \\ \sum_{k=0}^{\infty} \sum_{j=1}^{n} T_{n,j} \, \rho_j^k \left(\cos(k \, \phi_j) + i \, \sin(k \, \phi_j)\right) \chi_k \, \tilde{b}_j \end{bmatrix} := \begin{bmatrix} \sum_{k=0}^{\infty} \sigma_{1,k} \, \chi_k \\ \sum_{k=0}^{\infty} \sigma_{2,k} \, \chi_k \\ \vdots \\ \sum_{k=0}^{\infty} \sigma_{n,k} \, \chi_k \end{bmatrix}. \tag{2.40}$$

Note, that in each component of $\mathbf{y}_\infty$, the same χ_k fractional part appears.
To maximize the i^{th} component of $\mathbf{y}_\infty$, the following choice of the k^{th} fractional part should be made:

$$\chi^i = \{\chi_k\} = \{\text{sign}(\sigma_{i,k})\}, \qquad k = 0, 1, 2, \dots \tag{2.41}$$

Eq. (2.41) yields a good upper estimation when compared to simulated results.

A global *absorbing cuboid* can be defined by taking components of $\mathbf{y}_\infty$ with the substitution of the corresponding set of fractional parts χ^i which maximize that component:

$$\mathbf{y}_{\text{abs}} = \begin{bmatrix} y_{\infty,1}\,|_{\chi=\chi^1} \\ y_{\infty,2}\,|_{\chi=\chi^2} \\ \vdots \\ y_{\infty,n}\,|_{\chi=\chi^n} \end{bmatrix}. \tag{2.42}$$

This absorbing cuboid can provide a basis for the error estimation and can be used during the proof of chaos, as well.

Providing a set of neglected fractional parts which maximize a certain norm can be rather challenging, see Section 2.5, [25].

2.4.3 Periodic orbits and symbolic dynamics

Periodic orbits can be used to verify the previously introduced error estimation. If periodic orbits up to a relatively long period are obtained, they are expected to cover the invariant set – chaotic attractor – of the micro-chaos map quite well.

Starting with the estimation provided by Eq. (2.42) or Eq. (2.30), it is possible to select a corresponding symbolic dynamics, where symbols correspond to control effort values:

$$\mathfrak{m} = \{-m_{\max}, -m_{\max}+1, \ldots, 0, 1, 2, \ldots, m_{\max}\}. \tag{2.43}$$

It can be seen, that a p-periodic orbit starting from $\mathbf{y}_0$ can be expressed as:

$$\mathbf{y}_p \equiv \mathbf{y}_0 = (\mathbf{I} - \mathbf{U}^p)^{-1} \left(m_0 \mathbf{U}^{p-1} + m_1 \mathbf{U}^{p-2} + \cdots + m_{p-1}\mathbf{U}^0 \right) \mathbf{b}. \tag{2.44}$$

Here $\{m_0, m_1, \ldots, m_{p-1}\}$ is a combination of symbols selected from $\mathfrak{m}$. In order to enumerate all p-periodic orbits using Eq. (2.44), the prime cycles [15] – circular permutations with repetition – of symbol set $\mathfrak{m}$ of length p are calculated and substituted, see Table 2.2.
Then all possible periodic orbit is tested by repeatedly applying the micro-chaos map and verifying the actual control effort value m_i. Obviously, a periodic orbit is only valid if:

$$F(\mathbf{y}_i) = m_i \quad \text{for} \quad i = 0, 1, \ldots, p. \tag{2.45}$$

p	Prime cycles (circular permutations with repetitions)
1	$\{0\}, \{1\}, \{2\}$
2	$\{01\}, \{02\}, \{12\}$
3	$\{001\}, \{002\}, \{011\},$ $\{012\}, \{021\}, \{022\},$ $\{112\}, \{122\}$
4	$\{0001\}, \{0002\}, \{0011\}, \{0012\}, \{0021\}, \{0022\},$ $\{0102\}, \{0111\}, \{0112\}, \{0121\}, \{0122\}, \{0211\},$ $\{0212\}, \{0221\}, \{0222\}, \{1112\}, \{1122\}, \{1222\}$

Table 2.2: Prime cycles of $\mathfrak{m} = \{0, 1, 2\}$, up to length $p = 4$.

Applying the method and generating the periodic orbits up to $p = 22$ in case of the micro chaos map with a symbol alphabet length of 11 ($m = -5, \ldots, +5$), and plotting the periodic

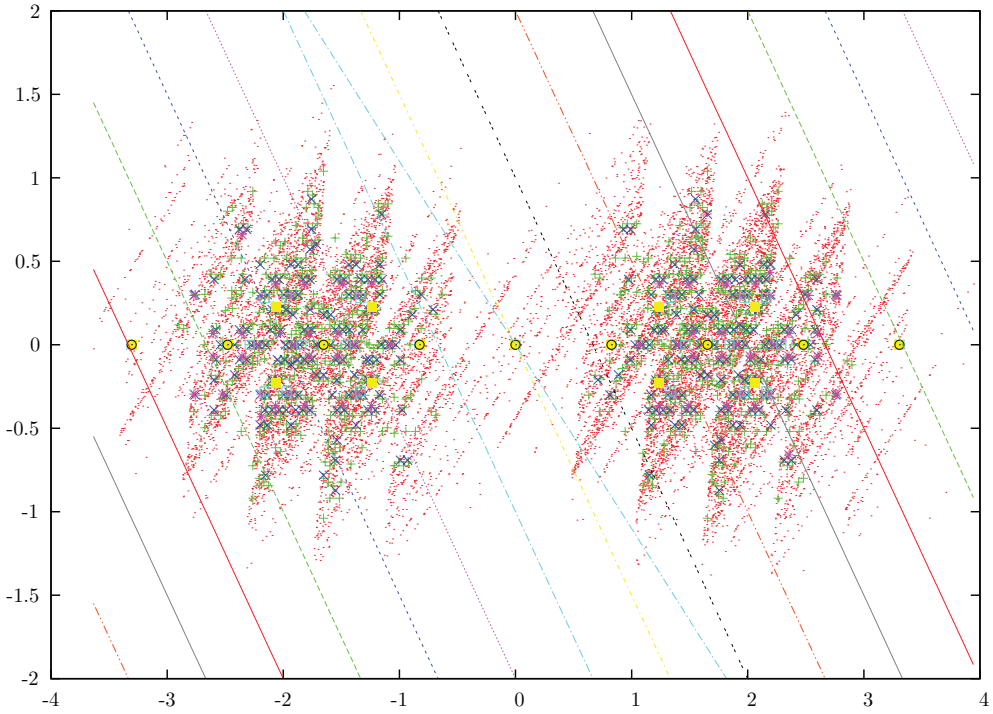

Figure 2.10: Unstable periodic orbits (indicated with coloured crosses) from length 3 to length 22 covering a chaotic attractor (red points), at $\hat{\alpha} = 1, \delta = 0, \hat{P} = 1.25, \hat{D} = 0.8$. *Yellow circles indicate saddle points, coloured lines indicate switching lines.*

orbits give a good picture of the chaotic attractor which spans over multiple control effort bands, see Figure 2.10. These periodic orbits are unstable and therefore difficult to find with numerical simulation. One can imagine, that the actual chaotic behaviour is formed by these unstable periodic orbits.

2.5 Application: Multi-PD controlled double inverted pendulum

Consider a double inverted pendulum with a control torque at the lower joint (Fig. 2.11, left). Given a multi PD-control – e.g., separate proportional and derivative control terms for every part – with zero order hold, τ sampling period, and rounding of the control signal, the torque between the i^{th} and $(i+1)^{\text{st}}$ sampling instances can be written as:

$$M = \rho_{\text{M}}\,\text{Int}\left(\frac{1}{\rho_{\text{M}}}\underbrace{\left(p_1\,\varphi_1(t_i) + d_1\,\dot{\varphi}_1(t_i) + p_2\,\varphi_2(t_i) + d_2\,\dot{\varphi}_2(t_i)\right)}_{:=m(t_i)}\right), \quad t_i = t_0 + i\,\tau. \tag{2.46}$$

Here p_1, p_2, d_1, d_2 are control gains, and ρ_{M} is the resolution of the control torque. After linearization, the equation of motion can be solved between successive sampling instants. Introducing dimensionless time $T = t/\tau$ and rearranging the solution of the equation of motion, one obtains the following *micro-chaos* map, that describes the state of the pendulum at successive sampling instants:

$$\mathbf{y}_{i+1} = \mathbf{U}\,\mathbf{y}_i + \mathbf{b}\,M, \tag{2.47}$$

where: $\mathbf{y}_i^{\text{T}} = \left(\begin{array}{cccc}\dot{\varphi}_1(t_i) & \dot{\varphi}_2(t_i) & \varphi_1(t_i) & \varphi_2(t_i)\end{array}\right)$. $\mathbf{U}$ and $\mathbf{b}$ are composed from the solution:

$$\mathbf{U} = \begin{bmatrix} \frac{A_{12}c_2 - A_{22}c_1}{A_{12}-A_{22}} & \frac{c_1-c_2}{A_{12}-A_{22}} & \frac{A_{22}\alpha_1 s_1 - A_{12}\alpha_2 s_2}{A_{12}-A_{22}} & \frac{\alpha_2 s_2 - \alpha_1 s_1}{A_{12}-A_{22}} \\ \frac{A_{12}A_{22}(c_2-c_1)}{A_{12}-A_{22}} & \frac{A_{12}c_1 - A_{22}c_2}{A_{12}-A_{22}} & \frac{A_{12}A_{22}(\alpha_1 s_1 - \alpha_2 s_2)}{A_{12}-A_{22}} & \frac{A_{22}\alpha_2 s_2 - A_{12}\alpha_1 s_1}{A_{12}-A_{22}} \\ \frac{A_{12}\alpha_1 s_2 - A_{22}\alpha_2 s_1}{A_{12}\alpha_1\alpha_2 - A_{22}\alpha_1\alpha_2} & \frac{\alpha_2 s_1 - \alpha_1 s_2}{A_{12}\alpha_1\alpha_2 - A_{22}\alpha_1\alpha_2} & \frac{A_{12}c_2 - A_{22}c_1}{A_{12}-A_{22}} & \frac{c_1-c_2}{A_{12}-A_{22}} \\ \frac{A_{12}A_{22}\alpha_1 s_2 - A_{12}A_{22}\alpha_2 s_1}{A_{12}\alpha_1\alpha_2 - A_{22}\alpha_1\alpha_2} & \frac{A_{12}\alpha_2 s_1 - A_{22}\alpha_1 s_2}{A_{12}\alpha_1\alpha_2 - A_{22}\alpha_1\alpha_2} & \frac{A_{12}A_{22}(c_2-c_1)}{A_{12}-A_{22}} & \frac{A_{12}c_1 - A_{22}c_2}{A_{12}-A_{22}} \end{bmatrix},$$

$$\mathbf{b}^{\text{T}} = \begin{bmatrix} \frac{A_{22}\,s_1}{\alpha_1(A_{12}-A_{22})} & \frac{A_{12}\,s_2}{\alpha_2(A_{22}-A_{12})} & \frac{A_{22}\,c_1 i}{\alpha_1(A_{12}-A_{22})} & \frac{A_{12}\,c_2 i}{\alpha_2(A_{22}-A_{12})} \end{bmatrix}.$$

Here, the eigenvalues of $\mathbf{U}$ are $\lambda_{1,2} = 0 \pm \alpha_1^2$ and $\lambda_{3,4} = 0 \pm \alpha_2^2$, where α_1, α_2 are characteristic time constants, c_i and s_i are $\cosh(\alpha_i)$ and $\sinh(\alpha_i)$ respectively, and A_{12} and A_{22} are the 2^{nd} components of the mode shape vectors (with the first component taken as $A_{i,1} = 1$).

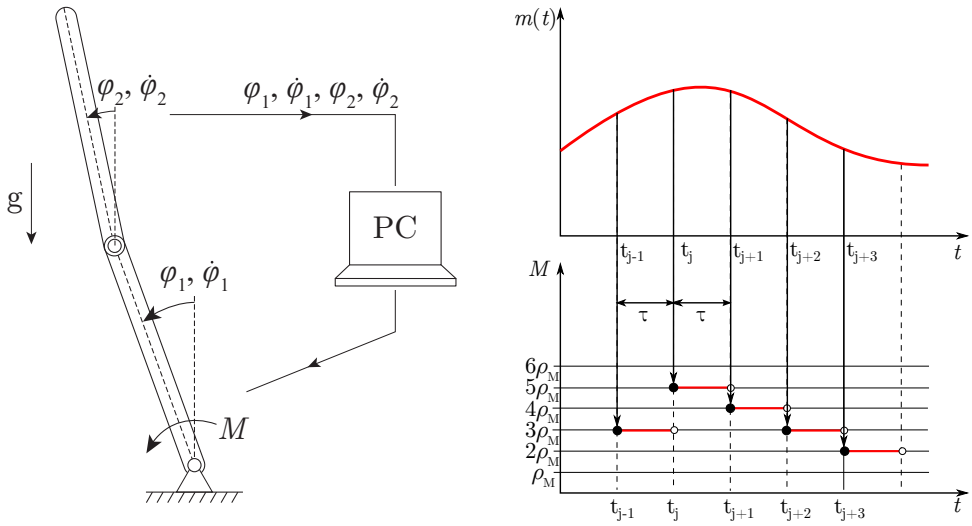

Figure 2.11: Double inverted pendulum with control torque and zero order hold multi-PD control. The calculated control effort $m(t)$ is rounded due to the quantization of the control torque. See Eq. (2.46).

2.5.1 Stable parameter region of multi-PD control

Considering the stability of the multi-PD control, one can calculate the 4D parameter region (see Fig. 2.12) corresponding to stable equilibrium solution for the sampled, but not rounded case at $\varphi_1 = 0$, $\varphi_2 = 0$, using the Jury's stability criterion. If the rounding is taken into account, the stabilized equilibrium becomes unstable, as the control turns off in the band corresponding to $M = 0$, although the equilibrium remains practically stable [43] outside the $M = 0$ band. Therefore, the goal is the determination of the practical stability of the micro-chaos map and the maximum distance of trajectories from the origin is examined.
It is important to note, that a stabilizing control can be achieved with p_1 turned off. This enables one to examine the projection of solutions and switching planes defined by Eq. (2.46) in a 3D subspace of the state-space, as switching planes does not depend on φ_1 (See Fig. 2.13.)

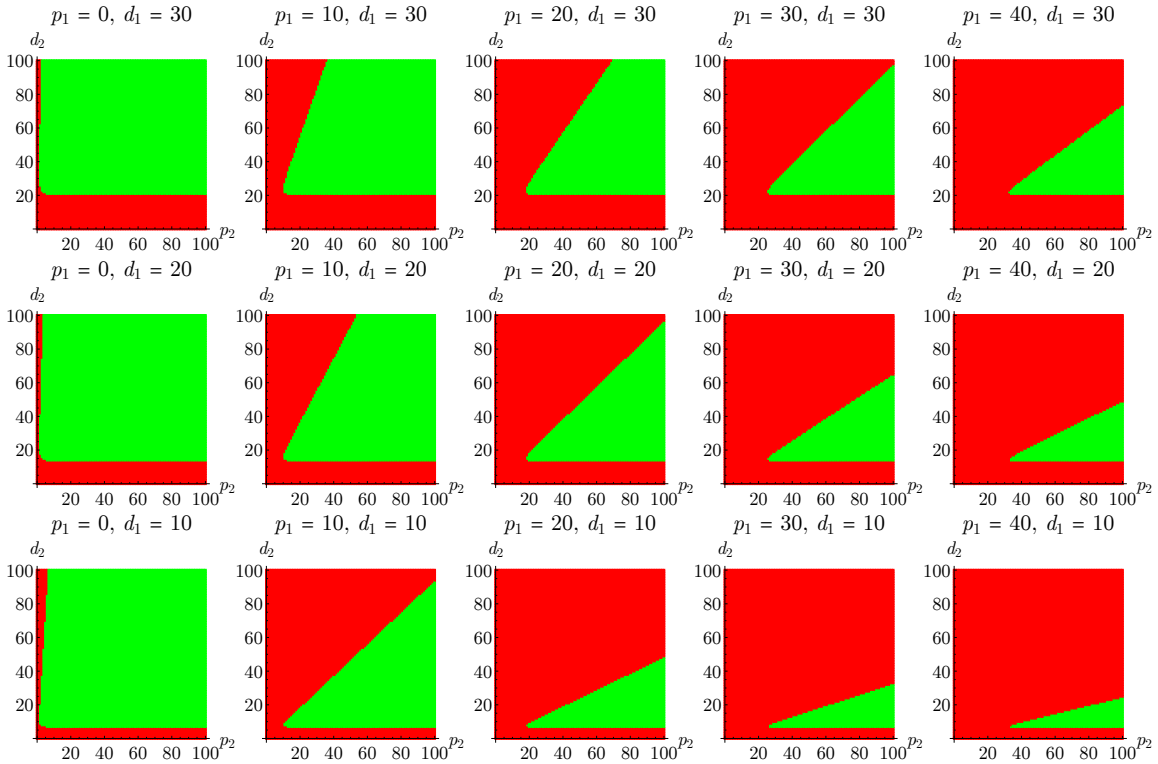

Figure 2.12: Stable parameter domain of the multi-PD control. Green ■ indicates stable, red ■ indicates unstable parameter regions.

2.5.2 Micro-chaotic behaviour

The rounding in the micro-chaos map defines switching surfaces, which separate bands with the same integer result of the rounding function (see Eq. (2.46)). For a given torque-resolution, increasing the sampling time τ allows the system to venture into a neighbouring band to some extent, before the next sampling occurs and the control torque is updated.
As explained before, this results in chaotic behaviour, as the time instant and the position of entries and exits vary during the motion between adjacent bands. An example attractor, where the solution visits the $M = -\rho_{\mathrm{M}}$, $M = 0$ and $M = \rho_{\mathrm{M}}$ bands can be seen in Fig. 2.13.
If the system parameters correspond to larger sampling times or smaller torque-resolution, the system can cross multiple control bands before the next sampling occurs (i.e., before the

value of M gets updated).

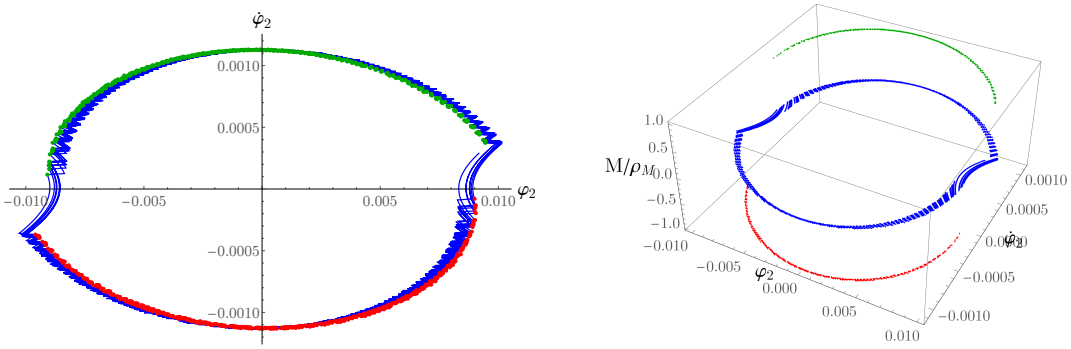

Figure 2.13: Example attractor of the micro-chaos map (2.47). Colours indicate different M values. Red ■, blue ■ and green ■ colours indicate $\mathrm{M}/\rho_{\mathrm{M}} = -1,\ 0,\ +1$ values. On the left image, the points of the attractor are joined with blue lines.

2.5.3 Estimation of error in the micro-chaos map

Rewriting the micro-chaos map into the form mentioned in Section 2.4.2, one obtains

$$\mathbf{y}_{i+1} = \mathbf{S}\,\mathbf{y}_i - \mathbf{b}\,\chi_i \tag{2.48}$$

where $\mathbf{S} = \mathbf{U} + \mathbf{b} \otimes [d_1\, d_2\, p_1\, p_2]$ is the map corresponding to the stabilized system and χ_i denotes the fractional part removed during the i^{th} rounding.

In order to estimate the maximal error of the controller, Eq. (2.38) is applied. Every component of $\mathbf{y}_\infty$ is maximized with a separate choice of the k^{th} fractional part $\chi_k = \operatorname{sign}(\sigma_{i,k})$, yielding a good upper estimation when compared to simulated results, see Fig. 2.14.

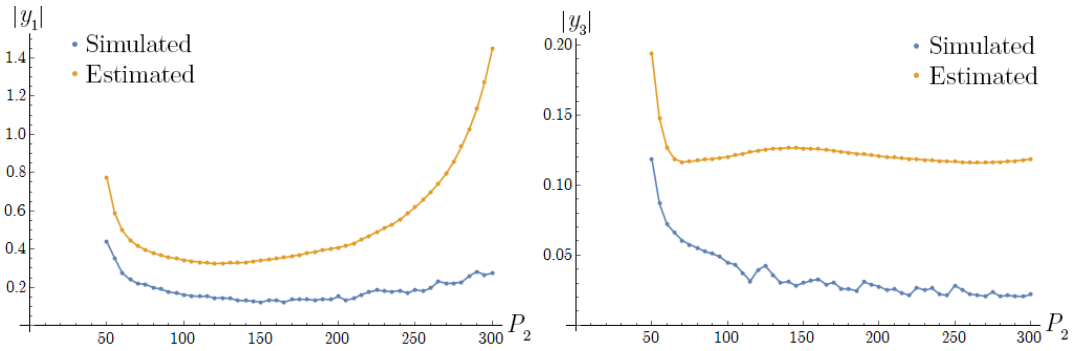

Figure 2.14: Comparison of simulated and estimated maxima for $y_1 = \dot{\varphi}_1$ and $y_3 = \varphi_1$.

As it was mentioned in Section 2.4.2, it is not trivial to select a set of fractional parts to maximize a certain norm. One can construct a suboptimal choice of χ_k to estimate the maximum $\mathfrak{L}_1$ norm. Rewrite Eq. (2.40) in the following form:

$$\mathbf{y}_\infty = \begin{bmatrix} \sum_{k=0}^{\infty} \sigma_{1,k} \\ \sum_{k=0}^{\infty} \sigma_{2,k} \\ \vdots \\ \sum_{k=0}^{\infty} \sigma_{n,k} \end{bmatrix} = \begin{bmatrix} \sum_{k=0}^{\infty} e_{1,k}\,\chi_k \\ \sum_{k=0}^{\infty} e_{2,k}\,\chi_k \\ \vdots \\ \sum_{k=0}^{\infty} e_{n,k}\,\chi_k \end{bmatrix} = \begin{bmatrix} s_{1,m} + \sum_{k=m+1}^{\infty} e_{1,k}\,\chi_k \\ s_{2,m} + \sum_{k=m+1}^{\infty} e_{2,k}\,\chi_k \\ \vdots \\ s_{n,m} + \sum_{k=m+1}^{\infty} e_{n,k}\,\chi_k \end{bmatrix}, \tag{2.49}$$

where $s_{j,m}$ denotes $\sum_{k=0}^{m} e_{j,k}\,\chi_k$. To maximize the $\mathfrak{L}_1$ norm of $\mathbf{y}_\infty$, the following strategy was followed: the k^{th} fractional part χ_k is chosen such that the new terms maximize the increase of the $\mathfrak{L}_1$ norm in the k^{th} step, taking into account the sign of the already accumulated part of the series. According to this rule, one can write:

$$\chi_k = \text{sign}(\text{sign}(s_{1,k-1})\,e_{1,k} + \text{sign}(s_{2,k-1})\,e_{2,k} + \cdots + \text{sign}(s_{n,k-1})\,e_{n,k}) = \text{sign}(\text{sign}(\mathbf{s}_k)^{\mathrm{T}}\,\mathbf{e}_k). \tag{2.50}$$

Although the rule for the choice of χ_k described by Eq. (2.50) does not yield the optimal choice to maximize the $\mathfrak{L}_1$ norm of $\mathbf{y}_\infty$, it provides a good estimation. The optimal χ_k series (yielding the maximum $\mathfrak{L}_1$ norm) for $k \in \{0 \dots 100\}$ had been generated and was compared to the rule based estimation (See Fig. 2.15.). It was found that the rule based estimation yields close results to the optimal one. It is important to note, that generating the optimal χ_k series involves exponential time complexity, as the number of combinations is 2^l for a given series length l.

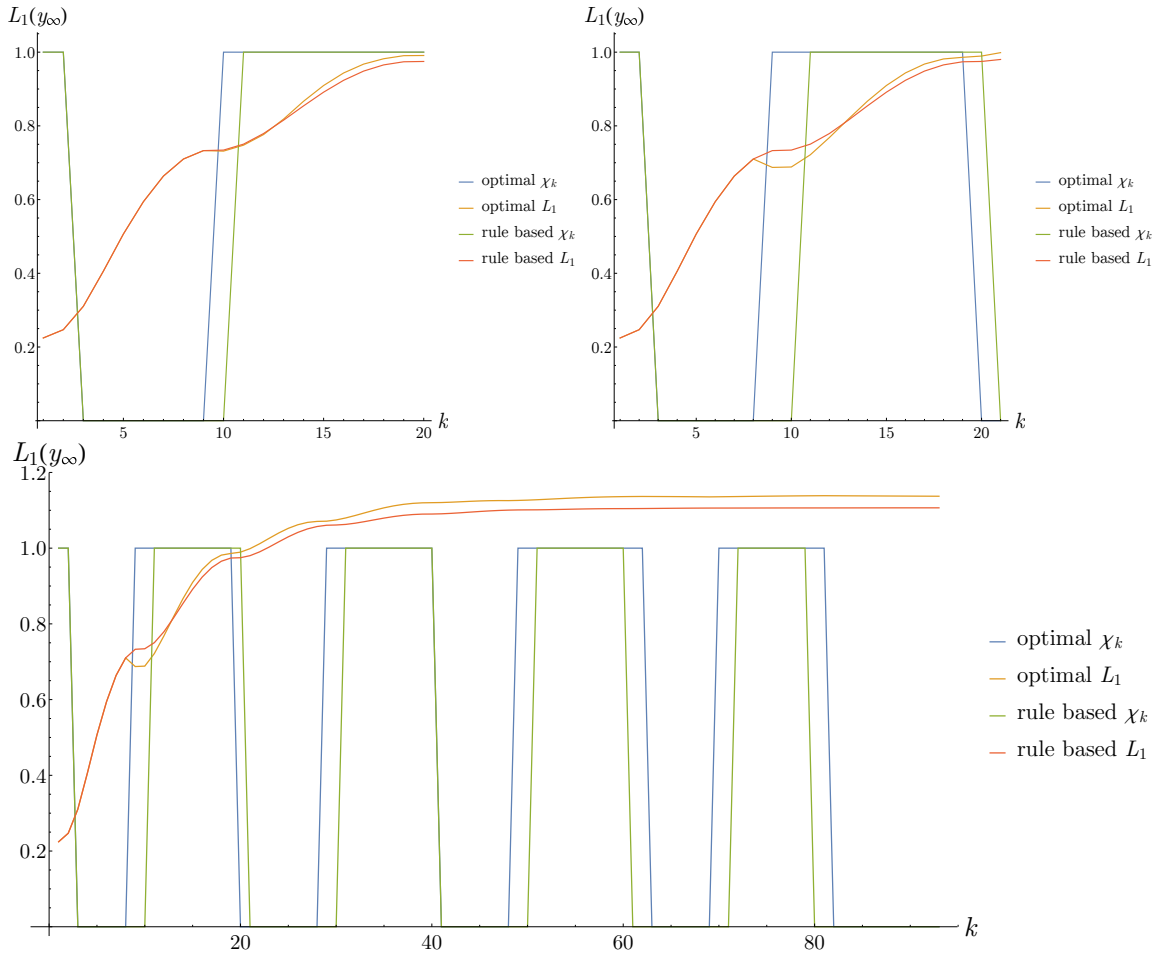

Figure 2.15: Analysis of rule-based $\mathfrak{L}_1$ norm estimation with: $\alpha_1 = 4.23763$, $\alpha_2 = 11.3663$, $A_{12} = 1.4305$, $A_{22} = -2.09717$. One can see, that the optimal χ_k combination incorporates a choice of χ_9 which decreases the $\mathfrak{L}_1$ norm locally, but increases its value overall. Top left: *series length $k = 20$*, right: $k = 21$, bottom: $k = 93$.

2.5.4 Application of Simple Cell Mapping

The estimated control errors can be used to choose the initial state space region for the Simple Cell Mapping method [35], which is used for further analysis of the micro-chaos map. Consequently, the estimation of various norms can be used effectively, even if they are determined with minor inaccuracies (due to the truncating of the infinite series, or using the rule based estimation of $\mathfrak{L}_1$ norm, for example.) An example of application to the micro-chaos map (2.47) is shown in Fig. 2.16, which illustrates the result of SCM using a low resolution cell state space.

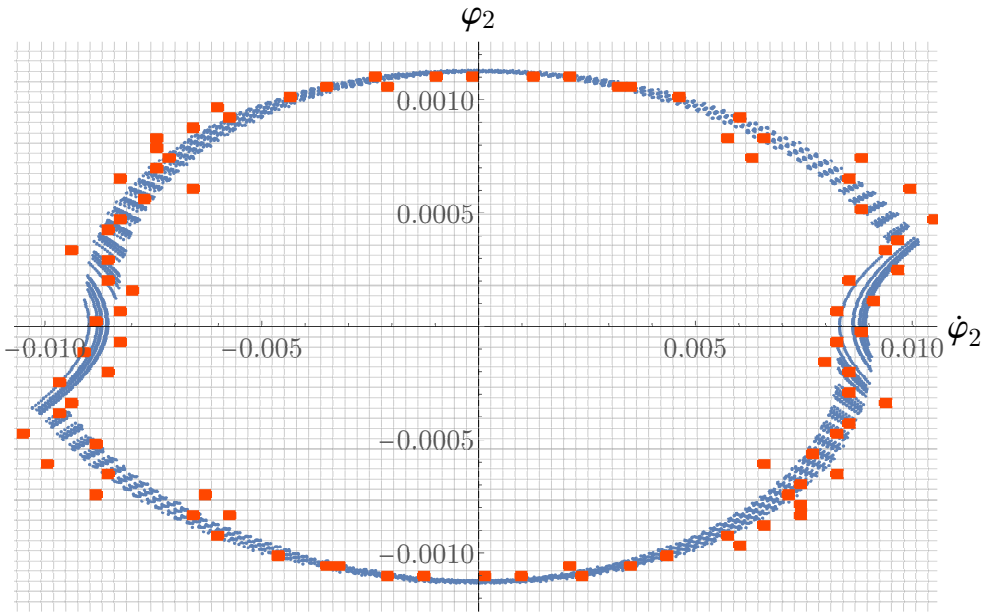

Figure 2.16: SCM results with a cell state space of $40 \times 100 \times 40 \times 60$ *cells (total of* 9.6 *million cells). Orange* ■ *tiles indicate a periodic group of 92 cells situated on the attractor, blue* ■ *dots show the attractor obtained with numerical simulation.*

2.6 Outlook towards input quantization

The previous sections of this chapter dealt with the case of output-quantization, when the calculated control effort is quantized. This section provides a brief overview about the case of input-quantization, when the input of the controller, i.e., the measured state is subjected to rounding.

Most of the previously mentioned methods and approaches can be applied or generalised to this case, as well [14, 30, 25, 7]. However, as it will be shown in this section, the complexity of input-quantization is higher due to the separated quantization of every component of the state variable.

2.6.1 Micro-chaos map of an inverted pendulum with input-quantization

Consider an inverted pendulum with sampling, zero-order hold and quantization at the measured angle – the input of the controller – with resolution r_I and sampling period τ. Assuming that the angular velocity is calculated from the sampled angle values, its resolution is r_I/τ. Consequently, the linearized equation of motion can be written as:

$$\ddot{\varphi}(t) + 2\delta\alpha\dot{\varphi}(t) - \alpha^2\varphi(t) = -P\, r_\mathrm{I}\,\mathrm{Int}\left(\frac{\varphi(t_i)}{r_\mathrm{I}}\right) - D\,\frac{r_\mathrm{I}}{\tau}\,\mathrm{Int}\left(\frac{\dot{\varphi}(t_i)\,\tau}{r_\mathrm{I}}\right), \qquad i = 1, 2, \ldots, \tag{2.51}$$

where α is the inverse of the characteristic time constant that describes the uncontrolled inverted pendulum, δ is the relative damping, P and D are control parameters. Function Int() denotes rounding towards the origin, according to Fig. 1.4.
Introducing the dimensionless time $T = t/\tau$, system parameters $\hat{\alpha} = \alpha\,\tau$, $\hat{P} = P\,\tau^2$, $\hat{D} = D\,\tau$ and the re-scaled space coordinate $x = \varphi/r_\mathrm{I}$, the resolution parameter can be eliminated. Note, that this choice of dimensionless displacement and time results in the same quantization resolutions of the displacement and velocity.
According to the solution of the linearized, dimensionless equation of motion (2.4), the following micro-chaos map can be written describing the evolution of the system between the states at subsequent sampling instants:

$$\begin{aligned} \mathbf{y}_{i+1} &= \mathbf{U}\,\mathbf{y}_i + \mathbf{b}\,F_i, \\ F_i &= \hat{P}\ \mathrm{Int}(x_i) + \hat{D}\ \mathrm{Int}(x'_i), \end{aligned} \tag{2.52}$$

where $\mathbf{y} = [x_i \quad x'_i]^T$, and $\mathbf{U} \equiv \mathbf{U}(1)$, $\mathbf{b} \equiv \mathbf{b}(1)$ from Eq. (2.7).
Equation (2.52) is the micro-chaos map corresponding to the negative stiffness and input quantization case (case B in Table 2.1).

2.6.2 Switching lines and control effort tiles

The most notable difference compared to the case of output quantization is that input-quantization yields a separate rounding for every state variable. In the case of the 2D micro-chaos map (2.52), the control effort contains the quantized position m_i and the quantized velocity n_i:

$$F_i = \hat{P}\underbrace{\mathrm{Int}(x_i)}_{:=m_i} + \hat{D}\underbrace{\mathrm{Int}(x'_i)}_{:=n_i}. \tag{2.53}$$

Therefore, horizontal and vertical switching lines are present in the state space forming a rectangular grid, see Figure 2.17. The equations of switching lines are:

$$\begin{aligned} \mathrm{SW}_m: &\quad x = m\,r_\mathrm{I}, \quad m \in \mathbb{Z}\backslash\{0\}, \\ \mathrm{SW}_n: &\quad x' = n\,r_\mathrm{I}, \quad n \in \mathbb{Z}\backslash\{0\}. \end{aligned} \tag{2.54}$$

Control effort tile $T_{m,n}$ is the state space domain between SW_m, SW_{m+1} and SW_n, SW_{n+1}, where the value of the control effort is $F_i = m\,\hat{P} + n\,\hat{D}$, as shown in Fig. 2.17. Since there is no switching line at $m = 0$ and $n = 0$, the size of control effort tiles around the axes is doubled.

It is important to note, that the state space domain corresponding to a specific control effort value is bounded, while in the case of output quantization, *control effort bands* were unbounded.

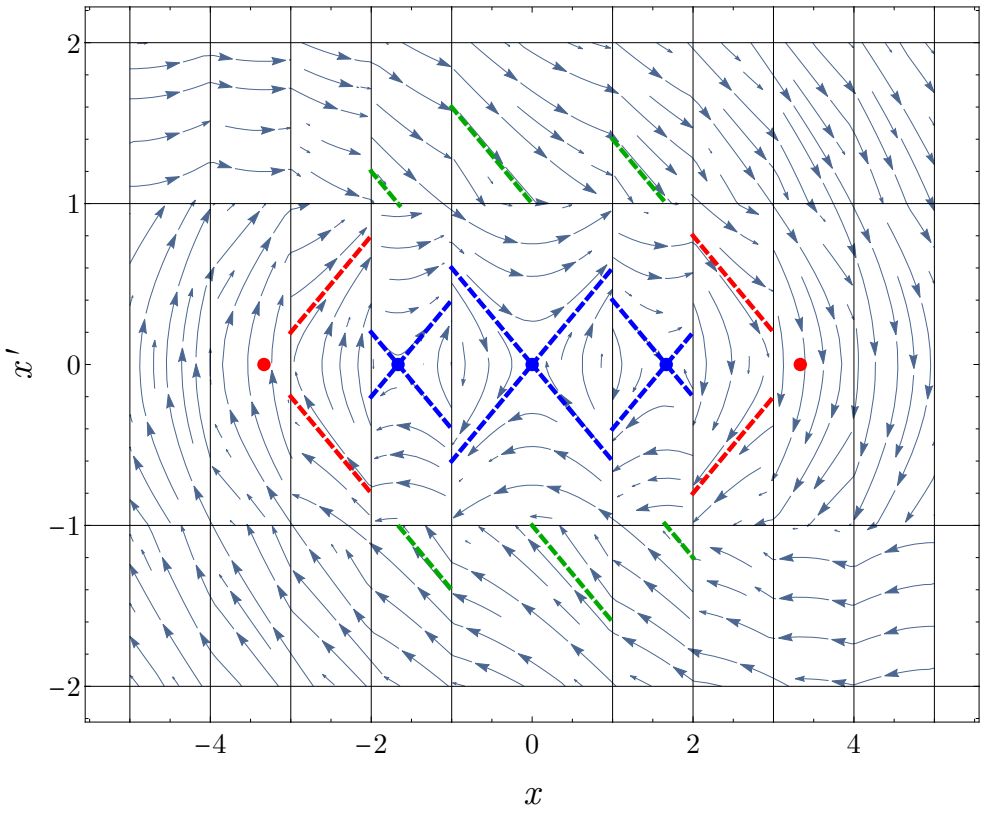

Figure 2.17: The state space of the micro-chaos map in case of input-quantization and $\hat{\alpha} = 0.6$, $\delta = 0$, $\hat{P} = \hat{D} = 0.6$. *Gray lines indicate switching lines, three regular fixed points (and their manifolds) are shown in blue, and two virtual fixed points (and their manifolds) are shown in red. Note, that due to the special choice of equal* $\hat{P}$ *and* $\hat{D}$ *parameters, the dynamics in tiles* $T_{2,0}$ *and* $T_{1,1}$ *are governed by the unstable manifold of the same virtual fixed point, according to (2.55). Green lines are the additional branches of the blue and red manifolds that are valid in the bands* $|n| = 1$.

2.6.3 Fixed points

For every control effort tile $T_{m,n}$, it is possible to express an unstable saddle point of the micro-chaos map: $\mathbf{F}^{m,n} = [x_u^{m,n} \quad 0]$, where the location can be obtained by substituting zero velocity and acceleration to the equation of motion (2.51):

$$\hat{\alpha}^2\, x_u^{m,n} = m\,\hat{P} + n\,\hat{D} \quad \rightarrow \quad x_u^{m,n} = \frac{m\,\hat{P} + n\,\hat{D}}{\hat{\alpha}^2}, \qquad m, n \in \mathbb{Z}. \tag{2.55}$$

Obviously, only the fixed points corresponding to zero velocity ($n = 0$) may reside within their corresponding control effort tiles. The condition for $\mathbf{F}^{m,0}$ to be a regular fixed point is:

$$m < \frac{m\,\hat{P}}{\hat{\alpha}^2} < m + 1, \tag{2.56}$$

that is,

$$m\,\hat{\alpha}^2 < m\,\hat{P} < (m+1)\,\hat{\alpha}^2. \tag{2.57}$$

The left inequality yields the stability condition $\hat{P} > \hat{\alpha}^2$, see Eq. (2.12), while the right inequality yields an upper bound for the index of regular fixed points:

$$m < \frac{\hat{\alpha}^2}{\hat{P} - \hat{\alpha}^2}. \tag{2.58}$$

This means, that the index of the last regular fixed point is:

$$m_{\max} = \mathrm{Int}\left(\frac{\hat{\alpha}^2}{\hat{P} - \hat{\alpha}^2}\right). \tag{2.59}$$

All other fixed points with $|m| > m_{\max}$ and $|n| > 0$ are *virtual fixed points*, that is, they do not reside in their corresponding control effort tiles, see Figure 2.17.

The stable and unstable manifolds of the fixed points correspond to the eigenvectors of $\mathbf{U}$, see Eq. (2.24).

2.6.4 Local and global behaviour

Looking at the deadzone of the velocity quantization – the domain of $n = 0$ control effort tiles – the same pattern of fixed points and strange sets can be found as in the case of output-quantization (see Section 2.3.1). The $n = 0$ control effort domain of the input-quantization is topologically equivalent to the $\hat{D} = 0$ case of output-quantization.

Figure 2.18 illustrates a case, when four separated chaotic attractors are present in the state space between fixed points $\mathbf{F}^{-2,0}$, $\mathbf{F}^{-1,0}$, $\mathbf{F}^{0,0}$, $\mathbf{F}^{+1,0}$ and $\mathbf{F}^{+2,0}$. As the damping ratio is decreased, eventually all the attractors turn to repellors and trajectories escape from the domains corresponding to $n = 0$. Figure 2.19 shows the state space with $\delta = 0$, where a larger chaotic attractor is present.

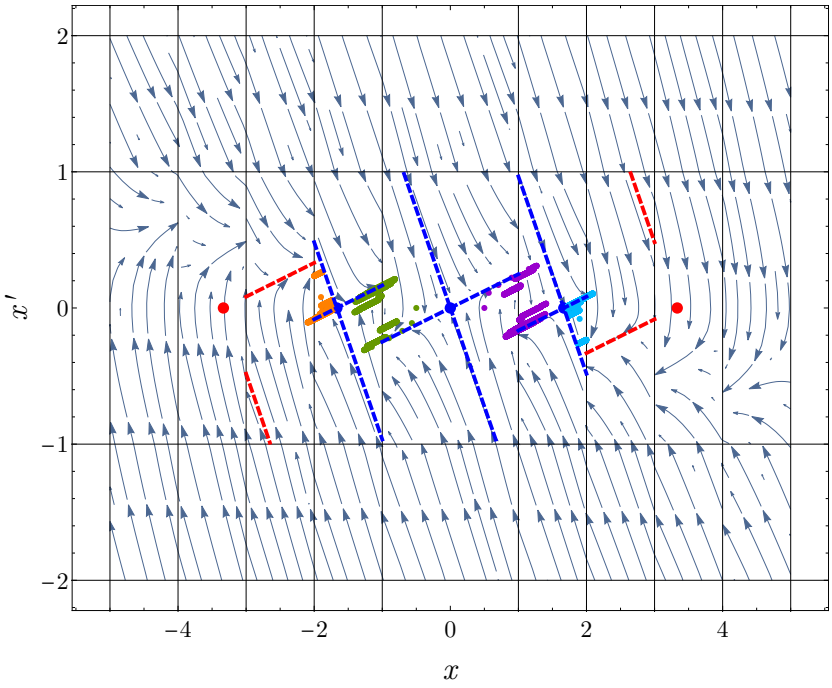

Figure 2.18: The state space of the micro-chaos map in case of input-quantization, $\hat{\alpha} = 0.6$, $\delta = 1$, $\hat{P} = \hat{D} = 0.6$. Four separated chaotic attractors (indicated with green, purple, orange and light blue) appear in the quadrangular regions between the manifolds of regular fixed points.

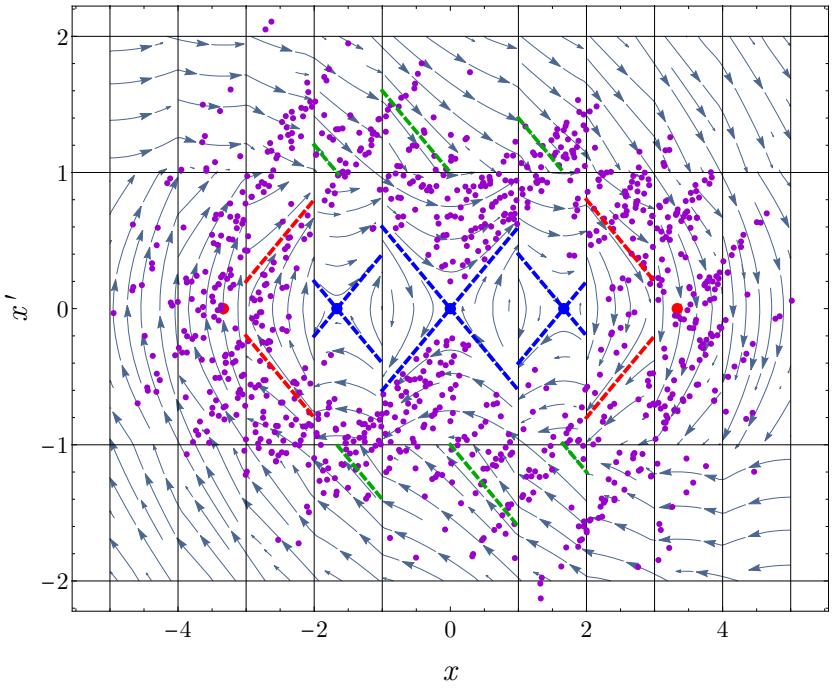

Figure 2.19: The state space of the micro-chaos map in case of input-quantization, $\hat{\alpha} = 0.6$, $\delta = 0$, $\hat{P} = \hat{D} = 0.6$. An example attractor is shown in purple. One can see, that the quadrangular regions between the manifolds (indicated with blue) of regular fixed points are repelling.

The global behaviour (in control effort tiles $|n| > 0$, $|m| > m_{max}$) of the micro-chaos map with input quantization is also governed by fixed points, which are virtual ones based on Section 2.6.3.

As a trajectory moves from one control effort tile to another, the control effort switches to a new value ($F_i = m\,\hat{P} + n\,\hat{D}$) and the governing virtual fixed point will be an other one at $x_u^{m,n} = (m\,\hat{P} + n\,\hat{D})/\hat{\alpha}^2$.

This dynamics often leads to a recurrent motion (see Fig. 2.21), where the locally (unstable) hyperbolic dynamics corresponding to a series of virtual fixed points form a stable, globally focus-like structure.

Figure 2.20 shows control effort tiles corresponding to the same control effort value with the same colour shading and manifolds with matching colours. For illustrative purposes $\hat{P} = \hat{D}$ was chosen, since the same fixed points and manifolds are valid in control effort tiles with the same $m + n$ value. For different $\hat{P}$ and $\hat{D}$ parameters, different fixed points would correspond to the control effort tiles, according to Eq. (2.55), and it would be inconvenient to present them in the state space. Still, a similar qualitative behaviour could be observed.

The chaotic trajectory varies during the recurrent motion, still it can happen, that it cycles through the same set of control effort tiles. Therefore the series of governing fixed points will be periodic in this case.
This kind of shadowing can be observed when a chaotic trajectory is examined by the Simple Cell Mapping method [35]. During the application of this method, chaotic motion is covered with long, periodic orbits. For further details, refer to Chapter 3.

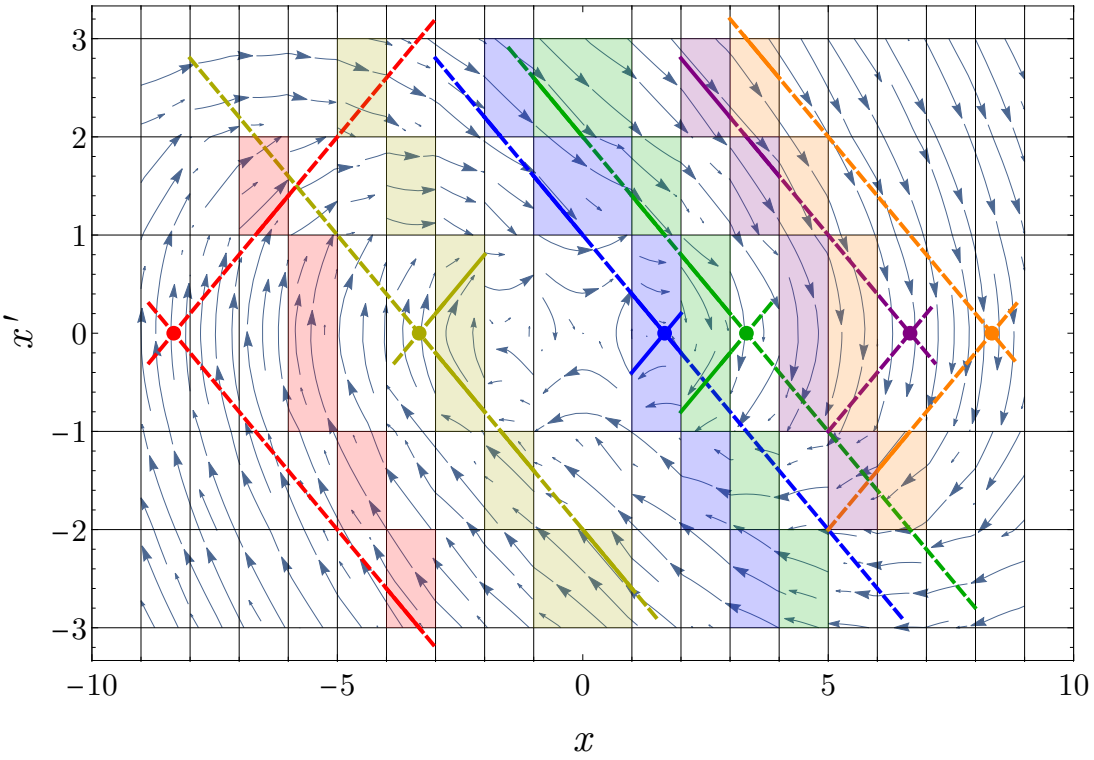

Figure 2.20: Illustration of the state space of the 2D micro-chaos map with input quantization. Coloured regions are control effort tiles corresponding to the same control effort. Fixed points and manifolds are shown in matching colour. Since $\hat{P} = \hat{D}$, the same fixed points and manifolds are valid in control effort tiles with the same $m+n$ value. The locally (unstable) hyperbolic dynamics corresponding to virtual fixed points form a stable, globally focus-like structure.

Looking at the state space from a distance, the global dynamics resembles to the focus-like phase portrait of the stabilized system $\mathbf{S} = \mathbf{U} + \mathbf{b} \otimes [\hat{P}, \hat{D}]^T$, see Figure 2.21.

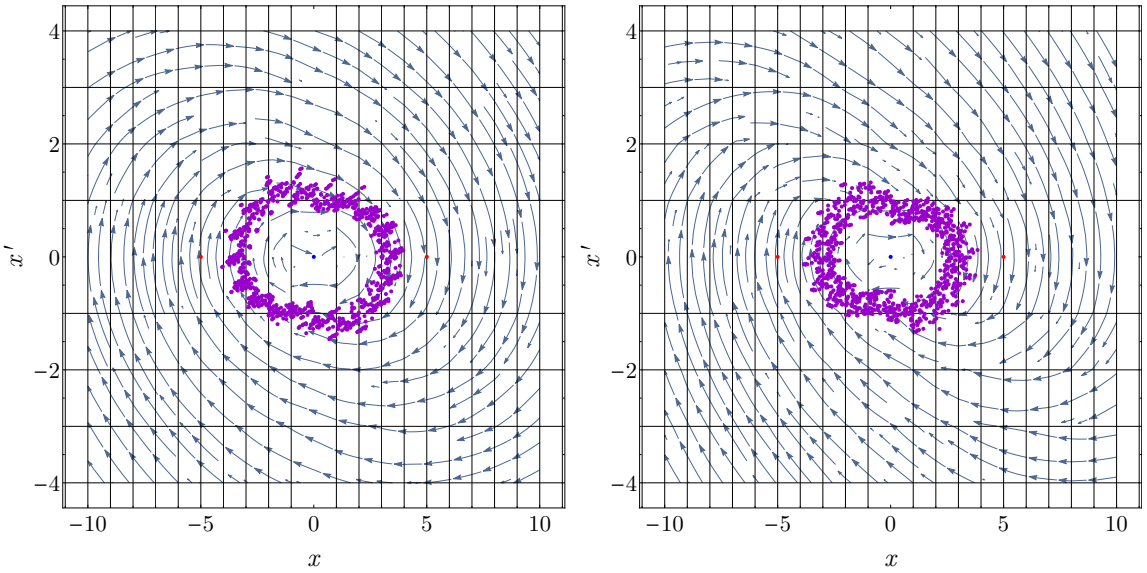

Figure 2.21: The state space of the micro-chaos map in case of input-quantization, $\hat{\alpha} = 0.1$, $\delta = 0$, left: $\hat{P} = \hat{D} = 0.2$, right: $\hat{P} = 0.2$, $\hat{D} = 0.4$. For smaller $\hat{\alpha}$ values, a recurrent orbit appears around the $m = n = 0$ deadzone.

As it can be seen, there are many similarities between the output- and input-quantization cases, in terms of state-space topology. However, the input-quantization scenario requires more effort to handle, due to the independent quantization of every state space variable and the increased number of virtual fixed points, which should be taken into account.

For example, one needs to maintain a wider set of symbols corresponding to control effort values when generating periodic orbits with the symbolic dynamics approach introduced in Section 2.4.3.

In practice, maximal possible control error is a very important property of the control system. As it was shown in Section 2.4.2 the control error can be characterized with the size of an estimated absorbing region. During the calculation of the dimensions of the absorbing cuboid, a correction term corresponding to every state variable's quantization should be taken into account. Micro-chaos map (2.52) can be rewritten as:

$$\mathbf{y}_{i+1} = \mathbf{S}\,\mathbf{y}_i - \mathbf{b}\,(\hat{P}\,\chi_{1,i} + \hat{D}\,\chi_{2,i}), \qquad \chi_{1,i}, \chi_{2,i} \in (-1, 1). \tag{2.60}$$

Here $\mathbf{S} = \mathbf{U} + \mathbf{b} \otimes [\hat{P}, \hat{D}]^T$. Repeated application of the map corresponds to the following expression:

$$\mathbf{y}_{j+1} = \mathbf{S}^j\,\mathbf{y}_0 - \sum_{k=0}^{j-1} \mathbf{S}^k\,\mathbf{b}\,\hat{P}\,\chi_{1,k} - \sum_{k=0}^{j-1} \mathbf{S}^k\,\mathbf{b}\,\hat{D}\,\chi_{2,k}. \tag{2.61}$$

With the same approach as described in Section 2.4.2, $\lim_{j\to\infty}\|\mathbf{S}^j\| = 0$, and the limit of all possible solutions can be written as:

$$\|\mathbf{y}_\infty\| = \max_{\chi_1,\chi_2} \left\| \lim_{j\to\infty} \sum_{k=0}^{j} \left(\mathbf{S}^k\,\mathbf{b}\,\hat{P}\,\chi_{1,k} + \mathbf{S}^k\,\mathbf{b}\,\hat{D}\,\chi_{2,k} \right) \right\|. \tag{2.62}$$

Here $\chi_1 = \{\chi_{1,1}, \chi_{1,2}, \dots \chi_{1,k}\}$ and $\chi_2 = \{\chi_{2,1}, \chi_{2,2}, \dots \chi_{2,k}\}$ are sequences of fractional parts corresponding to the quantization of x and x' respectively.

Introducing $\mathbf{D}$ as the diagonal matrix of eigenvalues (λ_i) and $\mathbf{T}$, the matrix formed by the columns of right eigenvectors of $\mathbf{S}$, Eq. (2.62) can be written as:

$$\mathbf{y}_\infty = -\mathbf{T} \sum_{k=0}^{\infty} \mathbf{D}^k \, \mathbf{T}^{-1} \, \mathbf{b} \, \hat{P} \, \chi_{1,k} - \mathbf{T} \sum_{k=0}^{\infty} \mathbf{D}^k \, \mathbf{T}^{-1} \, \mathbf{b} \, \hat{D} \, \chi_{2,k}. \tag{2.63}$$

The approach shown in Section 2.4.2 leads to:

$$\mathbf{y}_\infty = \cdots = \begin{bmatrix} \sum_{k=0}^{\infty} \sigma_{1,k} \, (\hat{P} \, \chi_{1,k} + \hat{D} \, \chi_{2,k}) \\ \sum_{k=0}^{\infty} \sigma_{2,k} \, (\hat{P} \, \chi_{1,k} + \hat{D} \, \chi_{2,k}) \\ \vdots \\ \sum_{k=0}^{\infty} \sigma_{n,k} \, (\hat{P} \, \chi_{1,k} + \hat{D} \, \chi_{2,k}) \end{bmatrix}. \tag{2.64}$$

To maximize the i^{th} component of $\mathbf{y}_\infty$, the following choice of the k^{th} fractional part should be made:

$$\begin{aligned} \chi_1^i = \{\chi_{1,k}\} &= \left\{ \text{sign}(\sigma_{i,k} \, \hat{P}) \right\}, \qquad k = 0, 1, 2, \dots \\ \chi_2^i = \{\chi_{2,k}\} &= \left\{ \text{sign}(\sigma_{i,k} \, \hat{D}) \right\}, \qquad k = 0, 1, 2, \dots . \end{aligned} \tag{2.65}$$

Consequently, if the sign of $\hat{P}$ and $\hat{D}$ is the same, the same fractional part set $\chi \equiv \chi_1 = \chi_2$ maximizes the i^{th} component.
Similarly as in Section 2.4.2, a global *absorbing cuboid* can be defined by taking components of $\mathbf{y}_\infty$ with the substitution of the corresponding sets of fractional parts χ_1^i and χ_2^i which maximize that component.

2.7 Main results

I have examined the general behaviour of 2D micro-chaos maps corresponding to a digitally controlled 1 DoF mechanical oscillator with sampling and quantization. The thorough analysis of the case with negative stiffness and quantization at the output revealed the existence of a characteristic pattern in the state space. It was found that chaotic attractors (or repellors) and fixed points are situated alternately along the x coordinate axis.

Various methods were generalized to higher dimensional systems, e.g., the calculation of Lyapunov exponents and the periodic orbits. Special attention was devoted to the determination of the size of the so-called absorbing domain, since this property characterizes the maximal control error $\|\mathbf{y}_\infty\|$. A formula was derived for the estimation of $\|\mathbf{y}_\infty\|$ that was successfully applied to a 4D micro-chaos map.

Main Result 1: Topological pattern

An alternating pattern of chaotic attractors or transient chaotic repellors and fixed points is present in the state space of the digitally controlled 1 DoF mechanical oscillator if proportional-derivative control scheme is applied with sampling, zero-order-hold and quantized output. Depending on the parameters, border collision bifurcations of fixed points at the switching lines can change this pattern. Moreover, crisis bifurcations can turn attractors to repellors.

Related publications: [23, 7]

Main Result 2: Absorbing cuboid

An upper bound was given for the control error of the micro-chaos map, by re-formulating it as a stabilized system without quantization and with additional correction terms corresponding to the neglected fractional parts.
In case of output-quantization, the farthest possible point of the invariant set is expressed in the form:

$$\mathbf{y}_\infty = \lim_{j\to\infty} \sum_{k=0}^{j} \mathbf{S}^k \mathbf{b}\, \chi_k = \cdots = \begin{bmatrix} \sum_{k=0}^{\infty} \sigma_{1,k}\, \chi_k \\ \vdots \\ \sum_{k=0}^{\infty} \sigma_{n,k}\, \chi_k \end{bmatrix}.$$

The choice of the infinite sequence of fractional parts χ_k that maximize the i^{th} component of $\mathbf{y}_\infty$, is $\chi^i = \{\chi_0, \chi_1, \ldots, \chi_k, \ldots\} = \{\text{sign}(\sigma_{i,0}), \text{sign}(\sigma_{i,1}), \ldots, \text{sign}(\sigma_{i,k}), \ldots\}$, which yields a close upper bound to the control error.
This approach can be adapted to the case of input quantization, where multiple fractional part sets correspond to the quantization of state variables.
By taking the separately calculated maxima for each component of $\mathbf{y}_\infty$, an *absorbing cuboid* was expressed which can be used to provide an absorbing region in the state space.
A practically usable algorithm was also developed for the determination of periodic orbits. This algorithm is based on a symbolic dynamics-based description of the phase-space and can be utilized to verify the control error estimation provided by the absorbing cuboid.

Related publications: [7, 25, 26]

It should be noted, that the upper bound corresponding to other norms can be given based on the separately calculated maximized components, as well, but these estimations

will be excessive due to the fact that every component was maximized with a different choice of χ_k.

3

Clustered simple cell mapping

This chapter introduces an extension to the Simple Cell Mapping (SCM) method [35]. While SCM offers a fast and elegant way to find state space objects in a given state space region, it is often difficult to select this particular, interesting region without preliminary analysis.

The extension allows one to combine two SCM results and thus creating a cluster of solutions, moreover a simple strategy is provided to automatically extend this cluster with new state space regions. This way, Clustered SCM can be used to adaptively discover state space objects which were outside of the initial domain.

The method is divided into two stages, first trajectories (cell sequences) leading from one SCM to a known object in the other are classified. Afterwards, the key step of the method, the cell tree mapping is carried out to resolve the non-trivial entanglement of the trajectories. This enables the method to discover new periodic orbits situated at the boundary of the joined SCM solutions.

3.1 Cell mapping methods

Cell Mapping methods (or shortly CM methods) were introduced by C.S. Hsu [35], in order to make the quick and thorough global analysis of nonlinear systems possible. CM methods discretize a region of the state space, thus creating the so called cell state space. For each cell one or more image cell is assigned (to where the dynamics lead from that cell), and by analysing the resulting graph or Markov-chain, periodic orbits, fixed points and their domains of attraction can be found.

The simplest CM method is the Simple Cell Mapping (SCM) and in the simplest case the cell state space is an n-dimensional grid of cells of the same size. The basic idea of the SCM method is that each cell has a single image, which is usually determined using the Centre Point Method [35], namely, a single trajectory from the centre of the *cell domain* is examined. In other words, all states within a cell are *mapped* to a single cell. Due to this property, the method is able to classify cells either as *periodic* cells (belonging to a periodic group) or *transient* cells (leading to a periodic group). Successful classification of all cells forms the *solution of the SCM*.

There are many variation of the CM methods. Usually a relatively fast CM method (for example SCM) is applied to the initial state space region, then further analysis is carried out at certain locations, using more advanced methods (Generalized Cell Mapping, for instance),

typically with refined cell state space [53], [55], [16]. These methods are excellent if the *interesting region* of the state space is known, but if that is not the case, a method capable of automatically extending the analysed state space region could be more suitable. The goal of the present chapter is to extend the Simple Cell Mapping with such capability.
To emphasize the relevance of adaptive state space extension, one could recall the following situations:

- The dynamical system has an expectedly complex state space and the enclosing region of state space objects is not known.
- The dynamical system has more than one attractor, and not all of them are found in the initial state space region. Escaping trajectories indicate the possible direction of other attracting structures.
- A lower dimensional state space object, e.g., a basin boundary is being followed.
- Examination of global bifurcations or crises in dynamical systems in cases when the structure and/or the size of state space objects change abruptly during the variation of certain parameters. This situation is typically encountered in piecewise smooth systems.
- Analysis of diffusion-like processes, for example intermittent maps [39].

My approach to solve the problem of state space extension is to find an adjacent region to the initial state space, to where most of the trajectories escape. Afterwards, a separate CM solution is calculated on that region and the two solutions are joined. Upon the joining procedure, new state space objects residing on the boundary of the two cell state spaces are also discovered. This chapter introduces this extension, particularly for the Simple Cell Mapping method, because it is the simplest adequate method to discover all objects in the state space [35]. The method of joining separate SCM solutions to a cluster of SCM solutions is referred to as *Clustered SCM method*. Based on these results, optional later analysis can be carried out using more advanced CM methods [54].
As an example of application, the analysis of the *micro-chaos map* (2.19) is shown, where multiple disconnected attractors – possibly consisting of distinguishable communicating repellors – are present in the state space. The behaviour of this piecewise smooth system fits into most of the aforementioned situations, as it exhibits a pattern of chaotic attractors and crisis phenomena with the appearance or disappearance of chaotic attractors/repellors [7].

3.1.1 Definitions and abbreviations

This section describes the basics terms, definitions and properties related to the Simple Cell Mapping, which are used throughout the chapter. Also some auxiliary subroutines are presented, which are necessary for the implementation of the method (see Figure 3.1).

- *Cell state space* (CSS): the bounded and discretized state space region, which is continuously covered by arbitrary *cell domains*. In the simplest case n-dimensional rectangular cuboids of the same size can be used to discretize an n-dimensional state space.
- *Cell domain*: bounded domain of the state space, part of the *cell state space*. In the simplest case it can be represented by a centre point in the state space and lengths along each dimension.
- *Cell*: object having its unique *index* referencing to a *cell domain* and various properties (e.g. *image*, *pre-image*).
- *Cell index* (or shortly *index*): cell property; a unique identifier.
- *Image*: property of a cell, one or more reference to other cells. The dynamics from the *cell domain* corresponding to the cell lead to the *cell domain(s)* indexed by the *image(s)*.

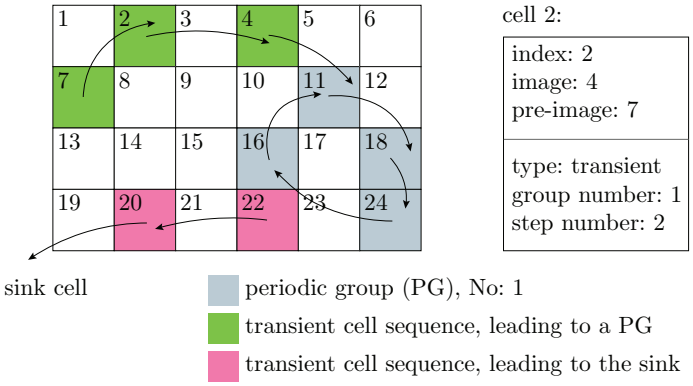

Figure 3.1: Explanation of the definitions introduced in Section 3.1.1

- *Pre-image*: property of a cell, one or more reference to other cells. The dynamics from the *cell domain(s)* indexed by the *pre-image(s)* lead to the *cell domain* corresponding to the cell.
- *Sink cell* (SC): a special *cell* indexing the unbounded region of the state space outside the CSS. Once a trajectory enters the sink, its evolution is no longer followed. To express this property, the *image* of the sink is itself by definition.
- State-to-index (or shortly *index()*) function: is a surjective function returning the *index* corresponding to the *cell domain* covering the given point in the state space.
- Index-to-domain (or shortly *domain()*) function: is a bijective function returning the *cell domain* representation for the given *index*.
- *Cell sequence*: A set of cells formed by tracking the *image* of cells subsequently. (See cells $\{7, 2, 4, 11, 18, 24, 16\}$ in Figure 3.1.)
- *Periodic group* (PG): A part of a cell sequence, that might constitute a periodic motion. A periodic cycle of n cells forms a periodic group, with periodicity n (or shortly an n-P group). Each cell within the PG is a *periodic cell* with period n, or shortly n-P cell [35]. (For example, the sink cell is a 1-P cell and forms a 1-P group.)
- *Transient cell*: Cell sequences leading to an n-P cell contain an n-P group at the end of the sequence. All other cells within the sequence are *transient* cells leading to that periodic group, forming a *transient cell sequence*.
- *Transient cell sequence*: cell sequences with their destination n-P cells removed form a *transient cell sequence*, see Figure 3.1.
- *Group number* (g): For each periodic group a unique group number is assigned. All periodic cells within a PG and all transient cells leading to that PG have the same specific group number assigned.
- *Step number* (s): property of a cell, the number of steps required to reach a PG. *Periodic cells'* step number is $s = 0$, while *transient cells'* step number is $s > 0$.
- *Domain of Attraction* (DoA): the DoA of a PG with group number g is the set of (transient) cells with the same group number g and positive step numbers $s > 0$. The Domain of Attraction can be thought as the discretization of the *Basin of Attraction* (see [46], [1] and for its numerical exploration [47].)
- *SCM solution*: After the successful execution of the SCM method, besides the initial cell properties, the *group number* and *step number* properties are assigned to each cell. At this stage all periodic groups and their domain of attraction are found, and the cell state space and its properties form the *SCM solution*.

3.2 Joining two SCM solutions

This section describes the procedure of joining two SCM solutions with non-overlapping cell state spaces. No other restrictions apply to the cell state spaces, even non-adjacent regions can be joined. First, the possible relationships between cells of the SCMs are examined, then the algorithm of joining is explained supported by a pseudo-code of the procedure.

The following conventions regarding the *SCM solutions* are adopted to aid the joining procedure.

- Group number $g = 0$ is assigned to the sink cell. Also the sink cell's index is 0.
- A new property, called *cell mapping index* (shortly: *cmid*) is assigned to each cell as an extension to its *group number* indicating which SCM contains the group referenced by the *group number*. Initially all SCM solutions have a unique *cmid*, and all cells within an SCM solution have that same *cmid*.
- Cells have an auxiliary *state* property, which can take any of the following three values: UNTOUCHED, UNDER_PROCESSING, PROCESSED. This property is used to keep track of the solution procedure.

3.2.1 Relationship of two SCM solutions

Upon joining two SCM solutions, transient cell sequences leading to the sink cell are examined, because these cell sequences might enter the other SCM's cell state space and lead to an object within the *united cell state space* – the union of the two cell state spaces. The state space region outside the *united cell state space* is called *reduced sink*. While examining an SCM solution's transient cell sequences leading to the original sink, the following cases can occur (Figure 3.2).

1. The *transient cell sequence* leads to a known destination:
   (a) the *reduced sink* or
   (b) a *periodic* or *transient* cell with group number $g > 0$ of the other SCM.
2. The *transient cell sequence* leads to a cell of the other SCM, which belongs to the domain of attraction of the sink (so the cell's group number is $g = 0$). This means that the final destination of the sequence is not known yet.

Considering the above cases, only Case 2 requires further analysis. Otherwise, transient cell sequences can be updated with a new group and step number (along with a new cell mapping id), corresponding to their new destination.
The procedure of joining two SCM solutions is therefore divided into two stages. Stage 1 enumerates all *transient cell sequences* and also updates those corresponding to Case 1. Stage 2 analyses the remaining sequences of Case 2.

3.2.2 Cell tree mapping

It is clear, that cell sequences leading to the other SCM's sink cell's domain of attraction (See Case 2 in Section 3.2.1) will eventually have one of the already existing periodic groups (including the *reduced sink*) as their destination, or they might form a new periodic group possibly with some extra transient cells leading to that PG.
This calls for the idea of mapping these remaining transient cell sequences onto each other (or some already determined cell). Transient cell sequences form trees called *cell trees* having a single cell as destination (which belongs to the other SCM), therefore these trees can be handled just like cells in SCM. The *image* of a *cell tree* is either a cell which was updated in

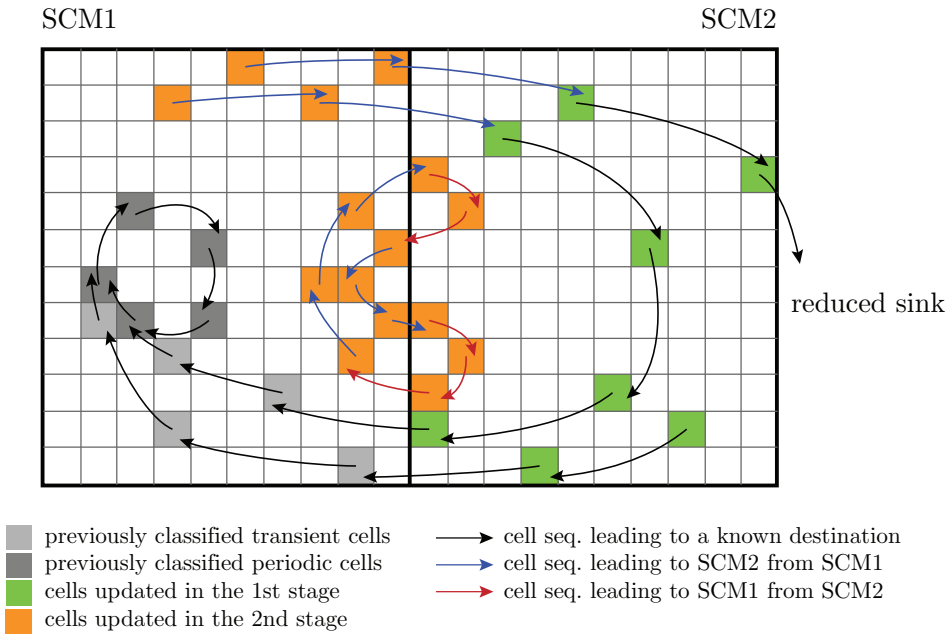

Figure 3.2: Joining of previously calculated adjacent SCM solutions. Cell sequences which lead to a known destination can be updated in Stage 1 (green cells), while sequences leading to another unclassified sequence or transient cell need further analysis in Stage 2 (orange cells). As a result, new periodic groups can be found close to the boundary of SCM1 and SCM2.

the first stage of the joining procedure (Case 1 in Section 3.2.1), or alternatively a member cell of another *cell tree* of the other SCM. Tracking the images of *cell trees* creates *tree sequences*. A *tree sequence* either leads to an already existing periodic group or forms a new periodic group and some transient cells leading to that group. Figure 3.3 illustrates two cell trees mapped to each other.
Shortly, the SCM method can be applied to the *cell trees*. If a *tree sequence* leads to a previously processed cell, all of its member cells can be tagged with the appropriate *cmid, group* and *step* numbers. Otherwise the trees form a graph containing a single cycle – the new periodic group – and branches which are transient cells belonging to that group, hence the *cmid, group* and *step* numbers can be updated. (The new periodic groups obtained this way must be added to one of the SCM solutions to have a valid *cell mapping index*.)

3.2.3 The algorithm of joining

This subsection describes the algorithm of joining adjacent SCM solutions. The algorithm is divided into preprocessing and two stages of classifying cell sequences which previously led to the sink cell.

Throughout the presentation of the algorithm, multiple SCM solutions will be examined. For the sake of simplicity, object oriented notation is used, with simple classes for describing the cell and SCM solution including the cell state space. See Algorithms 1 and 2 for these classes. In the pseudo codes the `.` (dot) operator is used to access data or function members of these objects. For instance `scm.cells[i].index` accesses the *index* of the i-th cell of the `scm` object. Furthermore, $\triangleright$ indicates clarifying comments.

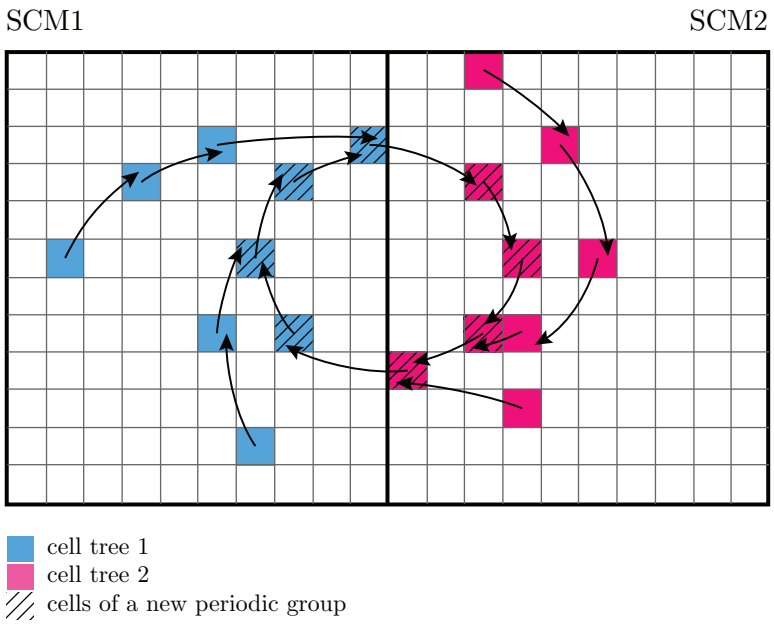

Figure 3.3: Illustration of the notion of cell tree mapping. Cell trees 1 and 2 are mapped to each other. The graph formed by them contains a cycle (new periodic group), and all other branches are transient cells leading to that group.

Algorithm 1 Class for cell

class CELL
  index $\subset \mathbb{N}$
  image $\subset \mathbb{N}$
  domain
  group $\subset \mathbb{N}$
  step $\subset \mathbb{N}$
  type $\subset$ { UNKNOWN, TRANSIENT, PERIODIC }
  state $\subset$ { UNTOUCHED, UNDER_PROCESSING, PROCESSED }
end class

Algorithm 2 Class for simple cell mapping

class SCM
  cell array of CELL objects
  cellCount $\subset \mathbb{N}$ ▷ the number of cells in the cell state space
  periodicGroupCount $\subset \mathbb{N}$ ▷ the number of periodic groups in the SCM solution
  index(...)
  domain(...)
end class

During the preprocessing the cells corresponding to the domain of attraction of the sink cell for both SCM solutions are identified. This can be done by selecting cells with group number 0, which belong to the 1-P group of the sink cell. Checking the step number is not necessary, since all cells with 0 group number must be transient cells. For the pseudo code of preprocessing see Algorithm 3 and 4.

Algorithm 3 Identification of sink cell's domain of attraction

Input: *scm* object representing an SCM solution
Output: array of indices of sink cell's domain of attraction

```
1:  function GetSinkDomainOfAttraction(scm)
2:      sinkDoA ← ∅
3:      for i ← 1, scm.cellCount do
4:          if scm.cell[i].group = 0 then
5:              sinkDoA ← sinkDoA ∪ i
6:              scm.cell[i].state ← UNTOUCHED ▷ invalidate previously processed cell
7:          end if
8:      end for
9:      return sinkDoA
10: end function
```

Algorithm 4 Preprocessing of two SCM solutions

Input: objects representing SCM solutions
Output: array of indices for both sink's domain of attraction

```
1: function Preprocess(scm1, scm2)
2:     sinkDoA1 ← GetSinkDomainOfAttraction(scm1)
3:     sinkDoA2 ← GetSinkDomainOfAttraction(scm2)
4:     return {sinkDoA1, sinkDoA1}
5: end function
```

Once the domain of attraction of the sink cell is identified for each SCM solution, the first stage of joining examines *transient cell sequences* and updates cells in Case 1 of Section 3.2.1, see Algorithm 5. The **for** loop in line 3 starts a new cell sequence by taking the next UNTOUCHED cell from the domain of attraction of the sink cell. The **while** loop in line 10 builds the cell sequence and updates all cells accordingly. If the condition in line 12 is true, then the cell sequence is still within the original cell state space. In this case the *cmid* is checked in line 14. If the currently examined cell has the same *cmid*, the current cell sequence either touches another cell sequence (line 16) and prepended to that cell sequence (thus forming a cell tree), or touches an already processed cell (line 24) in which case the cell sequence can be updated accordingly, or touches an UNTOUCHED cell (line 30) which results in continuing the current sequence by examining that cell's image.
If the condition in line 14 (*cmid* check) yields false, the cell sequence touches another cell sequence transiting to the other SCM's state space, therefore the current sequence can be updated accordingly. In cases, when $imz = 0$ is fulfilled (line 41), the cell sequence leaves the cell state space. Line 46 checks whether the current cell sequence enters the cell state space of the other SCM. In this case the sequence either touches a cell with $g \neq 0$ (line 49) when the current sequence is updated, or touches a cell with $g = 0$ (line 53) when the current cell sequence (*seq*) is stored in the array of cell trees (*cellTrees*) for further analysis. Lastly, if both cell state space have 0 (sink) index for the cell (see line 59), the current sequence leads to the reduced sink.

Algorithm 5 Stage 1 of the joining procedure

Input: Examined SCM solution and its DoA of sink, other SCM solution
Output: Updated SCM solution object *scm*, cell trees which require further processing

```
1: function STAGE1(scm, sinkDoA, otherScm)
2:     cellTrees ← ∅
3:     for i ← 0, sinkDoA.size do
4:         seq ← ∅
5:         z ← sinkDoA[i]
6:         if scm.cell[z].state = UNTOUCHED then
7:             ▷ Create new cell sequence
8:             seq ← seq ∪ z
9:             left ← false
10:            while left = false do
11:                imz ← scm.cell[z].image
12:                if imz ≠ 0 then
13:                    cmimz ← scm.cell[imz].cmid
14:                    if cmimz = cmid then
15:                        if scm.cell[imz].state = UNDER_PROCESSING then
16:                            ▷ This sequence touches another sequence under processing
17:                            left ← true
18:                            ct ← scm.cell[imz].cellTreeIndex
19:                            Tag cells in seq as UNDER_PROCESSING, assign ct as cellTreeIndex
20:                            ▷ The current sequence is prepended to cell sequence/tree
21:                            ▷ with index ct
22:                            cellTrees[ct] ← seq ∪ cellTrees[ct]
23:                        else if scm.cell[imz].state = PROCESSED then
24:                            ▷ This sequence touches an already processed cell (Case 1.b)
25:                            left ← true
26:                            g ← scm.cell[imz].group
27:                            cm ← scm.cell[imz].cmid
28:                            Tag cells in seq as PROCESSED and assign new group g and cmid cm
29:                        else
30:                            ▷ Append cell to sequence and continue
31:                            seq ← seq ∪ imz
32:                            z ← imz
33:                        end if
34:                    else
35:                        ▷ This sequence touches another seq. transiting to the other SCM (Case 1)
36:                        left ← true
37:                        g ← scm.cell[imz].group
38:                        cm ← scm.cell[imz].cmid
39:                        Tag cells in seq as PROCESSED and assign new group number g and cmid cm
40:                    end if
```

```
41:                 else
42:                     ▷ This sequence leaves the cell state space (imz = 0)
43:                     left ← true
44:                     ▷ Get image using the other SCM's cell state space
45:                     imz ← otherScm.index(step(scm.cell[z].center))
46:                     if imz ≠ 0 then
47:                         ▷ This sequence enters other SCM solutions cell state space
48:                         g ← otherScm.cell[imz].group
49:                         if g ≠ 0 then
50:                             ▷ This sequence touches a periodic group with g > 0 (Case 1.b)
51:                             cm ← otherScm.cell[imz].cmid
52:                             Tag cells in seq as PROCESSED and assign new group g and cmid cm
53:                         else
54:                             ▷ This sequence touches a transient cell of the other SCM's sink,
55:                             ▷ save this sequence for further analysis (Case 2)
56:                             Tag cells in seq as UNDER_PROCESSING and assign group g and cmid cm
57:                             cellTrees ← cellTrees ∪ seq
58:                         end if
59:                     else
60:                         ▷ This sequence leads to the reduced sink (Case 1.a)
61:                         Tag cells in seq as PROCESSED
62:                     end if
63:                 end if
64:             end while
65:         else
66:             ▷ skip cell
67:         end if
68:     end for
69:     return cellTrees
70: end function
```

In the second stage, for Case 2 in Section 3.2.1 a *cell tree mapping* is carried out (Algorithm 6). The **for** loop in line 3 starts examining an UNTOUCHED cell tree and the **while** loop in line 10 builds a sequence of cell trees (see variable: *treeSequence*). While examining the image tree ($ctImage$) of the current cell tree ($cellTrees[i]$), the following cases can occur:

- The image of the current cell tree is a cell which was updated in Stage 1 of the procedure (line 11). All cells in the sequence of trees can be updated.
- The image tree of the current cell tree is PROCESSED (line 18), therefore, the sequence of trees touches a known destination, and all cells in the sequence of trees can be updated accordingly.
- The image tree of the current cell tree is UNDER_PROCESSING (line 23), and a new periodic group and transient cells are found. All cells within the sequence of trees are examined and tagged as *periodic* (cycle in the sequence of trees) or *transient* (branches). See Figure 3.3.
- The image tree of the current cell tree is UNTOUCHED (line 29), the image tree is appended to the sequence of trees, and the examination of the tree sequence is continued.

In the end of Stage 2, all cell trees are processed and new periodic groups (if any) with their domain of attraction (transient cells) are found. The complete procedure of joining is summarized in Algorithm 7. The two SCM solutions joined this way form a cluster of cell mapping solutions, which can be further extended similarly.

Algorithm 6 Stage 2 of the joining procedure

Input: Cell Sequences Tree arrays and SCM objects
Output: Updated SCM solutions

```
1: function STAGE2(cellTrees1, cellTrees2, scm1, scm2)
2:     cellTrees ← cellTrees1 ∪ cellTrees2
3:     for i ← 0, cellTrees.size do
4:         if cellTrees[i].state = UNTOUCHED then
5:             ▷ Start examining sequence of cell trees
6:             cellTrees[i].state ← UNDER_PROCESSING
7:             treeSequence ← ∅ ∪ i
8:             processing ← True
9:             ctImage ← cellTrees[i].imageTree
10:            while processing do
11:                if ctImage = null then
12:                    ▷ There is no sequence image, image cell must be already PROCESSED in Stage 1
13:                    imageCell ← cellTrees[i].cell[0].image
14:                    Update all cells in each cell tree of the current treeSequence
15:                    Tag all cell tree in treeSequence as PROCESSED
16:                else
17:                    ▷ Cell tree mapping
18:                    if cellTrees[ctImage].state == PROCESSED then
19:                        ▷ The sequence of trees leads to a known destination
20:                        Update all cells in each cell tree of the current treeSequence
21:                        Tag all cell tree in treeSequence as PROCESSED
22:                        processing ← False
23:                    else if cellState[ctImage].state = UNDER_PROCESSING then
24:                        ▷ New periodic group and transient cells are found
25:                        g ← nextGroupNumber()
26:                        Update all cells in each cell tree of the current treeSequence
27:                        Tag all cell tree in treeSequence as PROCESSED
28:                        processing ← False
29:                    else
30:                        ▷ cellTrees[ctImage].state == UNTOUCHED
31:                        ▷ Tag this cell tree as UNDER_PROCESSING,
32:                        ▷ append to treeSequence and continue
33:                        treeSequence ← treeSequence ∪ ctImage
34:                        cellTrees[ctImage].state ← UNDER_PROCESSING
35:                    end if
36:                    ▷ Get next image sequence
37:                    ctImage = cellTrees[ctImage].imageSeq
38:                end if
39:            end while
40:        else if cellTrees[i].state = PROCESSED then
41:            ▷ Skip already processed cell tree
42:        end if
43:    end for
44:    return {scm1, scm2}
45: end function
```

Algorithm 7 Procedure of joining two SCM solutions

Input: SCM objects representing SCM solutions
Output: updated SCM objects
1: **function** JOIN($scm1, scm2$)
2: $\{sinkDoA1, sinkDoA2\} \leftarrow$ PREPROCESS($scm1, scm2$) ▷ See Algorithm 4
3: $cellTrees1 \leftarrow$ STAGE1($scm1, sinkDoA1, scm2$) ▷ See Algorithm 5
4: $cellTrees2 \leftarrow$ STAGE1($scm2, sinkDoA2, scm1$)
5: $\{scm1, scm2\} \leftarrow$ STAGE2($cellTrees1, cellTrees2, scm1, scm2$) ▷ See Algorithm 6
6: **return** $\{scm1, scm2\}$
7: **end function**

3.3 Properties and possible extensions

3.3.1 Complexity of joining

It can be seen that the complexity of calculating an SCM solution is $O(n)$ where n is the number of cells in its cell state space [51]. This comes from the fact that every cell needs constant amount of operations for initialization, and their state changes twice, first to UNDER_PROCESSING then to PROCESSED (Algorithm 8).
The complexity of preprocessing (Algorithm 3) is also linear, since the body of loop in line 3 contains constant amount of operations. For SCM solutions with cells n and m, the complexity of the preprocessing is $O(n+m)$.
The first stage of the joining procedure (Algorithm 5) contains an outer **for** loop (line 3) and an inner **while** loop (line 10), however, similarly to the SCM method, every cell is tagged with a new state maximum twice, therefore, the complexity of the first stage is $O(n)$ where n is the number of cells in the sink's domain of attraction.
Lastly, it can be seen that the complexity of the second stage (Algorithm 6) is also linear in terms of the number of total cells in the cell tree lists. This property can be shown with the same approach used in the previous case; every tree sequence is tagged with a new state maximum twice.
Introducing $n_{\text{sink}} \leq n$ and $m_{\text{sink}} \leq m$ for the number of cells in the domain of attraction of the sink cell, the complexity of the joining procedure can be written as $O(n_{\text{sink}} + m_{\text{sink}})$. The linear nature of the joining procedure can also be seen in the computation times presented in Table 3.1.

3.3.2 Simple continuous tiling of the state space

In Section 3.2 the procedure of joining two arbitrary SCM solutions was introduced. This section describes a simple algorithm for adaptively selecting an adjacent state space region (of the same shape and size as the original SCM solution) where most of the trajectories escape to. For convenience, the original cell state space is chosen to be an d-dimensional rectangular cuboid.
After selecting the initial state space region for the SCM solution one divides the unbounded outer state space region into adjacent subregions plus an unbounded non-adjacent region. To do this, the sink cell is divided into 3^d sub-regions. From these 3^d sub-regions, $3^d - 1$ are adjacent and equal size to the initial state space and the remaining region – the rest of the sink cell – is non-adjacent to the initial state space. These sub-regions are illustrated in Figure 3.4. During the calculation of the initial SCM solution, the number of cells entering these sub-regions can be counted.
Let us assume that the number of cells whose image belongs to the i-th adjacent sub-region

r_i is c_i, where $i = 1, 2, ..., 3^d - 1$. Amongst the adjacent state space regions, the one with the largest number c_k is selected. The index of the selected new adjacent state space region is

$$k = \sigma(\max(\{c_i : i = 1, 2, ..., 3^d - 1\})),$$

where $\sigma(c_k) := k$ is an index function. After solving the new SCM belonging to the newly selected region, a cluster of two SCM solutions is formed, and the procedure can be continued similarly, leading to a continuous tiling of a state space region.

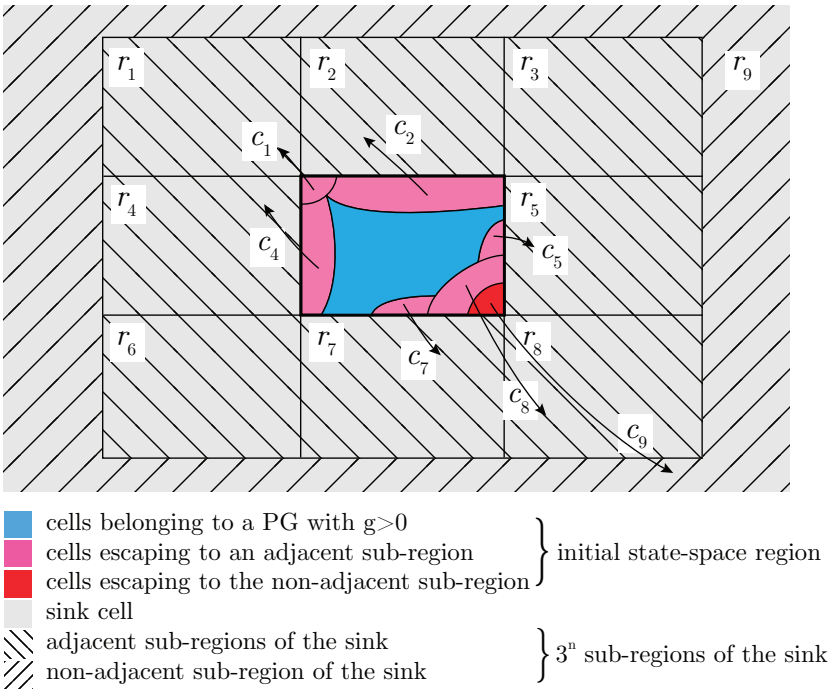

Figure 3.4: Sub-regions of the sink cell in case of a 2D cell state space. Sub-regions $r_i \ldots r_{3^d-1}$ are adjacent to the initial state space region, sub-region r_{3^d} is non-adjacent.

3.4 Application and Results

3.4.1 Analysis of the micro-chaos map

Although the Clustered SCM method is independent of the system's dimension, the results can be displayed most conveniently for systems with 2D state space. In order to demonstrate the Clustered SCM method, it is applied to the *micro-chaos map* (2.19) corresponding to an inverted pendulum with output quantization.

The quantization according to the Int() function introduces switching lines on the state space for every integer value. By examining the direction field of Equation (2.19), one can see an alternating pattern of unstable saddle points and switching lines [10], [23] see Figure 3.5.

During the application of the Clustered SCM method the resulting cluster of two SCM solutions is illustrated after every stage, by coloured images in Figures 3.6-3.11. Red colour indicates transient cells leading to the sink, other coloured regions illustrate the domain of attraction of other periodic groups. The periodic groups residing at the intersections of the x-axis and the switching lines are denoted by black dots. These PGs correspond to very small chaotic attractors of the micro-chaos map. White lines indicate the switching lines and dashed white lines denote the stable and unstable manifolds of the saddle points of the map. The initial state space region is placed on the left and the new subregion is on the right side,

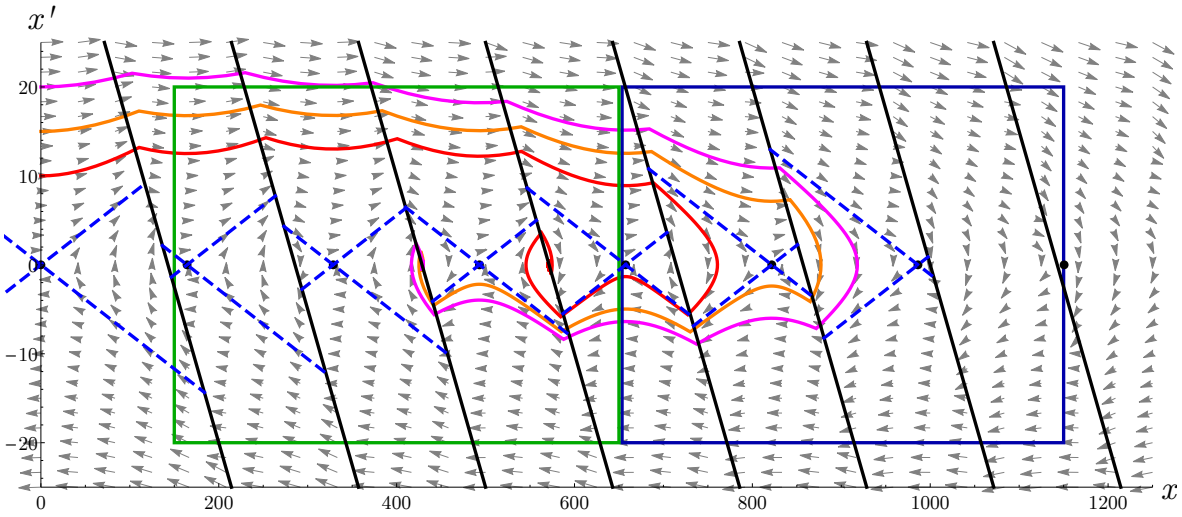

Figure 3.5: The state space of micro chaos map (2.19) at parameter values $\hat{\alpha} = 0.078$, $\delta = 0$, $\hat{P} = 0.007$, $\hat{D} = 0.02$. Dashed blue lines are the stable and unstable manifolds of saddle points. Three example trajectories leading to chaotic attractors are shown. The subsequent points of the trajectories are connected with line sections for better visibility. The green and blue rectangles show the initial and the adaptively chosen state space regions of the first example, respectively (see Figure 3.6).

since the right adjacent state space region contains the most escaping trajectories.
In the first example, no periodic groups reside at the boundary of the two state space regions (see Figure 3.6). Therefore, during Stage 1, all cells can be updated, except transient cell sequences of the initial region leading to a member cell of the domain of attraction of the new region's sink cell (see Figure 3.7). These sequences also lead to an already existing PG, but are updated in Stage 2 (as shown in Figure 3.8). The parameters of the micro-chaos map are $\hat{\alpha} = 0.078$, $\delta = 0$, $\hat{P} = 0.007$, $\hat{D} = 0.02$.

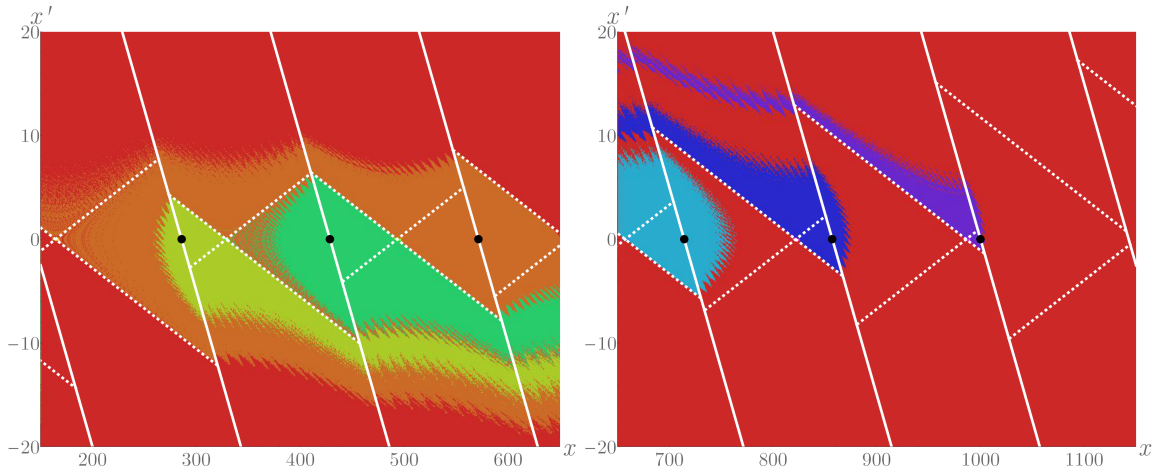

Figure 3.6: Example 1 – Illustration of initial SCM solutions before the joining procedure. The image on the left shows the initial state space region, the one on the right is the adaptively selected region. Both regions contain 3 chaotic attractors lying at the intersections of the x-axis and the switching lines.

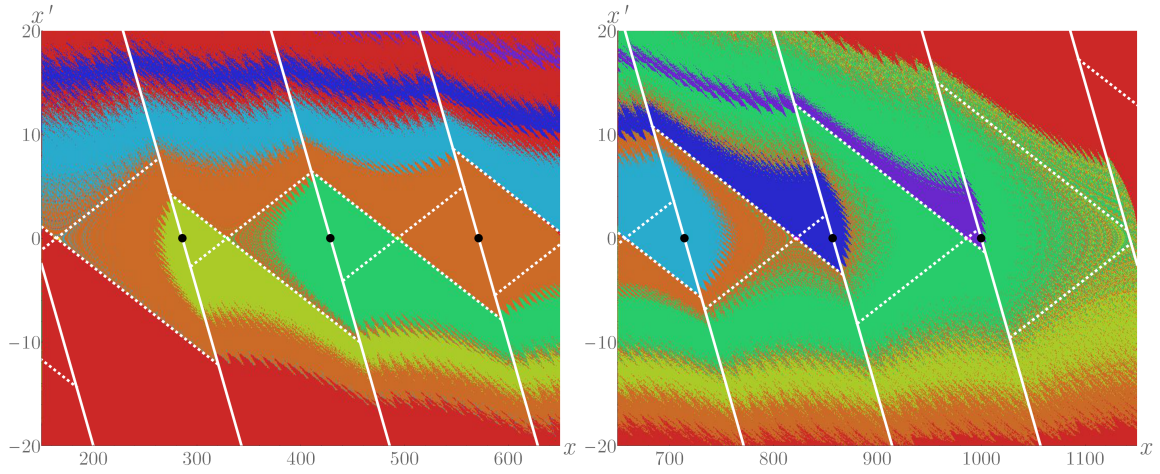

Figure 3.7: Example 1 – Illustration of SCM solutions after Stage 1 of the joining procedure. Cell sequences leading to a PG of the other SCM are updated (recoloured with the colour of the corresponding periodic group). The initial region contains some transient cell sequences which are stored for further processing in Stage 2. (See red bands at the top of the left image.)

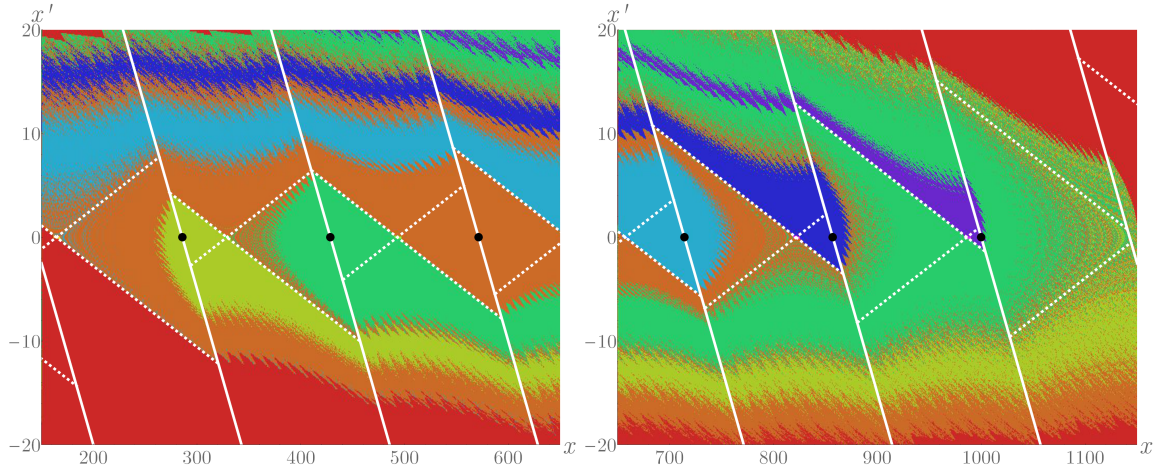

Figure 3.8: Example 1 – Illustration of SCM solutions after Stage 2 of the joining procedure. Examined cell trees are mapped to already processed cells (corresponding to the PGs with green and orange domain of attraction).

In order to show the detection of new periodic groups, another state space region is considered, for which a chaotic attractor of the map is just at the boundary of the region. The joining procedure is illustrated in Figures 3.9, 3.10 and 3.11. The parameters of the micro-chaos map are $\hat{\alpha} = 0.07$, $\delta = 0$, $\hat{P} = 0.007$, $\hat{D} = 0.02$. In the second example, a new periodic group and its domain of attraction are found during Stage 2.

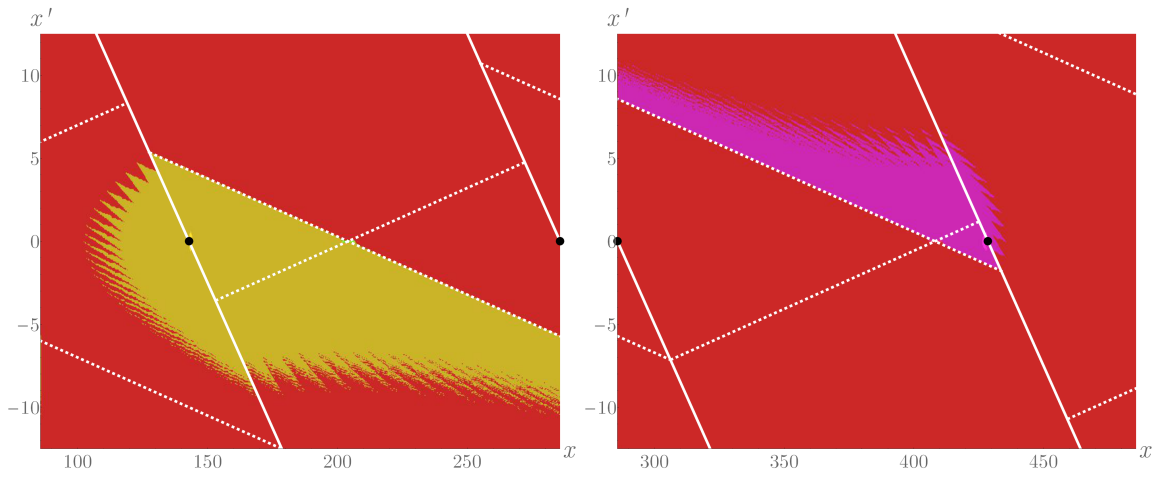

Figure 3.9: Example 2 – Illustration of initial SCM solutions before the joining procedure. The image on the left shows the initial state space region, the one on the right is the adaptively selected region. One chaotic attractor for each region is already detected (see yellow and pink domain of attractions). A third chaotic attractor is at the boundary of the two state space regions. (The black dot at the boundary of the state space regions denotes the third attractor's expected location.)

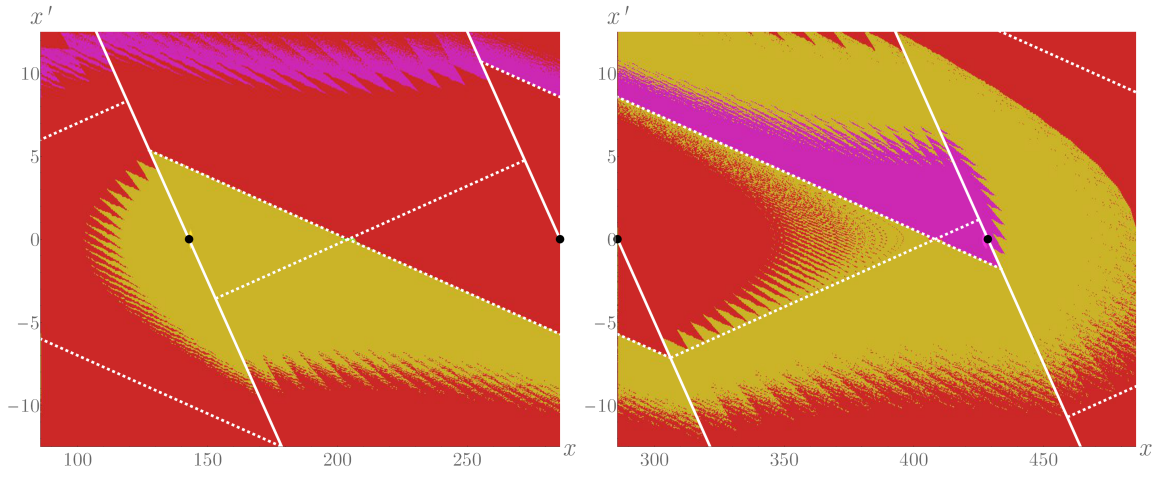

Figure 3.10: Example 2 – Illustration of SCM solutions after Stage 1 of the joining procedure. Cell sequences leading to the PG of the other SCM are updated (see yellow and pink cells). Both regions contain cell trees which are stored for further processing in Stage 2.

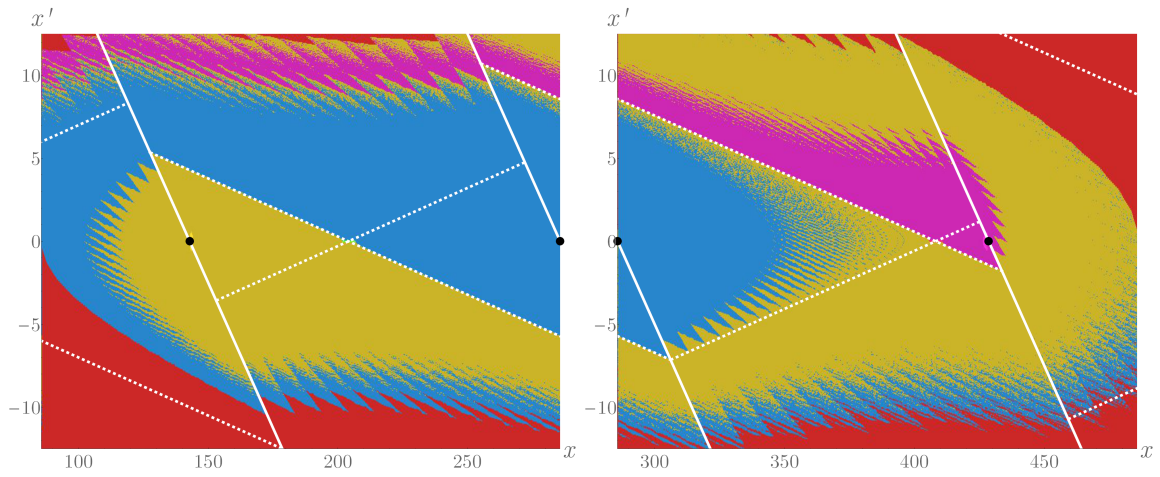

Figure 3.11: Example 2 – Illustration of SCM solutions after Stage 2 of the joining procedure. Examined cell trees are mapped to each other and a new periodic group is formed with its domain of attraction in blue.

3.4.2 Comparison of real computational efforts

To support the statements in Section 3.3.1, computation times for Example 1 are provided using the Clustered SCM. An SCM solution over the full region is also calculated for comparison (see Table 3.1 and Figure 3.12). Since the calculation of SCM1 and SCM2 can be done in parallel, the total processing time is calculated as $t_{\text{total}} = \max(t_{\text{SCM1}}, t_{\text{SCM2}}) + t_{\text{joining}}$. (Computations were carried out using 2 cores of an Intel ® Core™ i7-4700MQ CPU.)
In real situations it may happen that the two SCM solutions to be joined are of significantly different size. Consider the case when a 2D state space is displayed on the screen of a computer and the screen area is panned to move in the state space. Consequently, a separate SCM solution at the (narrow) state space region entering into the computer's screen must be calculated and joined to the already existing cluster. Computation times are checked for the case, when the original state space region is extended by 10% towards an adjacent narrow state space region (see Table 3.2). The total processing time is calculated as $t_{\text{total}} = t_{\text{SCM2}} + t_{\text{joining}}$. One can see that the use of the Clustered SCM method makes nearly real-time application possible. Moreover, further optimizations can be introduced to the method specifically for the panning application, for example, adjacent state space regions can be joined in advance, to utilize idle CPU states.
The joining time only depends on the number of cells and state space topology, while the computation time of SCM solutions also depends on the effort needed to calculate the image cells. For systems, where greater effort is necessary for the calculation of images (e.g. flows), the computation time of joining is relatively smaller compared to the complete procedure.

Number of cells	CPU time [ms]				
	t_{SCM1}	t_{SCM2}	t_{joining}	t_{total}	SCM on full region
500000	395	386	89	484	844
1000000	780	791	190	981	1573
2000000	1550	1551	418	1969	3316
4000000	3234	3225	897	4131	6752
8000000	6638	6720	1935	8655	13389

Table 3.1: Computation times for Example 1. (See Figures 3.6-3.8.)

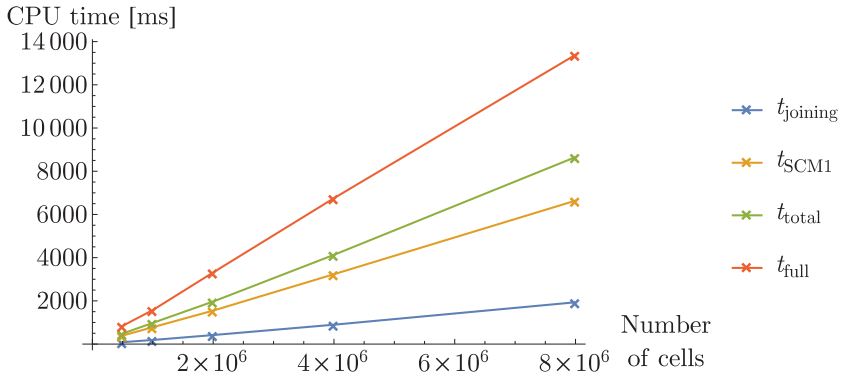

Figure 3.12: Comparison of computation times listed in Table 3.1.

Screen resolution	Number of cells		CPU time [ms]				
	n_{SCM1}	n_{SCM2}	t_{SCM1}	t_{SCM2}	t_{joining}	t_{total}	SCM on extended region
853×480	409440	40944	307	32	58	90	339
1280×720	921600	92160	661	66	129	195	740
1920×1080	2073600	207360	1581	188	361	549	1649
2880×1620	4665600	466560	3731	434	745	1179	4099
4320×2430	10497600	1049760	9689	753	1980	2733	11726

Table 3.2: Computation times for Example 1 in case of screen panning. Initially the whole computer screen is covered with the initial SCM solution (SCM1) and during panning a new SCM solution (SCM2) over a region with +10% width is added to the cluster. For comparison, the computation time of a single SCM solution on the extended state space region is included.

3.5 Main results

Main Result 3: Clustered Simple Cell Mapping

In order to adaptively discover state space objects with cell mapping approach, an extension to the Simple Cell Mapping (SCM) method was proposed. The Clustered Simple Cell Mapping method is the procedure of joining two Simple Cell Mapping solutions, thus creating a cluster of SCMs. Initially, two separate SCM solutions are present with non-overlapping and not necessarily adjacent domains of interest.
The procedure consists of two stages:

- The first stage updates transient cell sequences, which lead from one SCM domain to a known object in the other domain.
- The second stage examines cell sequences, which lead to the other domain, but to an unclassified state. The idea of *cell tree mapping* is used to discover new periodic groups situated at the boundary of the two SCM domains.

After the second stage, all cells either correspond to a known state space object or lead to the *reduced sink cell*, the state space region outside the cluster. A simple way to select an adjacent state space region to be added to the cluster is also described, enabling one to carry out Clustered SCM in an adaptive and automatic manner.
The computational effort of the method is linear in terms of the total number of cells.

Related publications: [24].

The proposed method may have an impact in various fields of application, because it offers the following advantages:

- The method allows the continuation of the SCM solution after human assessment in cases when automatic state space extension is not used, but human supervision is conducted. Solving an SCM for a new region and incorporating it into the cluster is computationally cheaper than solving an SCM over the whole extended state space (see Table 3.1).
- Parallelization of the method is trivial, as separate SCM solutions can be generated independently before the joining procedure. Also, Stage 1 of the joining procedure (for each previously calculated SCM solution) can be done in parallel.
- The method is useful in real-time situations, where the region of interest is changing as a parameter is varied. Clustered Simple Cell Mapping handles screen panning well, as a separate SCM solution at the (narrow) state space region entering into the computer's screen can be calculated quickly and joined to the already existing cluster (see Table 3.2).
- The proposed approach helps to overcome memory limitations by dividing large problems into smaller ones. During the generation of a Clustered SCM solution, if all adjacent regions of a cluster have already been examined, the SCM solution corresponding to the inner (fully surrounded) cluster can be written to disk and freed from memory. (Later, if any dynamics maps to this region, it can be reloaded from the disk.)

4

Twofold quantization

This chapter analyses the cases, when both the input (measured states) and output (control effort) of a digital controller are quantized. In Chapter 2 only the single-quantization cases were introduced and the *twofold quantization* was only mentioned briefly. In order to build up the twofold quantization case from the ground up, the example system of an inverted pendulum is used, similarly as in Section 2.3.

4.1 Formulation of quantization ratio

Consider a 1 DoF inverted pendulum that is controlled in such a way that both the measured states and the output control torque are sampled and quantized. The processing delay is neglected and the controller realizes *zero-order-hold*, as depicted in Fig. 4.1. The measured angle φ and angular velocity $\dot{\varphi}$ are quantized according to input resolution r_I, and the calculated control effort M is quantized with output resolution r_O.

After linearization, the equation of motion of the inverted pendulum assumes the following form:

$$\ddot{\varphi}(t) + 2\delta\alpha\dot{\varphi}(t) - \alpha^2\varphi(t) = -(P\varphi_i + D\dot{\varphi}_i), \quad t \in [i\tau, (i+1)\tau), \tag{4.1}$$

where α is the reciprocal of the time constant characterising the instability of the upper equilibrium position, δ is the relative damping, P and D are control parameters, τ is the sampling period and Eq. (4.1) is valid between subsequent sampling instants.

Introducing the dimensionless time $T = t/\tau$ and using the notation $\square' = \mathrm{d}\square/\mathrm{d}T$, Eq. (4.1) can be rewritten as

$$\varphi''(T) + 2\delta\hat{\alpha}\varphi'(T) - \hat{\alpha}^2\varphi(T) = -(\hat{P}\varphi_i + \hat{D}\varphi'_i), \quad T \in [i, i+1), \tag{4.2}$$

where

$$\hat{\alpha} = \alpha\tau, \quad \hat{P} = P\tau^2, \quad \hat{D} = D\tau. \tag{4.3}$$

Taking input and output quantization into account, and temporarily returning to the original control parameters (P and D) introduced in Eq. (4.1), one arrives at the following equation:

$$\varphi''(T) + 2\delta\hat{\alpha}\varphi'(T) - \hat{\alpha}^2\varphi(T) = -r_\mathrm{O}\,\tau^2\,\mathrm{Int}\left(\frac{P\,r_\mathrm{I}}{r_\mathrm{O}}\mathrm{Int}\left(\frac{\varphi_i}{r_\mathrm{I}}\right) + \frac{D\,r_\mathrm{I}}{\tau\,r_\mathrm{O}}\mathrm{Int}\left(\frac{\varphi'_i}{r_\mathrm{I}}\right)\right), \quad T \in [i, i+1).$$

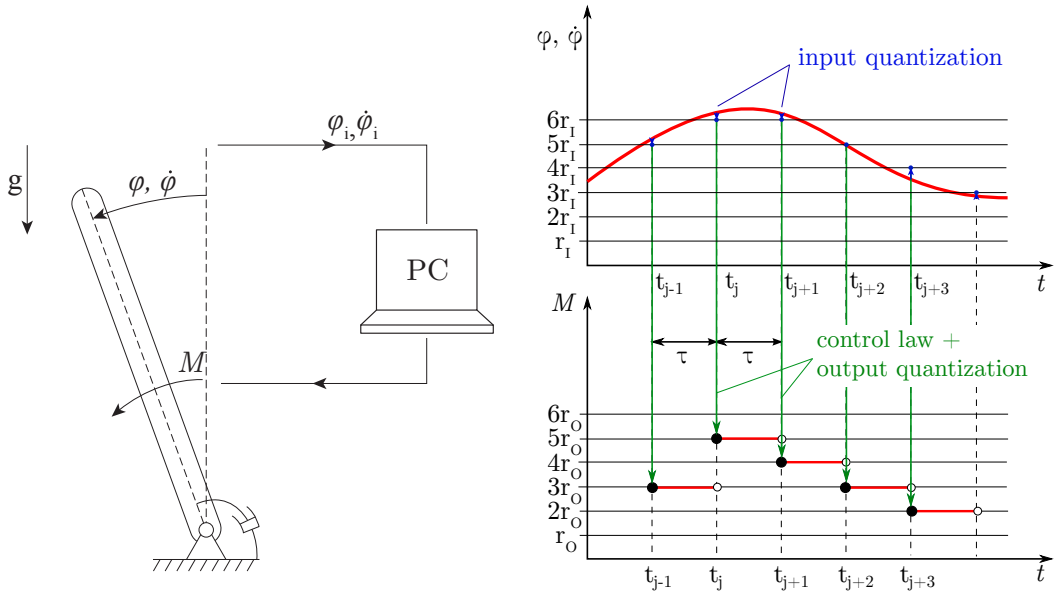

Figure 4.1: The digitally controlled inverted pendulum with the schematic representation of the zero-order-hold and quantization at the input (measured angle, angular velocity) and output (control torque).

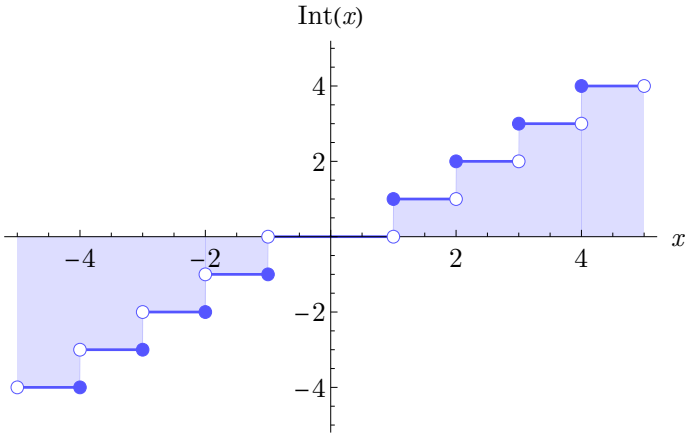

Figure 4.2: Rounding towards zero (Int); mid tread quantization with double deadzone.

According to Chapter 2, a mid-tread quantizer with double deadzone is used, that is, $\mathrm{Int}(x)$ yields the integer part of x (see Fig. 4.2).
Note, that the resolution of the angular velocity $\dot{\varphi}_i$ is r_I/τ. Thus, according to the definition of the dimensionless time T, one can write $\dot{\varphi}_i\,\tau/r_\mathrm{I} = \varphi_i'/r_\mathrm{I}$. This results in the same dimension in displacement and velocity with the same quantization resolutions, r_I at the input and r_O at the output.

In some cases, one of the quantizations is dominant over the other, and therefore the quantization with higher resolution can be neglected, and one of the *single quantization* models can be used (where either the input, or the output is quantized) [9]. However, the goal of this chapter is to analyse the joint effect of *twofold quantization* and examine the transition between the twofold and single quantization cases. Doing so, one can also highlight those ranges, where neglecting the less influential quantizer is valid.

In order to reduce the number of resolution parameters, re-scale the space coordinate with a properly chosen (see Sections 4.1.1-4.1.2) characteristic displacement X. Introducing the notations $x = \varphi/X$, $x' = \varphi'/X$ and $x'' = \varphi''/X$, the equation of motion can be rewritten as

$$x''(T) + 2\delta\hat{\alpha}x'(T) - \hat{\alpha}^2 x(T) = -\frac{r_\mathrm{O}\,\tau^2}{X}\,\mathrm{Int}\left(\frac{P\,r_\mathrm{I}}{r_\mathrm{O}}\mathrm{Int}\left(\frac{x_i\,X}{r_\mathrm{I}}\right) + \frac{D\,r_\mathrm{I}}{\tau\,r_\mathrm{O}}\mathrm{Int}\left(\frac{x_i'\,X}{r_\mathrm{I}}\right)\right).$$

To transform the output quantizer to a unit resolution one, the characteristic displacement $X_\mathrm{O} = r_\mathrm{O}\,\tau^2$ should be used. Similarly, using $X_\mathrm{I} = r_\mathrm{I}$ results in unit resolution input quantization.

4.1.1 Characteristic displacement for unit resolution output quantization

Using X_O, the equation of motion assumes the following form:

$$x''(T) + 2\delta\hat{\alpha}x'(T) - \hat{\alpha}^2 x(T) = -\mathrm{Int}\left(\frac{P\,r_\mathrm{I}}{r_\mathrm{O}}\mathrm{Int}\left(\frac{x_i\,r_\mathrm{O}\,\tau^2}{r_\mathrm{I}}\right) + \frac{D\,r_\mathrm{I}}{\tau\,r_\mathrm{O}}\mathrm{Int}\left(\frac{x_i'\,r_\mathrm{O}\,\tau^2}{r_\mathrm{I}}\right)\right).$$

Introducing $\rho_\mathrm{I} = r_\mathrm{I}/(r_\mathrm{O}\,\tau^2) = r_\mathrm{I}/X_\mathrm{O}$ one can write:

$$x''(T) + 2\delta\hat{\alpha}x'(T) - \hat{\alpha}^2 x(T) = -\mathrm{Int}\left(P\,\tau^2\,\rho_\mathrm{I}\,\mathrm{Int}\left(\frac{x_i}{\rho_\mathrm{I}}\right) + D\,\tau\,\rho_\mathrm{I}\,\mathrm{Int}\left(\frac{x_i'}{\rho_\mathrm{I}}\right)\right),$$

where $\hat{P}$ and $\hat{D}$ can be recognized (see Eq. (4.3)) and it can be seen, that ρ_I acts as a resolution for the input quantization and the output quantizer has unit resolution on the chosen scale:

$$x''(T) + 2\delta\hat{\alpha}x'(T) - \hat{\alpha}^2 x(T) = -\mathrm{Int}\left(\hat{P}\,\rho_\mathrm{I}\,\mathrm{Int}\left(x_i/\rho_\mathrm{I}\right) + \hat{D}\,\rho_\mathrm{I}\,\mathrm{Int}\left(x_i'/\rho_\mathrm{I}\right)\right). \tag{4.4}$$

4.1.2 Characteristic displacement for unit resolution input quantization

Using X_I and $\rho_\mathrm{O} = r_\mathrm{O}\,\tau^2/r_\mathrm{I} = 1/\rho_\mathrm{I}$, a similar derivation leads to:

$$x''(T) + 2\delta\hat{\alpha}x'(T) - \hat{\alpha}^2 x(T) = -\rho_\mathrm{O}\,\mathrm{Int}\left(\frac{P\,r_\mathrm{I}}{r_\mathrm{O}}\mathrm{Int}\left(x_i\right) + \frac{D\,r_\mathrm{I}}{\tau\,r_\mathrm{O}}\mathrm{Int}\left(x_i'\right)\right).$$

Exploiting the definiton of $\hat{P}$, $\hat{D}$ and ρ_O one arrives at the following equation:

$$x''(T) + 2\delta\hat{\alpha}x'(T) - \hat{\alpha}^2 x(T) = -\rho_\mathrm{O}\,\mathrm{Int}\left(\frac{\hat{P}}{\rho_\mathrm{O}}\mathrm{Int}\left(x_i\right) + \frac{\hat{D}}{\rho_\mathrm{O}}\mathrm{Int}\left(x_i'\right)\right), \tag{4.5}$$

where the input quantizer has unit resolution and ρ_O acts as a resolution for the output quantization.

In Equations (4.4-4.5), a single *quantization ratio* (ρ) characterises the ratio of input and output quantization resolutions. For large ρ_I or small ρ_O values, the input quantization dominates, and the outer quantization can be practically neglected. Similarly, for large ρ_O or small ρ_I values, the output quantization is more significant. Lastly, when the characteristic displacements X_I and X_O are equal, $\rho_\mathrm{O} = \rho_\mathrm{I} = 1$, therefore both quantizations have the same unit resolution.

It may seem, that one could continue by choosing one of the characteristic displacements X_I (and the corresponding resolution $\rho = \rho_\mathrm{O}$) or X_O (with $\rho = \rho_\mathrm{I}$) and examine the $\rho \to 0$

and $\rho \to \infty$ limits to express the single quantization cases. However, neither of the two choices are perfect, as the upper limit of quantization is

$$\lim_{\rho\to\infty} \rho \,\mathrm{Int}(x/\rho) = 0, \tag{4.6}$$

consequently the control effort turns to zero in Equations (4.4-4.5). Thus, this model does not reflect the physical properties of the single quantization controller.
Taking the lower limit, the following result is obtained:

$$\lim_{\rho\to 0} \rho \,\mathrm{Int}(x/\rho) = x, \tag{4.7}$$

which means that the twofold quantization turns to single quantization because the infinitely fine resolution quantizer yields the original signal itself (see Figure 4.3).

Consequently, it can be firmly stated, that none of the single-parameter twofold quantization equations (4.4) or (4.5) can be solely used to analyse the transition to both single quantization cases.

Therefore, Eq. (4.4) is used to examine the transition from twofold quantization to single quantization at the output ($\rho_\mathrm{I} \to 0$). Similarly, Eq. (4.5) can be used to inspect the transition to the single quantization at the input (as $\rho_\mathrm{O} \to 0$):

$$\mathrm{Int}\left(\hat{P}\,\rho_\mathrm{I}\,\mathrm{Int}\left(x_i/\rho_\mathrm{I}\right) + \hat{D}\,\rho_\mathrm{I}\,\mathrm{Int}\left(x_i'/\rho_\mathrm{I}\right)\right) \xrightarrow[\rho_\mathrm{I}\to 0]{} \mathrm{Int}\left(\hat{P}\,x_i + \hat{D}\,x_i'\right),$$

$$\rho_\mathrm{O}\,\mathrm{Int}\left(\frac{\hat{P}}{\rho_\mathrm{O}}\mathrm{Int}\left(x_i\right) + \frac{\hat{D}}{\rho_\mathrm{O}}\mathrm{Int}\left(x_i'\right)\right) \xrightarrow[\rho_\mathrm{O}\to 0]{} \hat{P}\,\mathrm{Int}(x_i) + \hat{D}\,\mathrm{Int}(x_i').$$

It is worth noting, that one can trivially switch between (4.4) and (4.5) at $\rho_\mathrm{I} = \rho_\mathrm{O} = 1$, or also can use one of the representations to examine the effect of rather large values of ρ, without switching to the other representation.

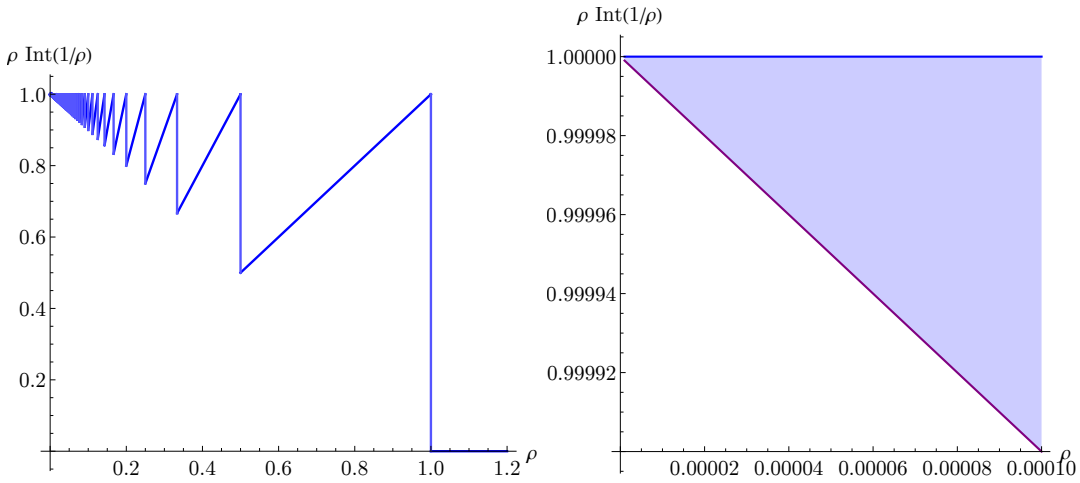

Figure 4.3: Visualisation of $\lim_{\rho\to 0} \rho\,\mathrm{Int}(x/\rho) = x$ *(for* $x = 1$*) and* $\lim_{\rho\to\infty} \rho\,\mathrm{Int}(x/\rho)$*. The values of the function* $\rho\,\mathrm{Int}(x/\rho)$ *are between the bounds* x *and* $x - \rho$*.*

4.2 Numerical analysis of the Micro-Chaos map with twofold quantization

4.2.1 Micro-Chaos map

Equations (4.4-4.5) characterise the behaviour of the inverted pendulum with sampling, PD-control and quantization at both input and output. Rewriting it as a system of first order differential equations, one can formulate its solution as:

$$\mathbf{y}(T) = \mathbf{U}(T)\mathbf{y}(0) + \mathbf{b}(T)\,F(T), \quad T \in [0,1), \tag{4.8}$$

where $\mathbf{y} = [x(T) \quad x'(T)]^T$, $\Gamma = \sqrt{1+\delta^2}$, F is the control effort,

$$\mathbf{U}(T) = \frac{e^{-\hat{\alpha}\delta T}}{\Gamma} \begin{bmatrix} \Gamma \operatorname{ch}(\hat{\alpha}\Gamma T) + \delta \operatorname{sh}(\hat{\alpha}\Gamma T) & \operatorname{sh}(\hat{\alpha}\Gamma T)/\hat{\alpha} \\ \hat{\alpha} \operatorname{sh}(\hat{\alpha}\Gamma T) & \Gamma \operatorname{ch}(\hat{\alpha}\Gamma T) - \delta \operatorname{sh}(\hat{\alpha}\Gamma T) \end{bmatrix},$$

and

$$\mathbf{b}(T) = \frac{1}{\hat{\alpha}^2\Gamma} \begin{bmatrix} \Gamma - e^{-\hat{\alpha}\delta T}\left(\Gamma \operatorname{ch}(\hat{\alpha}\Gamma T) + \delta \operatorname{sh}(\hat{\alpha}\Gamma T)\right) \\ -\hat{\alpha} e^{-\hat{\alpha}\delta T} \operatorname{sh}(\hat{\alpha}\Gamma T) \end{bmatrix},$$

as it was shown in Section 2.1.1. Substituting $T = 1$, a new type of the *micro-chaos* map [33] is obtained, which is valid at sampling instants:

$$\mathbf{y}_{i+1} = \mathbf{U}(1)\,\mathbf{y}_i + \mathbf{b}(1)\,F_i, \quad \text{where} \tag{4.9}$$

$$F_i = \operatorname{Int}\left(\rho_{\mathrm{I}}\left(\hat{P}\operatorname{Int}(x_i/\rho_{\mathrm{I}}) + \hat{D}\operatorname{Int}(x_i'/\rho_{\mathrm{I}})\right)\right) \text{ if } X = X_{\mathrm{I}},$$

or

$$F_i = \rho_{\mathrm{O}} \operatorname{Int}\left(\frac{1}{\rho_{\mathrm{O}}}\left(\hat{P}\operatorname{Int}(x_i) + \hat{D}\operatorname{Int}(x_i')\right)\right) \text{ if } X = X_{\mathrm{O}}.$$

Here F_i is the control effort between the dimensionless sampling instants $T = i$ and $T = i+1$.

It is clear, that the quantization causes the control effort F_i to be a piecewise constant function over the state space, which consists of domains, each corresponding to a specific F_i value. When the *output-quantization* is dominant, $F_i = \operatorname{Int}\left(\hat{P}\,x_i + \hat{D}\,x_i'\right)$. Thus, the aforementioned domains are parallel bands separated by parallel switching lines that can be given as

$$x' = \frac{m - Px}{D}, \quad m \in \mathbb{Z}, \tag{4.10}$$

(see Figures 4.4 and 4.6).

For the *input-quantization* case, however, these domains are rectangular areas since $F_i = \hat{P}\operatorname{Int}(x_i) + \hat{D}\operatorname{Int}(x_i')$. Consequently, the quantization results in a grid of horizontal and vertical switching lines (see Figures 4.5 and 4.6).

Based on Chapter 2, in the case of *single quantization at the output*, multiple chaotic attractors can be found in the state space, at the intersections of switching lines and the x axis, as it is illustrated in Fig. 4.4. Depending on system and control parameters, attractors may appear or disappear due to border-collision bifurcation, or some of them may become repellors, and form one or more bigger attractors, by pushing the trajectory towards each other [7].

In case of *input quantization*, the general observation is that a periodic orbit (with superimposed chaotic oscillations) appears around the internal structure of repellors. Depending on the parameters, one or more chaotic attractors spanning over multiple control effort bands can be found, see Fig. 4.5.

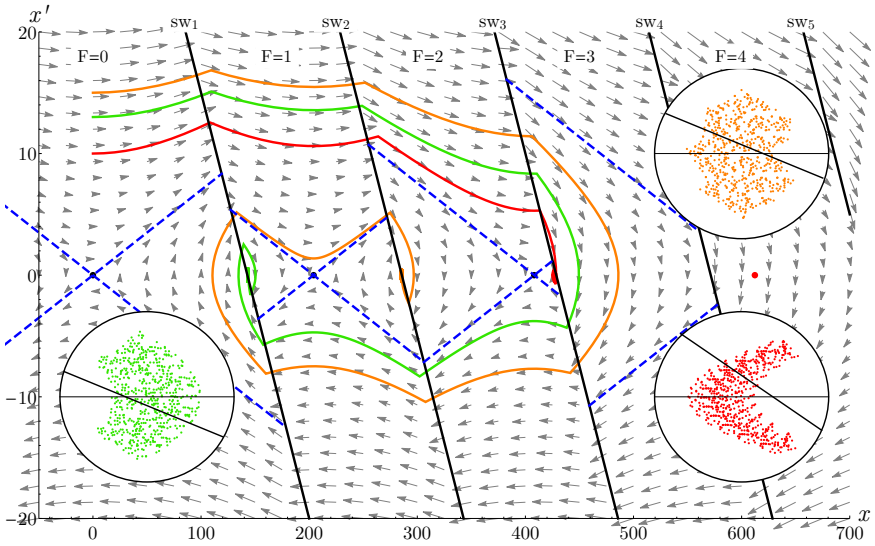

Figure 4.4: Output quantization. *State space of the micro-chaos map at* $\hat{\alpha} = 0.07$, $\delta = 0.03$, $\hat{P} = 0.007$, $\hat{D} = 0.02$, $r_{\mathrm{I}} \to 0$ *and* $r_{\mathrm{O}} = 1$. *Three example trajectories are shown starting from* $x = 0$ *and* ■: $x' = 10$, ■: $x' = 13$, ■: $x' = 15$. *The first trajectory (*■*) ends up in an attractor on the switching line between control effort bands* $F = 2$ *and* $F = 3$, *the second one (*■*) ends up in an attractor between bands* $F = 0$ *and* 1, *while the third (*■*) ends up in an attractor between bands* $F = 1$ *and* 2. *Close-up images of the attractors are also provided in the balloons with the corresponding colour.*

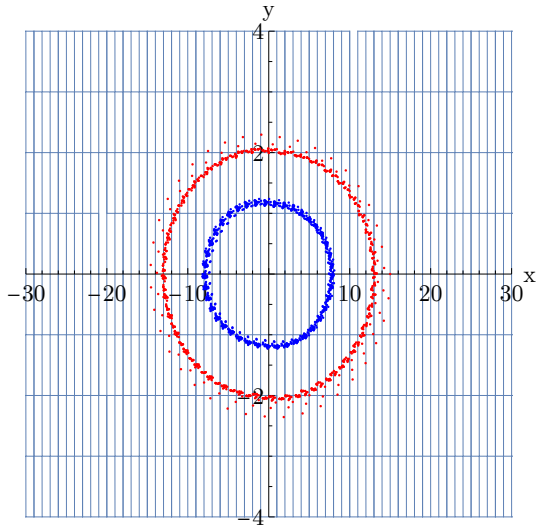

Figure 4.5: Input-quantization. Switching lines and example periodic orbits with superimposed chaotic oscillations at $\hat{\alpha} = 0.007$, $\delta = 0.$, $\hat{P} = 0.027$, $\hat{D} = 0.02$ *and* $\rho_{\mathrm{I}} = 0.8$. *Two example trajectories are shown starting from* $x' = 0$ *and* ■: $x = 8$ *and* ■: $x = 15$. *They end up in the same periodic orbits with superimposed chaotic oscillations indicated with* ■.

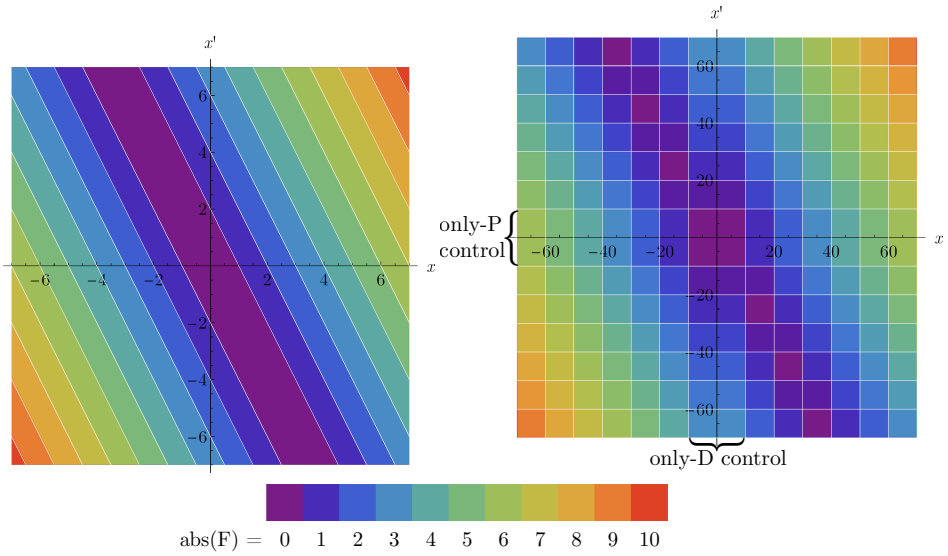

Figure 4.6: Left*: Switching lines and control effort bands in case of output quantization.* Right*: Switching line grid and control effort* tiles *in case of input quantization.*

4.2.2 Cell Mapping results

In order to explore the effect of varying the *quantization ratio* and examine the transitions from twofold to single quantization cases, Cell Mapping Methods [35] were utilized. Simple Cell Mapping (SCM) is suitable to obtain a *global picture* of a certain state space region, i.e., to find periodic orbits, fixed points and their domains of attraction. Chaotic attractors are usually covered by one or more high-period cell groups.

Utilizing *Clustered Simple Cell Mapping* ([24] and Chapter 3), it is possible to automatically extend the analysed state space region and also execute cell mapping in a parallel computing environment.

The primary goal is to express the control error, therefore the location (average of attractor's cell coordinates; x_{attr}, y_{attr}) and size (S_x, S_y) of chaotic attractors are extracted (see Fig, 4.7). In the output quantization case the attractors reside on the x-axis ($y_{\text{attr}} = 0$). Since the desired control state is the origin, any solution arriving to a specific attractor will yield a mean control error of x_{attr}.

A series of SCM solutions was generated by sweeping the parameter ρ_{I} for some fixed $\hat{\alpha}, \beta, \hat{P}$ and $\hat{D}$ values. Figure 4.8 shows the transition from $\rho_{\text{I}} = 0$ to $\rho_{\text{I}} = 16$ at $\hat{P} = 0.007, \hat{D} = 0.02, \alpha = 0.074$ and $\delta = 0$. Here the *output quantization* case has eight separated chaotic attractors (four-four on both sides, see Fig. 4.9 *top*) and as the quantization ratio increases, these attractors eventually become repellors. At $\rho_{\text{I}} = 1.28$ (see Fig. 4.9 *bottom*), the outermost attractors disappear resulting in a more favourable state space configuration in terms of control error.

The aforementioned results can be traced back to two phenomena: as it can be seen in Fig. 4.7, the *switching lines become jagged*, and consequently regions appear in the state space corresponding to only-P and only-D control (so-called *input deadzones*, see Fig, 4.6), due to the quantization of measured values. In the next section, the effect of these new deadzones is examined.

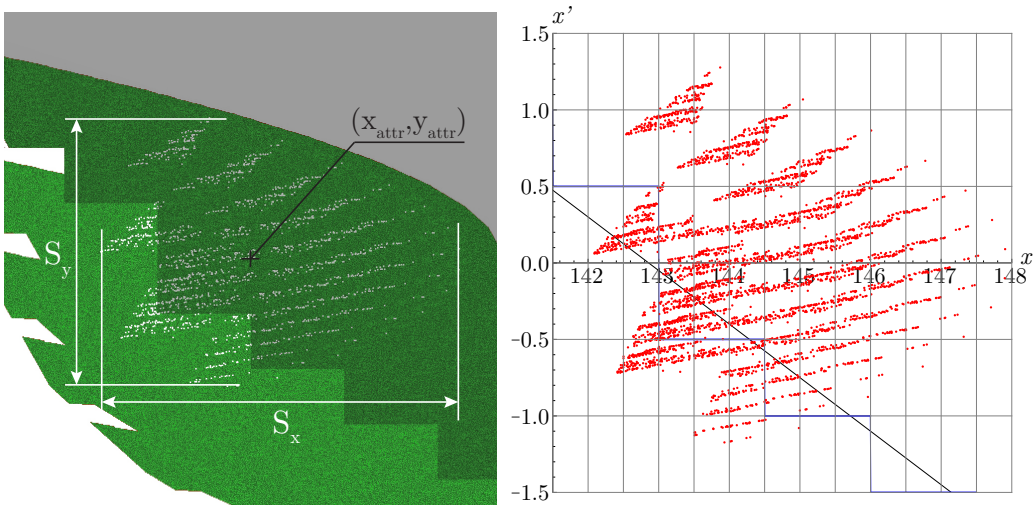

Figure 4.7: Left*: Example attractor in the twofold quantization case, obtained by SCM and illustration of extracted properties, location of attractor's averaged centre (x_{attr}, y_{attr}) and the extent along x and x' axes: (S_x, S_y).* Right*: The same attractor obtained by numerical simulation. Blue line indicates the switching line, and black straight line shows the reference switching line corresponding to output quantization.*

4.2.3 Deadzone crisis

For *output quantization*, the deadzone of the output quantizer creates an unstable band between switching lines SW_{-1} and SW_1 (see Fig. 4.4 and 4.6). On the other hand, in case of *input quantization* the two deadzones (corresponding to the measured values' quantizers) around the x and x' axes will cause the PD-control to work as only-P control for small velocities and only-D control for small displacements (see Fig. 4.6).

In the case of twofold quantization, during the variation of the quantization ratio, the borders of the *output deadzone* (uncontrolled region between the $\text{SW}_{\pm 1}$ switching lines, where the control effort is $F = 0$) and *input deadzones* (deadzones around x and x' axes, where either part of the PD-control is offline) move, thus state space objects (e.g., attractors or periodic orbits) can disappear or qualitatively change. This is called *deadzone crisis*.

To illustrate a possible scenario, consider Figure 4.10. As the quantization ratio ρ_{I} increases, the *steps* on the switching lines grow. At the intersection of the x-axis and the switching line, the switching line becomes *locally vertical* in the range of the input quantizer's deadzone and the attractor adapts to this by expanding proportionally. At a certain point – as the switching line gets close to the stable manifold of the nearby saddle point – a *deadzone crisis* happens, and the solution will be able to escape from the chaotic attractor, leaving a transient chaotic repellor behind.

During the transition from the output quantization to twofold quantization, a series of *deadzone crises* occur and eventually all chaotic attractors turn to repellors. The interactions of the repellors lead to a newly formed recurring orbit with superimposed chaotic oscillations (see Section 4.2.2 and Fig. 4.8).

Based on these results, it is obvious that the non-smooth, *stair-like* shape of the switching lines play an important role in manipulating state space objects by opening up escape possibilities from the previously closed domains of chaotic attractors.
To gain a deeper insight in this phenomenon, the following section examines the topology of switching lines.

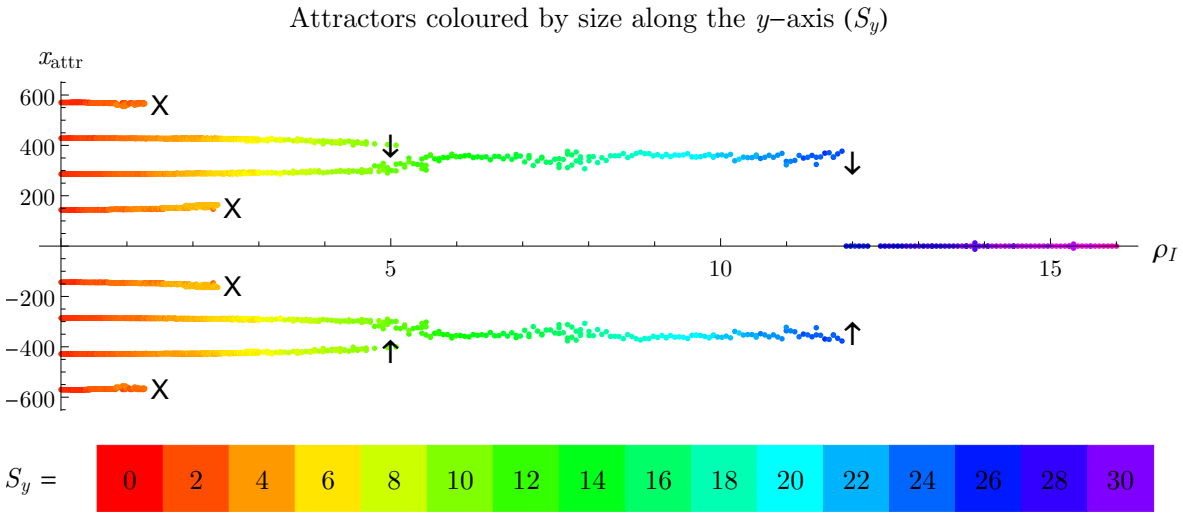

Figure 4.8: Transition from output quantization to twofold quantization. At $\rho_I \approx 1.3$, the outermost chaotic attractors, while at $\rho_I \approx 2.4$, the innermost attractors disappear due to deadzone crisis *(denoted by X). At $\rho_I \approx 4.7$ the chaotic attractors merge (denoted by arrows) on both sides and lastly at $\rho_I \approx 12$ they merge again resulting in a single recurring orbit with superimposed chaotic vibrations.*

4.3 Analysis of switching lines

4.3.1 Switching Line Collision

For the *single quantization cases*, the switching lines corresponding to different efforts of the PD-control are simple to express: parallel lines ($\hat{P}\,x + \hat{D}\,x' = m, m \in \mathbb{Z}$) for the output quantization, and a grid of lines ($x = i\,\rho_\mathrm{I}$, $x' = j\,\rho_\mathrm{I}$, $i, j \in \mathbb{Z}$) for the input quantization. In the *twofold quantization case*, however, their explicit expression is not straightforward.

In this section, Eq. (4.4) and ρ_I is used, with the implicit equation of the control effort:

$$\mathrm{Int}\left(\hat{P}\,\rho_\mathrm{I}\,\mathrm{Int}\,(x/\rho_\mathrm{I}) + \hat{D}\,\rho_\mathrm{I}\,\mathrm{Int}\left(x'/\rho_\mathrm{I}\right)\right) = m, \quad m \in \mathbb{Z}.$$

The domain of control effort band $F_i = m$ is bounded by two switching lines: $\mathrm{SW_m}$ and $\mathrm{SW_{m+1}}$, see Fig. 4.4. The equation of the lower bounding switching line is

$$\mathrm{SW_m}: \quad \hat{P}\,\rho_\mathrm{I}\,\mathrm{Int}\,(x/\rho_\mathrm{I}) + \hat{D}\,\rho_\mathrm{I}\,\mathrm{Int}\left(x'/\rho_\mathrm{I}\right) = m, \quad m \in \mathbb{Z}, \tag{4.11}$$

while the upper bounding switching line can be expressed implicitly as

$$\mathrm{SW_{m+1}}: \quad \hat{P}\,\rho_\mathrm{I}\,\mathrm{Int}\,(x/\rho_\mathrm{I}) + \hat{D}\,\rho_\mathrm{I}\,\mathrm{Int}\left(x'/\rho_\mathrm{I}\right) = m+1, \quad m \in \mathbb{Z}. \tag{4.12}$$

Expressing the quantized velocity ($\rho_\mathrm{I}\,\mathrm{Int}(x'/\rho_\mathrm{I})$) from Eq. (4.11):

$$\rho_\mathrm{I}\,\mathrm{Int}\left(x'/\rho_\mathrm{I}\right) = \frac{m - \hat{P}\,\rho_\mathrm{I}\,\mathrm{Int}\,(x/\rho_\mathrm{I})}{\hat{D}}, \quad m \in \mathbb{Z},$$

and applying the *conjugated* version (Int^*) of the rounding function used in quantizers, i.e. rounding towards infinity without deadzone (see Fig 4.11), yields the explicit formula of the switching lines:

$$x' = \rho_\mathrm{I}\,\mathrm{Int}^*\left(\frac{m - \hat{P}\,\rho_\mathrm{I}\,\mathrm{Int}\,(x/\rho_\mathrm{I})}{\hat{D}\,\rho_\mathrm{I}}\right), \quad m \in \mathbb{Z}. \tag{4.13}$$

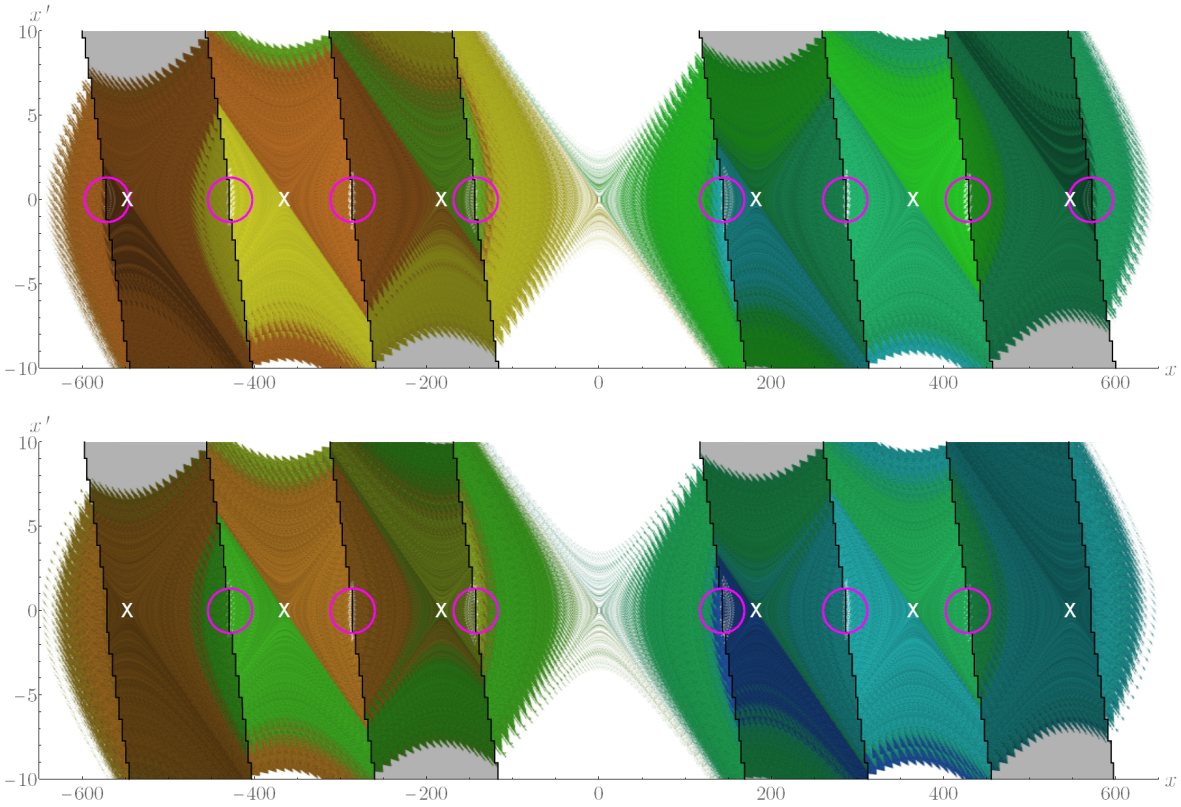

Figure 4.9: SCM results illustrating deadzone crisis. Top: *4-4 separated attractors and their domains of attraction are highlighted at* $\rho_{\mathrm{I}} = 1.247$. Bottom: *Outermost attractors disappear via* deadzone crisis *at* $\rho_{\mathrm{I}} = 1.287$. *Coloured regions indicate domains of attraction, pink circles highlight chaotic attractors, white crosses denote unstable fixed points.*

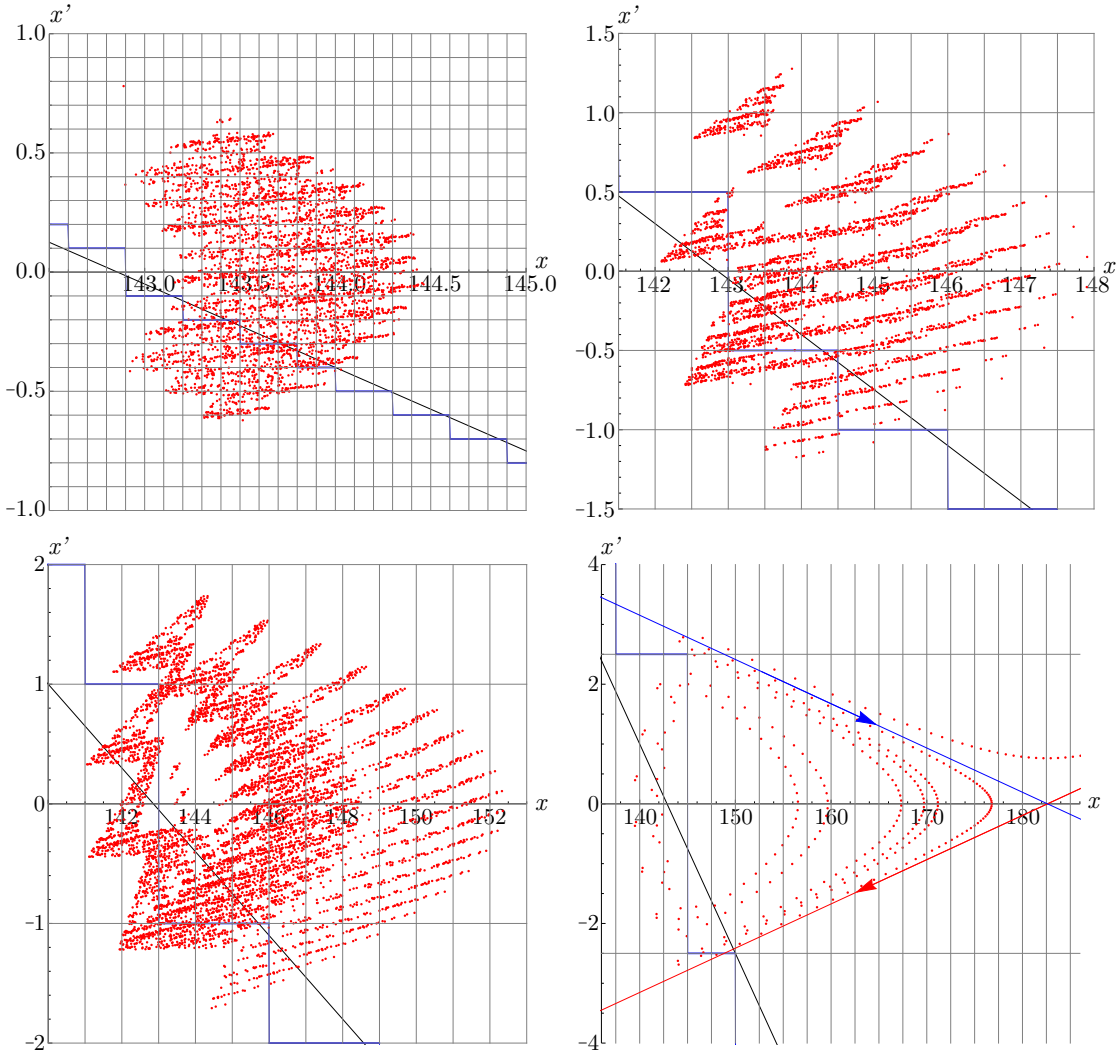

Figure 4.10: Deadzone crisis*: increasing the quantization ratio changes the switching line and the chaotic attractor around it. As the* step *around the x axis becomes larger, the switching line becomes "locally vertical" (when compared to the reference switching line corresponding to output quantization).* From left to right*: $\rho_I = 0.1$, $\rho_I = 0.5$, $\rho_I = 1$, $\rho_I = 2.5$. The last subfigure illustrates the crisis, when transient chaotic solution escapes by* jumping *over the stable manifold (indicated by blue arrow) of the neighbouring fixed point.*

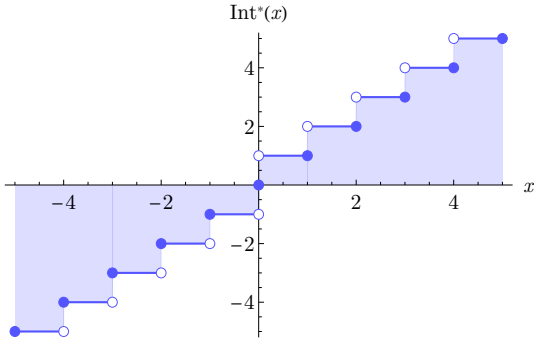

Figure 4.11: Conjugated integer-part function Int(), i.e., rounding towards infinity.*

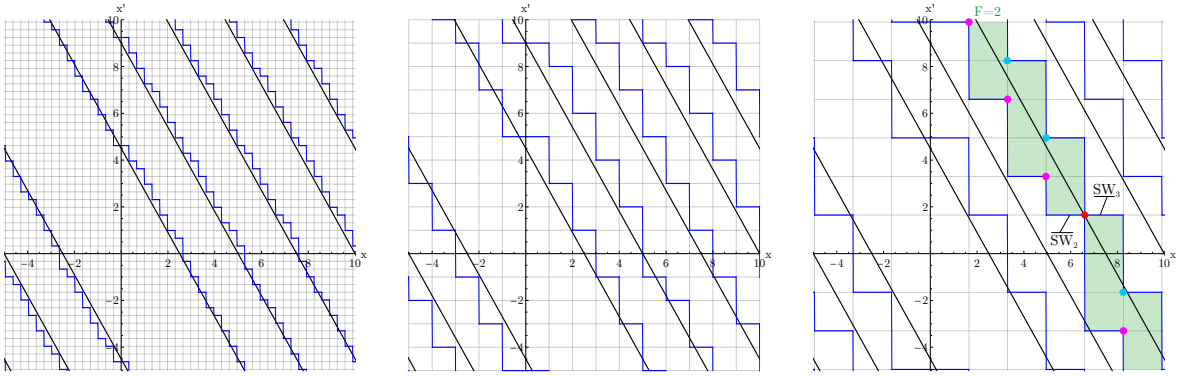

Figure 4.12: Switching lines at $\hat{P} = 2/5$, $\hat{D} = 2/9$ and $\rho_{\mathrm{I}} = 0.33$ (left) $\rho_{\mathrm{I}} = 1.0$ (centre), $\rho_{\mathrm{I}} = 1.65$ (right). The latter value is slightly above $\rho_{\mathrm{I}}^{L,i} = 1/(\hat{P} + \hat{D}) \approx 1.61$. Black lines indicate the switching lines for the output quantization case, gray gridlines indicate the ρ_{I}-spaced grid corresponding to the input quantization. Red point highlights switching line collision*, pink and blue points highlight* upper corners *of* SW_2 *and* lower corners *of* SW_3*, respectively. Green region indicates control effort band $F = 2$ which becomes disconnected due to* SLC*.*

One can similarly derive the inverse expression:

$$x = \rho_{\mathrm{I}} \operatorname{Int}^* \left(\frac{m - \hat{D}\, \rho_{\mathrm{I}} \operatorname{Int}\left(x'/\rho_{\mathrm{I}}\right)}{\hat{P}\, \rho_{\mathrm{I}}} \right), \quad m \in \mathbb{Z}. \tag{4.14}$$

As the quantization ratio increases further, the *stairs* on the switching lines become larger and at some point, the jagged switching lines will touch each other (see Fig. 4.12). This event – which will be referred to as *Switching Line Collision* (SLC) – changes the topology of control effort bands in the state space, regardless of the dynamics of the system under control as the switching lines depend only on the control strategy.

When *switching line collision* occurs, trajectories gain the ability to bypass certain control bands by passing through a switching line intersection point. In the case of PD-control – if there is no switching line collision – bands corresponding to the same control effort are connected domains. However, if the switching lines SW_{m} and $\mathrm{SW}_{\mathrm{m+1}}$ collide, the band $F_i = m$ becomes disconnected (see Fig. 4.12).

Observing the collision of SW_m and SW_{m+1} at $x = i\,\rho_{\mathrm{I}}$, $x' = j\,\rho_{\mathrm{I}}$, one can write the following condition:

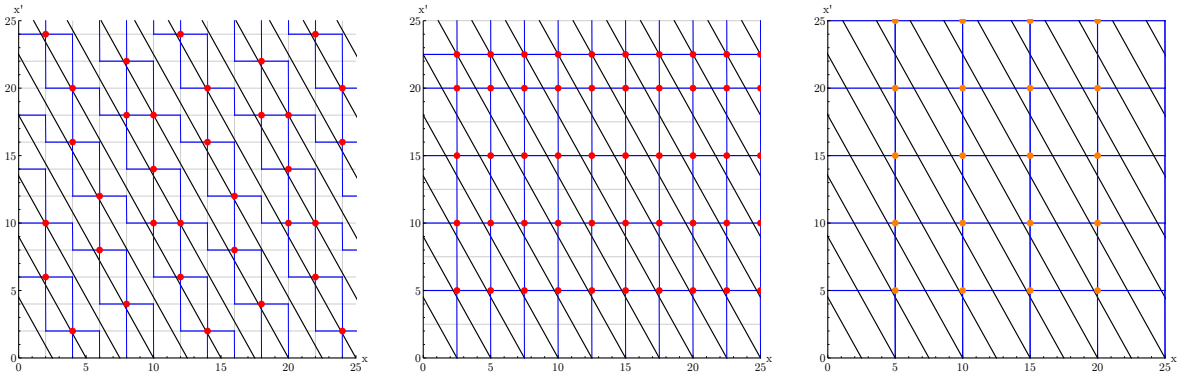

Figure 4.13: Switching lines at $\hat{P} = 2/5$, $\hat{D} = 2/9$ and critical quantization ratios $\rho_\mathrm{I} = 2.0$ (left), $\rho_\mathrm{I} = \rho_\mathrm{I}^{1,i} = 1/\hat{P}$ (centre), $\rho_\mathrm{I} = \rho_\mathrm{I}^{2,i} = 2/\hat{P}$ (right). Trajectories going through intersection points may bypass certain control effort bands. Orange points highlight 2^{nd} *order* switching line collisions.

$$\lim_{\varepsilon\to 0} \rho_\mathrm{I}\,\mathrm{Int}^*\left(\frac{m-\hat{P}\,\rho_\mathrm{I}\,\mathrm{Int}(i-\varepsilon)}{\hat{D}\,\rho_\mathrm{I}}\right) = \lim_{\varepsilon\to 0} \rho_\mathrm{I}\,\mathrm{Int}^*\left(\frac{(m+1)-\hat{P}\,\rho_\mathrm{I}\,\mathrm{Int}(i+\varepsilon)}{\hat{D}\,\rho_\mathrm{I}}\right).$$

Here the left and right hand sides correspond to switching lines SW_m and SW_{m+1}, respectively (see Eqs. (4.11-4.12)), both sides equal to $x' = j\,\rho_\mathrm{I}$ and $\{i, j, m\} \in \mathbb{Z}$.
Since the quantization $\mathrm{Int}(i)$ has a discontinuity (see Fig. 4.14), a small neighbourhood ε around $x = i\,\rho_\mathrm{I}$ is analyzed and the collision between the *upper* corner of the lower switching line (SW_m) and the *lower* corner of the upper switching line (SW_{m+1}) is formulated.
Expressing the limits, one can substitute $\lim_{\varepsilon\to 0}\mathrm{Int}(i-\varepsilon) = i-1$ for SW_m and use $\lim_{\varepsilon\to 0}\mathrm{Int}(i+\varepsilon) = i$ for SW_{m+1}, resulting in the following equation:

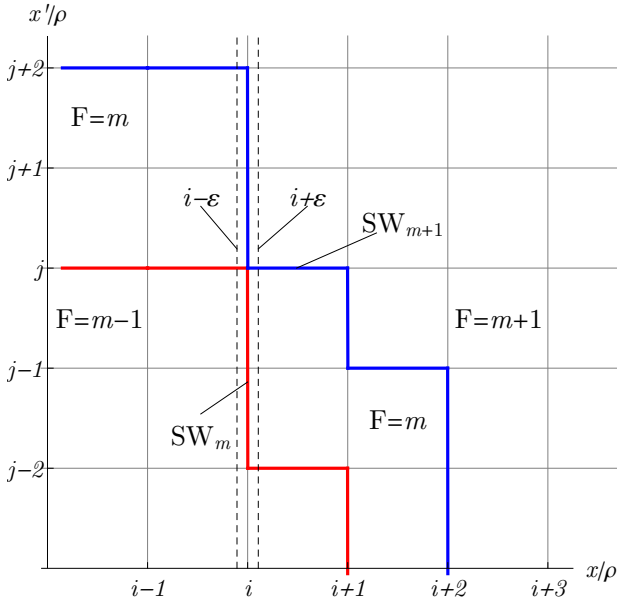

Figure 4.14: Illustration of switching line collision of SW_m (■) *and* SW_{m+1} (■) *at* $(i, j)\,\rho_\mathrm{I}$. *The upper corner of* SW_m *touches the lower corner of* SW_{m+1}.

$$\mathrm{Int}^*\left(\frac{m-\hat{P}\,\rho_\mathrm{I}\,(i-1)}{\hat{D}\,\rho_\mathrm{I}}\right)=j=\mathrm{Int}^*\left(\frac{(m+1)-\hat{P}\,\rho_\mathrm{I}\,i}{\hat{D}\,\rho_\mathrm{I}}\right),\quad \{i,j,m\}\in\mathbb{Z}. \tag{4.15}$$

Resolving the quantization to infinity (Int^*) in Eq. (4.15), the following inequalities can be written:

$$(j\ -\ 1)\ <\ \frac{m-\hat{P}\,\rho_\mathrm{I}\,(i-1)}{\hat{D}\,\rho_\mathrm{I}}\ <\ j,\ \ (j\ -\ 1)\ <\ \frac{(m+1)-\hat{P}\,\rho_\mathrm{I}\,i}{\hat{D}\,\rho_\mathrm{I}}\ <\ j. \tag{4.16}$$

The inequalities in Eq. (4.16) can be reformulated as

$$\frac{1}{\hat{D}+\hat{P}}<\rho_\mathrm{I}\le\frac{1}{\hat{P}}\quad\wedge\quad\frac{(m+1)-\hat{P}\,\rho_\mathrm{I}\,i}{\hat{D}\,\rho_\mathrm{I}}\le j<\frac{m-\hat{P}\,\rho_\mathrm{I}\,(i-1)+\hat{D}\,\rho_\mathrm{I}}{\hat{D}\,\rho_\mathrm{I}}, \tag{4.17}$$

$$\frac{1}{\hat{P}}<\overbrace{\rho_\mathrm{I}<\frac{1}{\hat{P}-\hat{D}}}^{\text{if }\hat{P}>\hat{D}>0}\quad\wedge\quad\frac{m-\hat{P}\,\rho_\mathrm{I}\,(i-1)}{\hat{D}\rho_\mathrm{I}}\le j<\frac{(m+1)-\hat{P}\,\rho_\mathrm{I}\,i+\hat{D}\,\rho_\mathrm{I}}{\hat{D}\rho_\mathrm{I}}. \tag{4.18}$$

For a given m and i, Eqs. (4.17-4.18) can be solved for $j\in\mathbb{Z}$ to find switching line collisions between SW_m and SW_{m+1} at $[x,x']=\rho_\mathrm{I}\,[i,j]$.
These kind of SLCs will be referred to as *first order switching line collisions* (while in general, the k^{th} order SLC means the collision of SW_m and SW_{m+k}).
It can be observed, that there is a *lowest quantization ratio* for first order switching line collisions to appear at a certain value of i in the state space:

$$\rho_\mathrm{I}^{L,i}=1/(\hat{P}+\hat{D}), \tag{4.19}$$

When $\rho_\mathrm{I}\ge\rho_\mathrm{I}^{L,i}$, first order SLCs are present in the state space and by increasing ρ_I, they become more and more frequent (see Fig. 4.13). Equation (4.17) reveals the value of the *critical quantization ratio* for which there is a solution for every i:

$$\rho_\mathrm{I}^{1,i}=1/\hat{P}. \tag{4.20}$$

When $\rho_\mathrm{I}=\rho_\mathrm{I}^{1,i}$, every switching line collides with its neighbour at coordinates $x=i\,\rho_\mathrm{I}$, for all i. To prove this statement, one can substitute $\rho_\mathrm{I}^{1,i}$ into Eq. (4.17), and the four inequalities are reduced to two relations:

$$(j-1)<\frac{m+1-i}{\hat{D}\,\rho_\mathrm{I}}<j. \tag{4.21}$$

This result shows that there is a solution $j\in\mathbb{Z}$ for every $\{i,m\}\in\mathbb{Z}$:

$$j=\mathrm{Int}^*\left(\frac{m+1-i}{\hat{D}\,\rho_\mathrm{I}}\right). \tag{4.22}$$

Note, that it does not imply that collision occurs for every $x'=j\,\rho_\mathrm{I}$, too (see Fig. 4.13 *centre panel*).

It follows from (4.18) that one can introduce the *highest quantization ratio* corresponding to the disappearance of first order switching line collisions:

$$\rho_\mathrm{I}^{H,i}=1/(\hat{P}-\hat{D})\quad\text{when}\quad 0<\hat{D}<\hat{P}. \tag{4.23}$$

When $\rho_\mathrm{I} > \rho_\mathrm{I}^{H,i}$, first order switching line collisions no longer present, because higher order collisions take their place.

Expressing the condition for the collision of SW_m and SW_{m+1} for i (instead of j, similarly to Eq. (4.15)), one can write:

$$\mathrm{Int}^*\left(\frac{m-\hat{D}\,\rho_\mathrm{I}\,(j-1)}{\hat{P}\,\rho_\mathrm{I}}\right) = i = \mathrm{Int}^*\left(\frac{(m+1)-\hat{D}\,\rho_\mathrm{I}\,j}{\hat{P}\,\rho_\mathrm{I}}\right), \quad \{i,j,m\}\in\mathbb{Z}, \tag{4.24}$$

which yields the following inequalities:

$$\frac{1}{\hat{P}+\hat{D}} < \rho_\mathrm{I} \le \frac{1}{\hat{D}} \quad \wedge \quad \frac{(m+1)-\hat{D}\,\rho_\mathrm{I}\,j}{\hat{P}\,\rho_\mathrm{I}} \le i < \frac{m-\hat{D}\,\rho_\mathrm{I}\,(j-1)+\hat{P}\,\rho_\mathrm{I}}{\hat{P}\,\rho_\mathrm{I}}, \tag{4.25}$$

$$\frac{1}{\hat{D}} < \overbrace{\rho_\mathrm{I} < \frac{1}{\hat{D}-\hat{P}}}^{\text{if } \hat{D}>\hat{P}>0} \quad \wedge \quad \frac{m-\hat{D}\,\rho_\mathrm{I}\,(j-1)}{\hat{P}\rho_\mathrm{I}} \le i < \frac{(m+1)-\hat{D}\,\rho_\mathrm{I}\,j+\hat{P}\,\rho_\mathrm{I}}{\hat{P}\rho_\mathrm{I}}. \tag{4.26}$$

Here another *critical quantization ratio* is revealed for which Eqs. (4.25-4.26) have a solution for every j (but not necessarily for every $x = i\,\rho_\mathrm{I}$):

$$\rho_\mathrm{I}^{1,j} = 1/\hat{D}. \tag{4.27}$$

Combining Eqs. (4.20) and (4.27), one can express a *combined critical quantization ratio*:

$$\rho_\mathrm{I}^{1} = \max(\rho_\mathrm{I}^{1,i}, \rho_\mathrm{I}^{1,j}) = \max(1/\hat{P}, 1/\hat{D}). \tag{4.28}$$

If $\rho_\mathrm{I} \ge \rho_\mathrm{I}^1$, switching line collisions occur for all i and j.
Expressing higher order switching line collisions in a similar fashion, one can arrive at the formulae of *k-th order critical quantization ratios* for the collision of SW_m and SW_{m+k} at $\forall\, i \in \mathbb{Z}$ and $\forall\, j \in \mathbb{Z}$, respectively:

$$\rho_\mathrm{I}^{k,i} = k/\hat{P}, \tag{4.29}$$

$$\rho_\mathrm{I}^{k,j} = k/\hat{D}. \tag{4.30}$$

It is important to note, that due to the double deadzone of the mid-tread quantizer (see Fig. 4.2), switching line collisions of SW_{-1} and SW_{+1} are 2^{nd} order ones.
Here only the case of positive $\hat{P}$ and $\hat{D}$ is considered, but a similar analysis can be carried out for negative control parameters, as well.
In the following sections, it is shown, how the transition between the twofold and single quantization cases affects the switching lines.

4.3.2 Transition from twofold quantization to output quantization

It is clear – based on Section 4.3, and Eq. (4.13) – that refining the input quantizer ($\rho_\mathrm{I} \to 0$) means smaller steps on the jagged switching lines, and eventually the transition to *output quantization* leads to a set of parallel lines.

$$\rho_\mathrm{I}\,\mathrm{Int}^*\left(\frac{m-\hat{P}\,\rho_\mathrm{I}\,\mathrm{Int}\,(x/\rho_\mathrm{I})}{\hat{D}\,\rho_\mathrm{I}}\right) \xrightarrow[\rho_\mathrm{I}\to 0]{} \frac{m-\hat{P}\,x}{\hat{D}} \quad m\in\mathbb{Z}. \tag{4.31}$$

One can imagine this kind of transition by looking at Fig. 4.12. The transition from twofold quantization to *input quantization*, however, is not this trivial.

4.3.3 Transition from twofold quantization to input quantization

Switching lines corresponding to input quantizations form a regular grid of horizontal ($\mathrm{Int}(y)$) and vertical ($\mathrm{Int}(x)$) lines (see Fig. 4.6 *right*). The square shaped domains (or rectangle shaped domains around the axes) between switching lines correspond to integer value linear combination of the control parameters, e.g., $F = i\,\hat{P} + j\,\hat{D}$ control effort at $\mathrm{Int}(x) = i$, $\mathrm{Int}(x') = j$.

If one would like to achieve the same structure of switching lines in the twofold quantization case, the following conditions must be satisfied:

– *Condition 1*: switching lines must partition the state space into square shaped domains, i.e., for every x' value, crossing $x = i$, ($i \in \mathbb{Z}$) values must result in a switch in the control effort value. Similarly, for every x value, crossing $x' = j$, ($j \in \mathbb{Z}$) must also result in a switch.
– *Condition 2*: for each domain between the switching lines, the control effort value should be the same as in the case of input quantization.

Condition 1 can be satisfied by using $\rho_{\mathrm{O}} \leq \rho_{\mathrm{O}}^{1}$ (where $\rho_{\mathrm{O}}^{1} = 1/\rho_{\mathrm{I}}^{1} = \min(\hat{P}, \hat{D})$), which corresponds to $\rho_{\mathrm{I}} \geq \max(1/\hat{P}, 1/\hat{D})$ (see Eq. (4.28)), because in this case, for all $i, j \in \mathbb{Z}$ – at least first order – switching line collision takes place.
It can be seen, that once *Condition 1* is satisfied (and the structure of the state space matches the input quantization case), the control effort value of twofold quantization will be within an error of ρ_{O} to the control effort value of the input quantization case (see Eq. (4.9)). It follows therefore, that $\rho_{\mathrm{O}} \to 0$ will satisfy *Condition 2*.

4.4 Main results

I have analysed the effect of twofold quantization in digital control, i.e., when both the input and the output of the controller are quantized. I have formulated the corresponding micro-chaos map, and determined how the single quantization cases can be derived from the twofold quantization formalism. I pointed out that the transition between these cases is not trivial.
I have found two new bifurcation phenomena that can occur in the case of twofold quantization only. One of them is the *deadzone crisis* when the variation of the quantization parameter changes the interaction of the input and output deadzones, leading to a crisis event, that turns the attractor to a chaotic repellor exhibiting transient chaos.
Another phenomenon is the *switching line collision*, when neighbouring switching lines touch each other, significantly changing the state-space topology.

Main Result 4: Quantization Ratio

Twofold quantization – when both the input and the output of the controller are quantized – can be characterised by the so-called *quantization ratio* parameter, corresponding to the ratio of input and output quantizers' resolution. Twofold quantization can be reduced to a single quantization case (input-only or output-only quantization) if an appropriate quantization ratio ρ is used and its limit $\rho \to 0$ is analysed.
It is impossible to analyse both kinds of twofold-to-single quantization transitions with a single quantization ratio, because parameter ρ appears in an integer-part function in the governing equations of the dynamical system. Consequently, the upper limit corresponding to one of the transitions is zero: $\lim_{\rho\to\infty} \rho \operatorname{Int}(x/\rho) = 0$, therefore, the control effort is turned off for finite values of x, where x is a linear combination of state variables.
Hence, two different quantization ratios are necessary to be used for the two transitions, and they are inversely proportional to each other: $\rho' \sim 1/\rho$.

Related publications: [29, 28].

Main Result 5: Switching Line Collision and Deadzone Crisis

In the case of twofold quantization – when both the input and the output of the controller are quantized – the state space of the controlled system can be divided into domains, each corresponding to a certain value of the control effort, separated by switching lines. Two new bifurcation phenomena were introduced that can occur only in the case of twofold quantization:
- *Switching Line Collision* is the event, when piecewise smooth switching lines touch each other, that is, collide in the state space. This phenomenon can induce qualitative changes in the state space of continuous *flows*, but – since the trajectories of *maps* are allowed to "jump" in the phase-space – the effects of Switching Line Collision are less pronounced in the case of maps.
The condition of the existence of first order switching line collisions is provided for maps where the neighbouring switching lines are originating from twofold quantization and proportional-derivative (PD) control scheme. Conditions for the collision between any switching line and its k-th neighbour were determined as well, along with critical quantization ratios which correspond to special cases, when all switching lines collide at all possible locations.
- *Deadzone Crisis* is an event, when a chaotic attractor turns to a transient chaotic repellor due to the change of the corresponding switching line's shape. The term *deadzone crisis* is originated from the observation, that this event is strongly related to the variation

of input-deadzones in case of the 2D micro-chaos map. It was shown that this crisis event can strongly influence the maximal possible control error in the system. In some cases, even the increase of a resolution parameter r_{I} or r_{O} can lead to smaller control error.

Related publications: [29, 28].

From practical point of view, it is possible to improve the properties of the control for a given application, by carrying out an analysis of the quantization ratio and selecting a favourable range as illustrated in Section 4.2.2. Doing so, one can also find out how to improve a certain controlled system, i.e., which quantizer should be replaced by a higher-resolution one. In some cases one can even arrive to an unnatural conclusion, that using lower-resolution output quantizer or larger sampling time will actually result in lower control error. Similar results were found in [45, 49], where the quantization improved the stability properties of the controlled system.

5

Hybrid-switching micro-chaos map

5.1 Introduction

In the previous chapters, various digitally controlled systems exhibiting micro-chaos were analysed. It was shown that in case of quantization at the control effort (output of the controller), separated chaotic attractors are present in the state-space, see Section 2.3. However, if the measured states (input of the controller) are quantized, usually a periodic orbit appears with superimposed chaotic oscillation [7]. The transition between these two cases was also discussed in Chapter 4.

Thus, although several digital control schemes were analysed, one important point have not been addressed yet: since the amplitude of micro-chaotic oscillations is typically small, the inevitable friction that is present in mechanical systems may have a large influence on the dynamics. Thus, the question naturally arises: can micro-chaos persist if Coulomb friction is present?

This chapter introduces the *hybrid-switching micro-chaos map*, where the term *hybrid* refers to the two types of switching in the system: the *"map-like"* switching of the control effort that happens only at sampling time instants and the *"flow-like"*, continuous switching of the friction force at the sign changes of the velocity. Simple analytical formulas are presented to determine if chaotic attractors are affected by the sticking introduced by the friction or not. Finally, numerical results obtained using Clustered Simple Cell Mapping (C-SCM) [24] are given to support the theoretical results.

Lastly, the chapter concludes, that the phenomena of micro-chaos can withstand the presence of Coulomb-friction and chaotic attractors can coexist with sticking zones in the state space.

5.2 PD-controlled inverted pendulum with dry friction

Consider an inverted pendulum controlled according to a proportional-derivative (PD) scheme with sampling and zero order hold, as shown in Figure 5.1. Dry friction, symbolised by μ in the figure, is temporarily omitted.

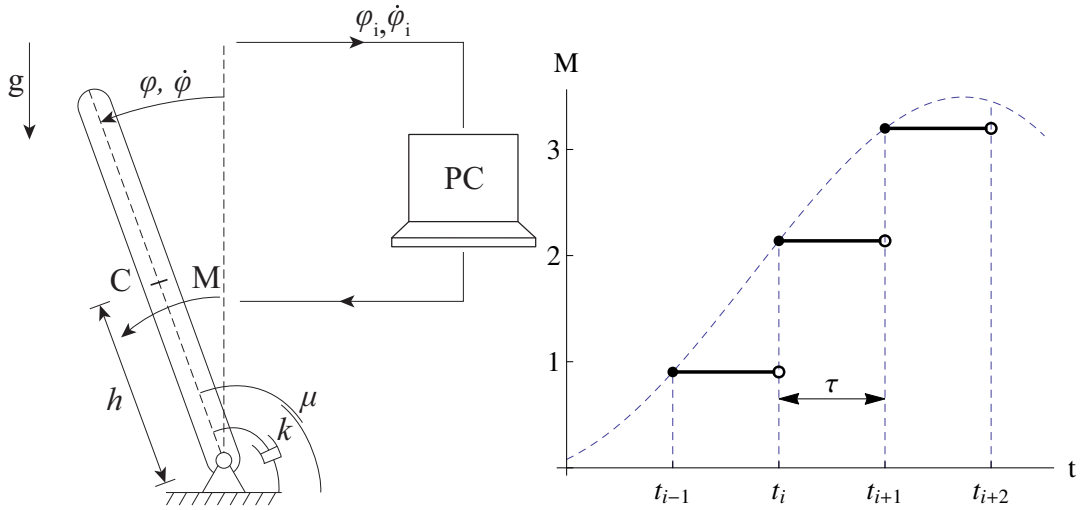

Figure 5.1: Digitally controlled inverted pendulum realising zero-order-hold and the control torque M with respect to time. Blue dashed envelope curve indicates a reference control torque corresponding to a continuous, non-sampled case.

The equation of motion of the frictionless system can be given as

$$J\,\ddot{\varphi}(t) = mgh\sin(\varphi(t)) - k\,\dot{\varphi}(t) - p\,\varphi_i - d\,\dot{\varphi}_i, \qquad t \in [i\tau, (i+1)\tau), \tag{5.1}$$

where m and J are the mass and mass moment of inertia of the pendulum, respectively. h is the distance between the centre of mass and the axis of rotation, p and d are control gains and k is the linear damping coefficient. Gravitational acceleration is denoted by g, τ is the sampling time, while $\varphi_i = \varphi(i\tau)$ and $\dot{\varphi}_i = \dot{\varphi}(i\tau)$ are the sampled values of the angular position and angular velocity, respectively, at the beginning of the i^{th} time interval. Rearranging and linearizing (5.1) yields

$$\ddot{\varphi}(t) + 2\alpha\delta\dot{\varphi}(t) - \alpha^2\varphi(t) = -P\,\varphi_i - D\,\dot{\varphi}_i, \tag{5.2}$$

where

$$\alpha^2 = \frac{mgh}{J}, \quad 2\alpha\delta = \frac{k}{J}, \quad P = \frac{p}{J}, \quad D = \frac{d}{J}. \tag{5.3}$$

As it is shown in [7], if the control torque can assume only quantized values, this system exhibits small amplitude chaotic vibrations. However, as it was pointed out in [4], Coulomb friction has a major role in the damping of such systems. Therefore, our present goal is to analyse the effect of dry friction on the previously found, so-called micro-chaotic solutions. Before formulating the equations for the quantized case, we add a new term to (5.2) that corresponds to Coulomb friction (see Fig. 5.2):

$$\ddot{\varphi}(t) + 2\alpha\delta\dot{\varphi}(t) - \alpha^2\varphi(t) = -P\,\varphi_i - D\,\dot{\varphi}_i - \operatorname{sgn}(\dot{\varphi}(t))\,\mu_0. \tag{5.4}$$

Note, that this equation is non-linear due to the sgn function that may assume any value between -1 and 1 at zero angular velocity. The actual value of the friction force at $\dot{\varphi}(t) = 0$ is determined by the other forces and torques acting on the pendulum. As a consequence, the upper equilibrium point turns to an interval of possible equilibrium positions. Thus, (5.4) cannot be linearized at the $\varphi = 0$, $\dot{\varphi} = 0$ state in the conventional manner. To linearize the equation in a mathematically correct way, one could apply the theory of differential inclusions [17] or introduce a regularized, smooth approximation to the sgn function. This latter approach was followed in [4].

However, as it will be shown in this section, quantization is another non-smooth effect that introduces non-linearity in the system. Thus, instead of focusing on the linearization process, we opted for using non-smooth models describing the effects of friction and quantization. It is usual in textbooks and papers dealing with dry friction (see e.g., [44] and [48]) that a friction force-related term $F_{friction} = -\mathrm{sgn}(v)\, F_N$ is added to otherwise linear(ized) equations, and the resulting piecewise linear system is analysed. Even in case of time-delayed systems, piecewise smooth control input is considered similarly, [36, 37]. Since this method led to qualitatively correct findings, it is often applied in the industry, too [41]. Following this approach, we continue the analysis of (5.4) without further linearization.

Eq. (5.2) can be rewritten as a system of first order differential equations that is valid for $t \in [i\tau, (i+1)\tau)$, i.e., in a sampling interval:

$$\begin{aligned} \dot{\omega}(t) &= \alpha^2\varphi(t) - 2\alpha\delta\dot{\varphi}(t) - P\varphi_i - D\omega_i - \mathrm{sgn}(\dot{\varphi}(t))\,\mu_0, \\ \dot{\varphi}(t) &= \omega(t), \end{aligned} \tag{5.5}$$

with initial conditions $\omega(i\tau) = \omega_i$ and $\varphi(i\tau) = \varphi_i$.

If the sign of the angular velocity does not change, Eq. (5.5) can be easily solved for a sampling interval. Introducing the notations $\hat{\alpha} = \alpha\tau$, $\Gamma = \sqrt{1+\delta^2}$, $\hat{P} = P\tau^2$, $\hat{D} = D\tau$, $x = \varphi/(r_{\mathrm{out}}\tau^2)$, $v = \omega/(r_{\mathrm{out}}\tau)$, $\hat{\mu} = \mu_0\,\tau^2/(r_{\mathrm{out}}\tau^2)$, dimensionless time $T = t/\tau$ and r_{out} as the resolution of the actuated control effort, the solution formulates a dimensionless 2D map:

$$\mathbf{y}(T) \equiv \begin{bmatrix} x(T) & v(T) \end{bmatrix}^T = \mathbf{U}(T)\,\mathbf{y}(0) + \mathbf{b}(T)\,F(\mathbf{y}(0)), \quad T \in [0,1), \tag{5.6}$$

where F is composed of the control effort and the friction force

$$F(\mathbf{y}(T)) = \hat{P}\,x(0) + \hat{D}\,v(0) + \mathrm{sgn}(v(T))\,\hat{\mu}, \tag{5.7}$$

and the solution operators of the ODE are

$$\mathbf{U}(T) = \frac{e^{-\hat{\alpha}\delta T}}{\Gamma} \begin{bmatrix} \Gamma\,\mathrm{ch}\,(\hat{\alpha}\Gamma T) + \delta\,\mathrm{sh}\,(\hat{\alpha}\Gamma T) & \mathrm{sh}\,(\hat{\alpha}\Gamma T)/\hat{\alpha} \\ \hat{\alpha}\,\mathrm{sh}\,(\hat{\alpha}\Gamma T) & \Gamma\,\mathrm{ch}\,(\hat{\alpha}\Gamma T) - \delta\,\mathrm{sh}\,(\hat{\alpha}\Gamma T) \end{bmatrix}$$

and

$$\mathbf{b}(T) = \frac{1}{\hat{\alpha}^2\Gamma} \begin{bmatrix} \Gamma - e^{-\hat{\alpha}\delta T}\,(\Gamma\,\mathrm{ch}\,(\hat{\alpha}\Gamma T) + \delta\,\mathrm{sh}\,(\hat{\alpha}\Gamma T)) \\ -\hat{\alpha}e^{-\hat{\alpha}\delta T}\,\mathrm{sh}\,(\hat{\alpha}\Gamma T) \end{bmatrix},$$

according to Section 2.1.1.

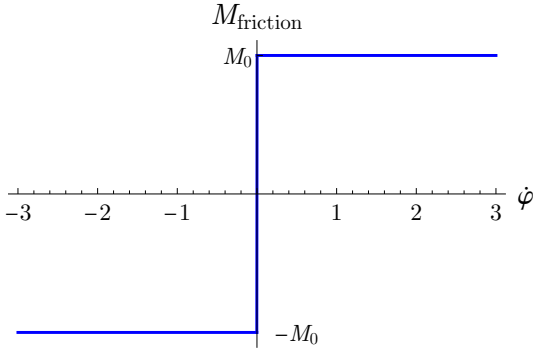

Figure 5.2: Bearing friction with respect to angular velocity of the pendulum. The coefficients of kinetic and static friction are considered to be equal.

5.3 The hybrid-switching micro-chaos map

The calculated control force does not change within the sampling interval, due to the zero order hold. Consequently, Eq. (5.6) can be used as a map between states at the i^{th} and $(i+1)^{\text{st}}$ sampling instants, if the sign of the velocity v does not change either in the interval $T \in [i, i+1)$:

$$\mathbf{y}(i+T) = \mathbf{U}(T)\,\mathbf{y}(i) + \mathbf{b}(T)\,F(\mathbf{y}(i)), \quad T \in [0,1). \tag{5.8}$$

Introducing the notation $\mathbf{y}_i = \begin{bmatrix} x(i) & v(i) \end{bmatrix}^T$, the state vector at the next sampling instant can be expressed by substituting $T = 1$ in Eq. (5.8). Thus, the following map is obtained:

$$\mathbf{y}_{i+1} = \mathbf{U}\,\mathbf{y}_i + \mathbf{b}\left(\underbrace{\mathrm{Int}(\hat{P}\,x_i + \hat{D}\,v_i)}_{m_i} + \underbrace{\mathrm{sgn}(v_i)\,\hat{\mu}}_{\mu_i}\right). \tag{5.9}$$

Here m_i is the control effort, μ_i is the friction force and $\mathrm{Int}(\cdot)$ denotes the integer part function representing the quantization of the control effort. The zero-order-hold introduces a *map-like switching* in the system: the controller updates the control effort at sampling instants, only.

In the frictionless case (at $\hat{\mu} = 0$) or if the sign of the velocity does not change within a sampling interval, there is no other discontinuity in the system. Consequently, (5.8) – that is another generalization of the *micro-chaos map* – fully describes the evolution of the solutions in these cases.

The signum function corresponding to the friction, however, corresponds to a *flow-like switching*, because the sign of the friction force changes at any time instant when the velocity changes sign – regardless of the sampling. Thus, (5.8) must be modified to take into account this type of switching, as well.

To handle the case when the velocity changes sign within the i^{th} sampling interval, one needs to calculate the dimensionless time $T_{0,i}$ when the solution reaches the switching line of the friction force

$$\Sigma_f : \mathbf{y}\,|_{v=0}, \tag{5.10}$$

i.e., when the velocity is zero. Expressing the velocity using Eq. (5.8), one arrives at

$$\underbrace{\hat{\alpha}\,\Gamma\,v_i}_{:=C_i}\cosh(\hat{\alpha}\,\Gamma\,T_{0,i}) \underbrace{-\left(\hat{\alpha}\,\delta\,v_i - \hat{\alpha}^2\,x_i + m_i + \mu_i\right)}_{:=S_i}\sinh(\hat{\alpha}\,\Gamma\,T_{0,i}) = 0. \tag{5.11}$$

From Eq. (5.11), the dimensionless time corresponding to zero velocity can be obtained:

$$T_{0,i} = \frac{1}{\hat{\alpha}\,\Gamma}\log\left(\sqrt{\frac{S_i - C_i}{S_i + C_i}}\right), \tag{5.12}$$

where S_i and C_i are the coefficients of $\sinh(\hat{\alpha}\,\Gamma\,T_{0,i})$ and $\cosh(\hat{\alpha}\,\Gamma\,T_{0,i})$, respectively in Eq. (5.11). Both S_i and C_i depend on the state of the system (i.e., x_i, v_i or μ_i) at the beginning of the sampling interval. Thus, the state vector $\tilde{\mathbf{y}}_i$ must be supplemented with the friction state μ_i: $\tilde{\mathbf{y}}_i = \begin{bmatrix} x_i & v_i & \mu_i \end{bmatrix}^T$. The condition of crossing the switching line of the friction force (Σ_f) within the actual sampling interval is

$$0 \le T_{0,i} < 1. \tag{5.13}$$

If $T_{0,i} > 1$, one can use (5.8). Otherwise, the mapping between successive sampling instants must be divided into three steps: 1) time evolution until the velocity becomes zero, 2) change of the sign of friction force (or sticking), and 3) time evolution until the next sampling interval.

Combining these steps, one can formulate the so-called *hybrid-switching micro-chaos map*:

$$\begin{aligned}\tilde{\mathbf{y}}(T_{0,i}) &= \tilde{\mathbf{U}}(T_{0,i})\,\tilde{\mathbf{y}}_i + \tilde{\mathbf{b}}(T_{0,i})\,F(\tilde{\mathbf{y}}_i),\\ \tilde{\mathbf{y}}(T_{0,i})^+ &= \tilde{\mathbf{Q}}\,\tilde{\mathbf{y}}(T_{0,i})\\ \tilde{\mathbf{y}}_{i+1} &= \tilde{\mathbf{U}}(1-T_{0,i})\,\tilde{\mathbf{y}}(T_{0,i})^+ + \tilde{\mathbf{b}}(1-T_{0,i})\,F(\tilde{\mathbf{y}}(T_{0,i})^+),\end{aligned} \tag{5.14}$$

where

$$\tilde{\mathbf{U}}(T) = \left[\begin{array}{cc|c} & & 0\\ & \mathbf{U}(T) & 0\\ \hline 0 & 0 & 1\end{array}\right] \quad \text{and} \quad \tilde{\mathbf{b}}(T) = \left[\begin{array}{c}\mathbf{b}(T)\\ 0\end{array}\right]. \tag{5.15}$$

The discontinuity map related to the change of sign of the friction force is

$$\tilde{\mathbf{Q}} = \begin{cases} \begin{bmatrix} 1 & 0 & 0\\ 0 & 0 & 0\\ 0 & 0 & 0\end{bmatrix} & \text{if sticking occurs,}\\ \begin{bmatrix} 1 & 0 & 0\\ 0 & 1 & 0\\ 0 & 0 & -1\end{bmatrix} & \text{otherwise,}\end{cases} \tag{5.16}$$

where the condition of sticking is:

$$\text{abs}\left(\text{Int}(\hat{P}\,x(i) + \hat{D}\,v(i)) - \hat{\alpha}^2\,x(i+T_{0,i})\right) < \hat{\mu}. \tag{5.17}$$

In the first case of Eq. (5.16), when (5.17) is satisfied, the solution sticks and will stay at Σ_f. Otherwise, the solution crosses the switching line and the sign of the friction force is changed. $\tilde{\mathbf{y}}(T_{0,i})$ is the state when the solution reaches Σ_f and $\tilde{\mathbf{y}}(T_{0,i})^+$ is the state immediately after crossing Σ_f.
It should be noted, that the initial state of map (5.14) must contain a friction force $\mu_0 = \text{sgn}(v_0)\,\hat{\mu}$, compatible with the initial velocity.

5.4 Topological patterns, sticking zones

Recall from Section 2.3.1, that the equation of control effort switching lines is

$$\text{Int}(\hat{P}\,x + \hat{D}\,v) = m \quad \Rightarrow \quad v = \frac{m - \hat{P}\,x}{\hat{D}}, \quad m \in \mathbb{Z}\backslash\{0\}. \tag{5.18}$$

The unstable fixed points $\mathbf{F}_m = [x_u^m \quad 0]^T$ of the micro-chaos map lie on the x-axis, at zero velocity. Omitting the friction force, the positions of the fixed points can be determined:

$$\text{Int}(\hat{P}\,x_u^m) = \hat{\alpha}^2\,x_u^m \quad \Rightarrow \quad x_u^m = \frac{m}{\hat{\alpha}^2}, \qquad m \in \mathbb{Z}. \tag{5.19}$$

This formula is valid only if x_u^m resides between the m^{th} and $(m+1)^{\text{st}}$ switching lines – since this is required to have $\text{Int}(\hat{P}\,x_u^m) = m$. Based on Eqs. (5.18)-(5.19), unstable fixed points and switching lines occur alternately on the $x - v$ phase-space (see Fig. 5.3).

If unstable fixed points exist on both sides of a switching line, they push the trajectories towards each other. Therefore, chaotic attractors are expected to be at the intersections of the switching lines and the x axis (see Fig. 5.3):

$$x_{\text{attr}} = \frac{m}{\hat{P}}, \qquad m \in \mathbb{Z}\backslash\{0\}. \tag{5.20}$$

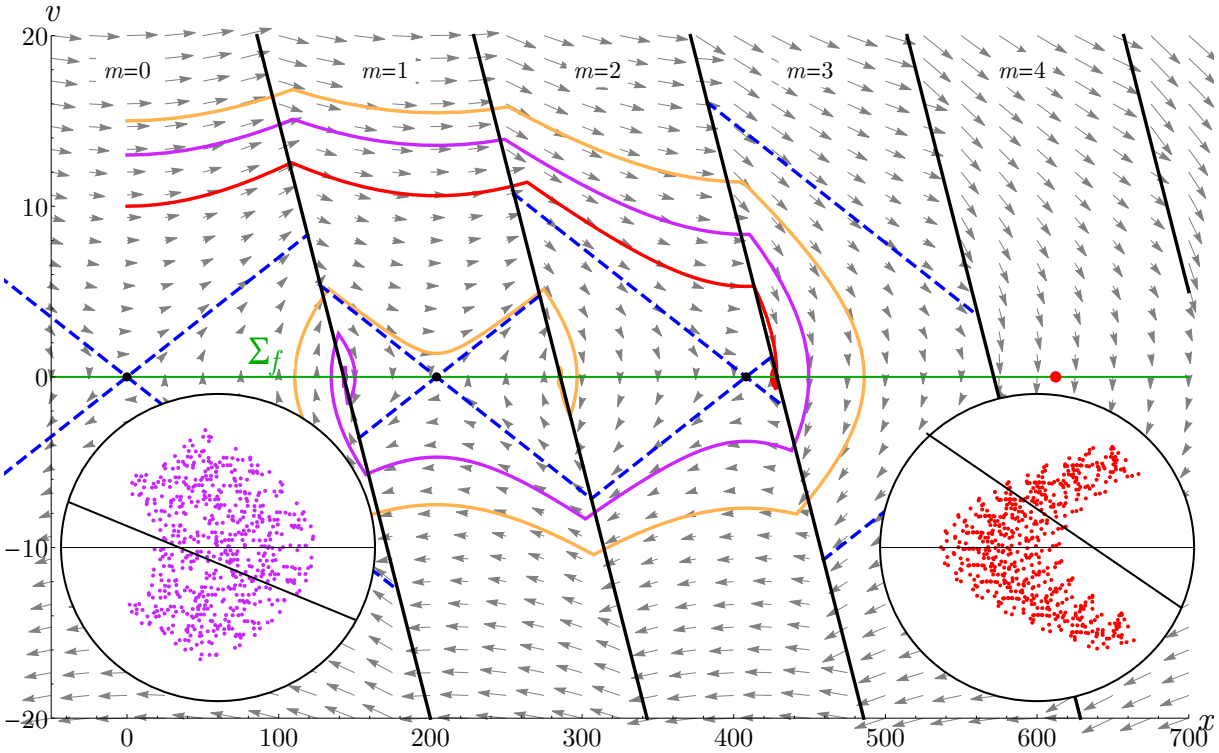

Figure 5.3: The state space of the micro-chaos map, when $\hat{\mu} = 0$. Black lines are control effort switching lines, Σ_f is denoted with a green line, unstable fixed points are denoted with black dots and their manifolds are the blue dashed lines. Three example trajectories corresponding different initial velocities are shown, ending in different chaotic attractors. Here $m_{\max} = 3$ and after the 3rd attractor at approx. $x = 420$, the alternating pattern of attractors and fixed points breaks. The upcoming, virtual fixed point is shown with a red dot.

Restricting the control parameters to the stable domain ($\hat{P} > \hat{\alpha}^2$), the index of the outermost attractor can be expressed – in a slighly different way as in Section 2.3:

$$\frac{m-1}{\hat{\alpha}^2} = \frac{m}{\hat{P}} \quad \Rightarrow \quad m_{\max} = \mathrm{Int}\left(\frac{\hat{P}}{\hat{P}-\hat{\alpha}^2}\right). \tag{5.21}$$

At $m > m_{\max}$, the alternating pattern of attractors and fixed points breaks because the $m = m_{\max}$ control effort band does not have a fixed point inside. This particular fixed point is virtual and is situated in the next control effort band, see Fig. 5.3. While there can exist an attractor between a real and a virtual fixed point [7], there cannot be attractors at switching lines if $m > m_{\max}$. Thus, one can expect to have several attractors when the difference between the control gain $\hat{P}$ and $\hat{\alpha}^2$ is relatively small. At certain parameter combinations (see [6]), the neighbouring attractors merge and form a larger attractor.

An upper estimate for the control error – the distance of the outermost attractor from the origin – can be given for that frictionless case, when the eigenvalues of $\mathbf{U}$ are positive and real [6]:

$$x_{\mathrm{err,max}} = \frac{1}{\hat{P}-\hat{\alpha}^2}. \tag{5.22}$$

As friction is introduced in the system, the fixed points extend to larger intervals along the x axis, where the friction force can be in equilibrium with the other forces acting on the

system. If such an equilibrium interval collides with an attractor, a crisis phenomenon occurs and the attractor turns to a repellor, exhibiting finite time transient chaotic behaviour.

As it was shown in [6], there is only one fixed point in the phase-space – at the origin – if large control gain $\hat{P} > 2\hat{\alpha}^2$ is chosen from the domain of stability. The corresponding large attractor immediately disappears if friction is present.

However, at relatively small values of $\hat{P}$ – when it is only slightly larger than $\hat{\alpha}^2$ –, several small attractors coexist and some of them may be quite far from the neighbouring fixed points. Thus, such attractors can persist even if friction is taken into account.

Considering the condition of sticking (5.17) and substituting the control effort value m, one arrives at

$$\mathrm{abs}(m - \hat{\alpha}^2\, x) < \hat{\mu}.$$

Resolving the absolute value yields

$$\frac{(m-\hat{\mu})}{\hat{\alpha}^2} < x_{\mathrm{sticking}} < \frac{(m+\hat{\mu})}{\hat{\alpha}^2}. \tag{5.23}$$

One can recognize here the term corresponding to the unstable fixed points (Eq. (5.19)), that is, the m-th sticking zone will appear around the m-th unstable fixed point:

$$x_{\mathrm{sticking},m} \in \left[x_{u,m} - \frac{\hat{\mu}}{\hat{\alpha}^2}, x_{u,m} + \frac{\hat{\mu}}{\hat{\alpha}^2} \right]. \tag{5.24}$$

Using Eq. (5.20) and Eq. (5.24), one can express the condition corresponding to the overlap of the attractor centered around $x = m/\hat{P}$ and one of its neighbouring sticking zones:

$$\frac{m-1+\hat{\mu}}{\hat{\alpha}^2} = \frac{m}{\hat{P}} \quad \text{or} \quad \frac{m}{\hat{P}} = \frac{m-\hat{\mu}}{\hat{\alpha}^2}. \tag{5.25}$$

Note, that the size of the attractor is not taken into account by these formulae. The collision of the attractor and the sticking zone (the crisis) takes place at a smaller value of the friction parameter. However, the parameters corresponding to the crisis phenomenon can be estimated fairly well by (5.25) if the attractor is significantly smaller than $1/\hat{P}$.

One can also express the critical friction parameter when all sticking zones merge with their neighbours, that is the whole x-axis behaves as a sticking zone:

$$\frac{\hat{\mu}_{\mathrm{crit}}}{\hat{\alpha}^2} = \frac{1}{\hat{\alpha}^2} \rightarrow \hat{\mu}_{\mathrm{crit}} = 1. \tag{5.26}$$

Since the collision of chaotic attractors and sticking zones also depends on the size of the attractors, providing an exact formula for the absorbtion of a certain chaotic attractor can be challenging. Therefore, cell mapping, especially, the Clustered Simple Cell Mapping (C-SCM) method (see Chapter 3 and [24]) was used to examine the effect of increasing the friction parameter $\hat{\mu}$.

5.5 Cell mapping results

As it was discussed in Chapter 3, cell mapping methods are suitable for the global investigation of the long term behaviour of nonlinear dynamical systems [35]. Using cell mapping methods fixed points, periodic orbits and their basin of attraction can be quickly found. Chaotic attractors are usually covered with one or more high-period orbits. The Clustered Simple Cell Mapping (C-SCM) was applied to Eq. (5.14) in order to determine whether the chaotic attractors disappear due to the dry friction or not.

Consider Figure 5.4, showing chaotic attractors (black dots), their basin of attraction (coloured bands), switching lines (white), and manifolds of fixed points (dashed white lines).

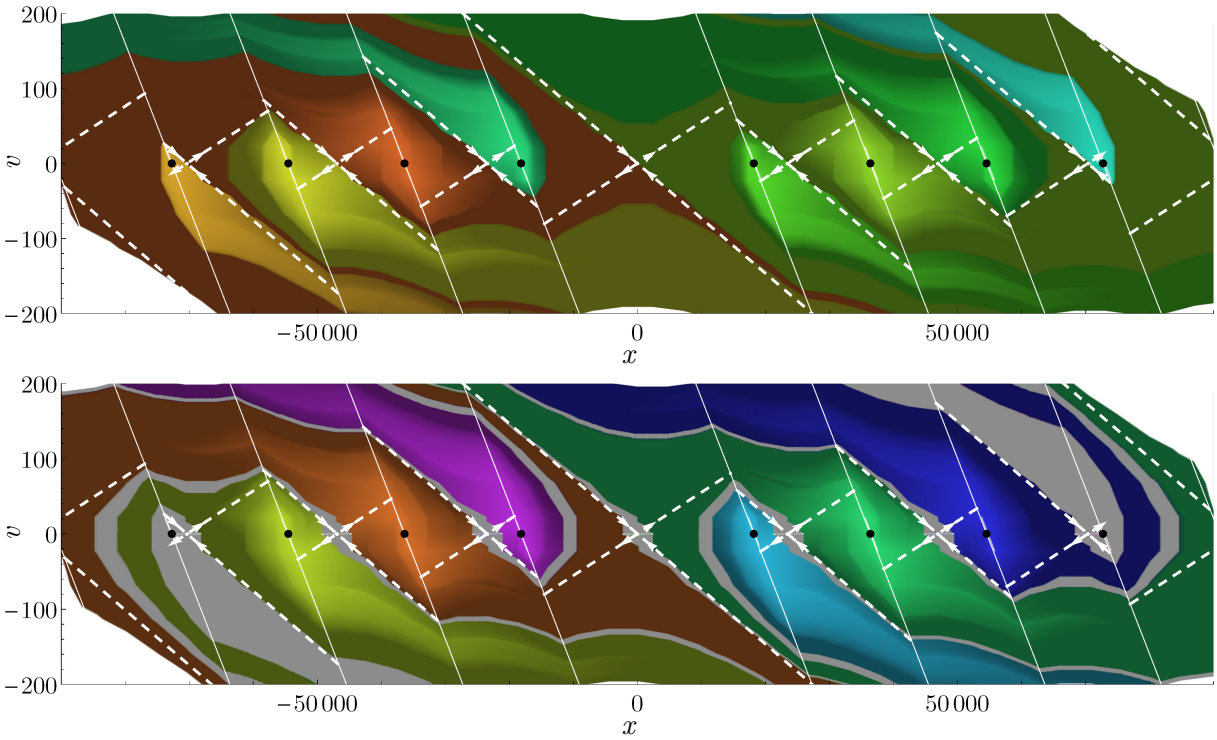

Figure 5.4: C-SCM results for $\hat{\alpha} = 6.53 \times 10^{-3}$, $\hat{\delta} = 0$, $\hat{P} = 5.5 \times 10^{-5}$, $\hat{D} = 2.5 \times 10^{-3}$. Top*:* $\hat{\mu} = 0$. Bottom*:* $\hat{\mu} = 0.095$. *Chaotic attractors are indicated with black dots, their basin of attractions are coloured regions, fixed points' manifolds are shown as white dashed lines. Gray regions indicate the basins of attraction of sticking zones, the bottom subfigure shows the case, when the outermost chaotic attractors are absorbed by sticking zones.*

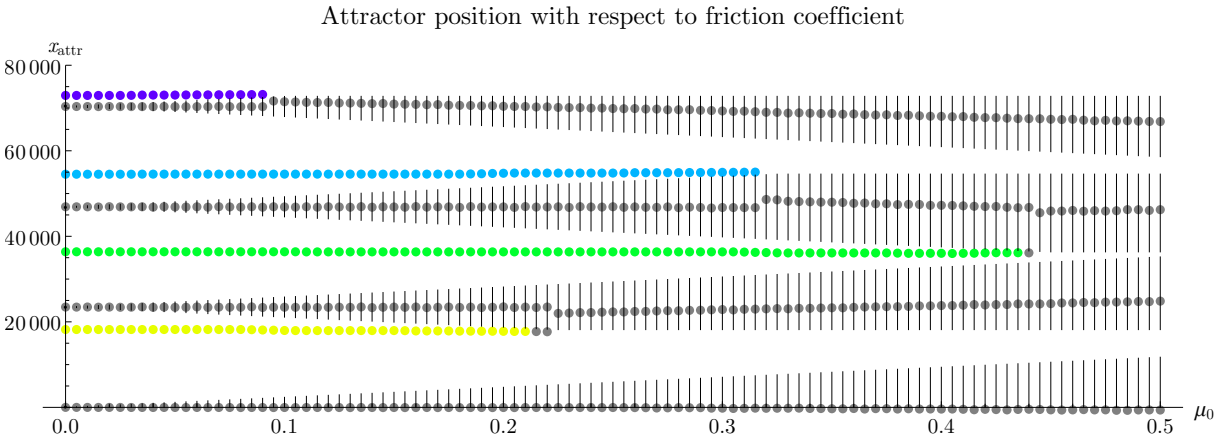

Figure 5.5: C-SCM parameter scan results for $\hat{\alpha} = 5.5 \times 10^{-5}$, $\hat{\delta} = 0$, $\hat{P} = 5.5 \times 10^{-5}$, $\hat{D} = 2.5 \times 10^{-3}$. Coloured points correspond to the location coordinate of chaotic attractors, while gray points indicate the centers of periodic cell groups corresponding to sticking zones. The theoretical ranges of sticking zones are shown by vertical sections. As the friction parameter is increasing, chaotic attractors are absorbed by sticking zones, one by one.

Results with $\hat{\mu} = 0$ and $\hat{\mu}' = 0.095$ are shown, where the latter corresponds to the collision of the sticking zone and the 4^{th} attractor: $(m - 1 + \mu')/\hat{\alpha}^2 = m/\hat{P}$, with $m = 4$. Since domains of attraction are provided by cell mapping, one can clearly see which initial states lead to sticking zones (gray regions).

In order to explore the effect of varying $\hat{\mu}$, a parameter scan was carried out on $\hat{\mu} \in [0, 0.5]$. Attractor and fixed point positions (mean of x coordinates) are shown in Fig. 5.5, with coloured and gray dots, respectively. As the sticking zones around fixed points grow, they absorb chaotic attractors one after the other. In this particular case, all chaotic attractors are absorbed at $\hat{\mu} \approx 0.45$.

5.6 Main results

I have introduced the *hybrid-switching micro-chaos map* that describes the behavior of a PD-controlled inverted pendulum with sampling and dry friction. Without fricton, this system can have multiple separated chaotic attractors in its state space. By the generalisation of the micro chaos map, the effect of friction was analysed.
I have shown, that chaotic attractors can turn to chaotic repellers via a crisis event, when a chaotic attractors collides with a boundaries of a sticking zone. The conditions for this crisis were formulated. There is a wide range of parameters, where chaotic attractors coexist with sticking zones originating from dry friction.
Using the proposed methodology, other switching phenomena, e.g., impact, could be taken into account, as well.

> **Main Result 6: Hybrid-switching Micro-Chaos Map**
>
> The notion of *micro-chaos* can be generalized to incorporate switching events – e.g., related to dry friction or impact – which are independent from sampling. The map obtained this way is called *hybrid-switching micro-chaos map*.
> Chaotic attractors and sticking zones of friction force can coexist in the state-space of the hybrid-switching micro-chaos map, therefore it has been proven, that the *micro-chaos* phenomenon can persists in the presence of Coulomb-friction.

Related publications: [27, 30].

The practical relevance of this result is the fact, that it is possible to detect micro-chaos in measurements even in non-ideal circumstances, e.g., in the presence of unwanted Coulomb-friction. One attempt to experimentally detect micro-chaos was presented in [30], although the chaotic nature of the measured trajectories was not proven.

6

Epilogue

I have presented five chapters dealing with the history, description and analysis of micro-chaos. The new results are briefly summarized in the following paragraphs.

In Chapter 2 the *topological pattern* found in the state space of micro-chaos is presented and a formula for calculating the size of an *absorbing cuboid* is derived.

Chapter 3 introduced the *Clustered Simple Cell Mapping* method (an extension to the Simple Cell Mapping – SCM), which deals with joining separate SCM solutions, therefore allows adaptive expansion of the examined state space region and enables parallel execution.

In Chapter 4 the effect of twofold quantization was examined: the characterization of twofold quantization with the *quantization ratio*, and two new bifurcation phenomena: the *switching line collision* and the *deadzone crisis* were presented.

Chapter 5 explained the formulation of the *hybrid-switching micro-chaos map*, and showed that micro-chaotic oscillations can coexist with sticking zones caused by Coulomb-friction in the state space of this generalized micro-chaos map.

Lastly, I would like to express my gratitude towards the PhD program. It provided me a safe environment to push myself beyond my mental limits, widen my perspectives towards analytical mechanics, numerical methods, learning and education. It was fun at many times, but more importantly, it was fulfilling. I consider myself extremely lucky to have been given the opportunity to pursue a PhD at the Department of Applied Mechanics and be creative and open-minded during this time.

7

Brief summary of new results

Main Result 1: Topological pattern

An alternating pattern of chaotic attractors or transient chaotic repellors and fixed points is present in the state space of the digitally controlled 1 DoF mechanical oscillator if proportional-derivative control scheme is applied with sampling, zero-order-hold and quantized output. Depending on the parameters, border collision bifurcations of fixed points at the switching lines can change this pattern. Moreover, crisis bifurcations can turn attractors to repellors.

Main Result 2: Absorbing cuboid

An upper bound was given for the control error of the micro-chaos map, by re-formulating it as a stabilized system without quantization and with additional correction terms corresponding to the neglected fractional parts.
In case of output-quantization, the farthest possible point of the invariant set is expressed in the form:

$$\mathbf{y}_\infty = \lim_{j\to\infty} \sum_{k=0}^{j} \mathbf{S}^k \, \mathbf{b} \, \chi_k = \cdots = \begin{bmatrix} \sum_{k=0}^{\infty} \sigma_{1,k} \, \chi_k \\ \vdots \\ \sum_{k=0}^{\infty} \sigma_{n,k} \, \chi_k \end{bmatrix}.$$

The choice of the infinite sequence of fractional parts χ_k that maximize the i^{th} component of $\mathbf{y}_\infty$, is $\chi^i = \{\chi_0, \chi_1, \ldots, \chi_k, \ldots\} = \{\text{sign}(\sigma_{i,0}), \text{sign}(\sigma_{i,1}), \ldots, \text{sign}(\sigma_{i,k}), \ldots\}$, which yields a close upper bound to the control error.
This approach can be adapted to the case of input quantization, where multiple fractional part sets correspond to the quantization of state variables.
By taking the separately calculated maxima for each component of $\mathbf{y}_\infty$, an *absorbing cuboid* was expressed which can be used to provide an absorbing region in the state space. A practically usable algorithm was also developed for the determination of periodic orbits. This algorithm is based on a symbolic dynamics-based description of the phase-space and can be utilized to verify the control error estimation provided by the absorbing cuboid.

Main Result 3: Clustered Simple Cell Mapping

In order to adaptively discover state space objects with cell mapping approach, an extension to the Simple Cell Mapping (SCM) method was proposed. The Clustered Simple Cell Mapping method is the procedure of joining two Simple Cell Mapping solutions, thus creating a cluster of SCMs. Initially, two separate SCM solutions are present with non-overlapping and not necessarily adjacent domains of interest.
The procedure consists of two stages:

- The first stage updates transient cell sequences, which lead from one SCM domain to a known object in the other domain.
- The second stage examines cell sequences, which lead to the other domain, but to an unclassified state. The idea of *cell tree mapping* is used to discover new periodic groups situated at the boundary of the two SCM domains.

After the second stage, all cells either correspond to a known state space object or lead to the *reduced sink cell*, the state space region outside the cluster. A simple way to select an adjacent state space region to be added to the cluster is also described, enabling one to carry out Clustered SCM in an adaptive and automatic manner.
The computational effort of the method is linear in terms of the total number of cells.

Main Result 4: Quantization Ratio

Twofold quantization – when both the input and the output of the controller are quantized – can be characterised by the so-called *quantization ratio* parameter, corresponding to the ratio of input and output quantizers' resolution. Twofold quantization can be reduced to a single quantization case (input-only or output-only quantization) if an appropriate quantization ratio ρ is used and its limit $\rho \to 0$ is analysed.
It is impossible to analyse both kinds of twofold-to-single quantization transitions with a single quantization ratio, because parameter ρ appears in an integer-part function in the governing equations of the dynamical system. Consequently, the upper limit corresponding to one of the transitions is zero: $\lim_{\rho\to\infty} \rho \,\mathrm{Int}(x/\rho) = 0$, therefore, the control effort is turned off for finite values of x, where x is a linear combination of state variables.
Hence, two different quantization ratios are necessary to be used for the two transitions, and they are inversely proportional to each other: $\rho' \sim 1/\rho$.

Main Result 5: Switching Line Collision and Deadzone Crisis

In the case of twofold quantization – when both the input and the output of the controller are quantized – the state space of the controlled system can be divided into domains, each corresponding to a certain value of the control effort, separated by switching lines.
Two new bifurcation phenomena were introduced that can occur only in the case of twofold quantization:
- *Switching Line Collision* is the event, when piecewise smooth switching lines touch each other, that is, collide in the state space. This phenomenon can induce qualitative changes in the state space of continuous *flows*, but – since the trajectories of *maps* are allowed to "jump" in the phase-space – the effects of Switching Line Collision are less pronounced in the case of maps.
The condition of the existence of first order switching line collisions is provided for maps where the neighbouring switching lines are originating from twofold quantization and proportional-derivative (PD) control scheme. Conditions for the collision between any switching line and

its k-th neighbour were determined as well, along with critical quantization ratios which correspond to special cases, when all switching lines collide at all possible locations.
- *Deadzone Crisis* is an event, when a chaotic attractor turns to a transient chaotic repellor due to the change of the corresponding switching line's shape. The term *deadzone crisis* is originated from the observation, that this event is strongly related to the variation of input-deadzones in case of the 2D micro-chaos map. It was shown that this crisis event can strongly influence the maximal possible control error in the system. In some cases, even the increase of a resolution parameter r_{I} or r_{O} can lead to smaller control error.

Main Result 6: Hybrid-switching Micro-Chaos Map

The notion of *micro-chaos* can be generalized to incorporate switching events – e.g., related to dry friction or impact – which are independent from sampling. The map obtained this way is called *hybrid-switching micro-chaos map*.
Chaotic attractors and sticking zones of friction force can coexist in the state-space of the hybrid-switching micro-chaos map, therefore it has been proven, that the *micro-chaos* phenomenon can persists in the presence of Coulomb-friction.

Bibliography

[1] Aguirre, J., Viana, R. L., and Sanjuán, M. A. F. (2009). Fractal structures in nonlinear dynamics. *Rev. Mod. Phys*, 81:333–386.

[2] Berkolaiko, G. (1999). Dynamics of piecewise linear interval maps with hysteresis. *Dynamics and Stability of Systems*, 14(1):57–70.

[3] Budai, C., Kovács, L. L., Kövecses, J., and Stépán, G. (2017). Effect of dry friction on vibrations of sampled-data mechatronic systems. *Nonlinear Dynamics*, 88(1):349–361.

[4] Campbell, S. A., Crawford, S., and Morris, K. (2008). Friction and the Inverted Pendulum Stabilization Problem. *Journal of Dynamic Systems, Measurement, and Control*, 130(5):054502.

[5] Chen, Q., Ott, E., and Hurd, L. P. (1991). Calculating topological entropies of chaotic dynamical systems. *Physics Letters A*, 156(1):48 – 52.

[6] Csernák, G. (2016). Quantization-induced control error in a digitally controlled system. *Nonlinear Dynamics*, 85:2749–2763.

[7] Csernák, G., Gyebrószki, G., and Stépán, G. (2016). Multi-baker map as a model of digital PD control. *International Journal of Bifurcations and Chaos*, 26(2):1650023–11.

[8] Csernák, G. and Stépán, G. (2005). Life expectancy of transient microchaotic behaviour. *J. Nonlinear Science*, 15:63–91.

[9] Csernák, G. and Stépán, G. (2010). Digital control as source of chaotic behavior. *International Journal of Bifurcations and Chaos*, 5(20):1365–1378.

[10] Csernák, G. and Stépán, G. (2011). Sampling and round-off, as sources of chaos in PD-controlled systems. *Proceedings of the 19th Mediterranean Conference on Control and Automation*.

[11] Csernák, G. and Stépán, G. (2012). Disconnected chaotic attractors in digitally controlled linear systems. *Proceedings of the 8th WSEAS International Conference on Dynamical Systems and Control*, pages 97–102.

[12] Csernák, G. and Stépán, G. (2006). Quick estimation of escape rate with the help of fractal dimension. *Communications in Nonlinear Science and Numerical Simulation*, 11(5):595 – 605. Dynamical systems—theory and applications.

[13] Csernák, G. and Stépán, G. (2007). Life expectancy calculation of transient chaos in the 2d micro-chaos map. *Periodica Polytechnica Mechanical Engineering*, 51(2):59–62.

[14] Csernák, G. and Stépán, G. (2013). The state-space model of micro-chaos. *Proceedings of the 2013 International Conference on Systems, Control, Signal Processing and Informatics*, pages 420–425.

[15] Cvitanović, P., Artuso, R., Mainieri, R., Tanner, G., and Vattay, G. (2016). *Chaos: Classical and Quantum*. Niels Bohr Inst., Copenhagen.

[16] de Kraker, B., van der Spek, J. A. W., and van Campen, D. H. (2000). Extensions of cell mapping for discontinuous systems. In Wiercigroch, M. and de Kraker, B., editors, *Applied Nonlinear Dynamics and Chaos of Mechanical Systems with Discontinuities*, chapter 4, pages 61–102. World Scientific.

[17] Deimling, K. (1992). *Multivalued Differential Equations*. DE GRUYTER, Berlin, New York.

[18] Delchamps, F. D. (1990). Stabilizing a linear system with quantized state feedback. *IEEE Trans. Autom. Contr.*, 35:916–924.

[19] Devaney, R. (2003). *An Introduction to Chaotic Dynamical Systems*. Addison-Wesley, 1989, reprinted by Westview Press.

[20] Domokos, G. and Szász, D. (2003). Ulam's scheme revisited: digital modeling of chaotic attractors via micro-perturbations. *Discret. Contin. Dyn. Syst. Ser. A*, 9(4):859–876.

[21] Enikov, E. and Stepan, G. (1998). Microchaotic motion of digitally controlled machines. *Journal of Vibration and Control*, 4(4):427–443.

[22] Garay, B. M., Csikja, R., and Tóth, J. (2008). Some chaotic properties of the beta-hysteresis transformation. *Proc. of the 2008 International Symposium on Nonlinear Theory and its Applications, Budapest, Hungary*, pages 7–10.

[23] Gyebrószki, G. and Csernák, G. (2014). Methods for the quick analysis of micro-chaos. In Awrejcewicz, J., editor, *Applied Non-Linear Dynamical Systems*, chapter 28, pages 383–395. Springer International Publishing.

[24] Gyebrószki, G. and Csernák, G. (2017). Clustered simple cell mapping: An extension to the simple cell mapping method. *Communications in Nonlinear Science and Numerical Simulation*, 42:607–622.

[25] Gyebrószki, G. and Csernák, G. (2015). Digitális szabályozás okozta kaotikus rezgés amplitúdójának becslése. *XII. Magyar Mechanikai Konferencia, Miskolc, Magyarország*, 261:6.

[26] Gyebrószki, G. and Csernák, G. (2017). Inherent control error in a multi-pd controlled double inverted pendulum. *Proceedings of the 9th European Nonlinear Dynamics Conference, ENOC, Budapest University of Technology and Economics, Hungary*, pages 1–5.

[27] Gyebrószki, G. and Csernák, G. (2018a). The hybrid micro-chaos map: digitally controlled inverted pendulum with dry friction. *Periodica Polytechnica Mechanical Engineering*, accepted, in press:7.

[28] Gyebrószki, G. and Csernák, G. (2018b). Structures within the quantization noise: Micro-chaos in digitally controlled systems. *SYROCO 2018 - 12th IFAC Symposium on Robot Control, Budapest, Hungary*, 20:6.

[29] Gyebrószki, G. and Csernák, G. (2018c). Twofold quantization in digital control: dead-zone crisis and switching line collision. *Nonlinear Dynamics*, submitted, under review:16.

[30] Gyebrószki, G., Csernák, G., and Budai, C. (2014). Experimental investigation of micro-chaos. *Proceedings of the 8th European Nonlinear Dynamics Conference ENOC, Technische Universität, Wien*, pages 1–6.

[31] Góra, P. and Boyarsky, A. (1988). Why computers like lebesgue measure. *Computers & Mathematics with Applications*, 16(4):321 – 329.

[32] Góra, P. and Boyarsky, A. (1996). An algorithm to control chaotic behavior in one-dimensional maps. *Computers & Mathematics with Applications*, 31(6):13 – 22.

[33] Haller, G. and Stépán, G. (1996). Micro-chaos in digital control. *Journal of Nonlinear Science*, 6:415–448.

[34] Hegger, R., Kantz, H., and Schreiber, T. (1999). Practical implementation of nonlinear time series methods: The tisean package. *CHAOS*, 9:413.

[35] Hsu, C. (1987). *Cell-to-Cell Mapping: A Method of Global Analysis for Nonlinear Systems*, volume 64 of *Applied Mathematical Sciences*. Springer, Singapore.

[36] Insperger, T. and Milton, J. (2014). Sensory uncertainty and stick balancing at the fingertip. *Biological Cybernetics*, 108(1):85–101.

[37] Insperger, T., Milton, J., and Stepan, G. (2015). Semidiscretization for Time-Delayed Neural Balance Control. *SIAM Journal on Applied Dynamical Systems*, 14(3):1258–1277.

[38] Jabłoński, M., Góra, P., and Boyarsky, A. (1995). Invariant measures generated by sequences of approximating transformations. *Computers & Mathematics with Applications*, 30(7):75 – 91.

[39] Klages, R. (1996). *Deterministic diffusion in one-dimensional chaotic dynamical systems*. PhD thesis, TU Berlin.

[40] Kollár, L. E. (2001). *Dynamics of Digitally Controlled Unstable Mechanical Systems*. PhD thesis, Budapest University of Technology and Economics. PhD Thesis.

[41] Kruse, S. and Hoffmann, N. P. (2013). On the Robustness of Instabilities in Friction–Induced Vibration. *Journal of Vibration and Acoustics*, 135(6):061013.

[42] Lai, Y.-C. and Tél, T. (2011). *Transient Chaos*, volume 173 of *Applied Mathematical Sciences*. Springer New York, New York, NY.

[43] Lakshmikantham, V., Leela, S., and Martynyuk, A. A. (1990). *Practical Stability of Nonlinear Systems*. World Scientific, Singapore.

[44] Laurea, M. d. B., Champneys, A. R., Budd, C. J., and Kowalczyk, P., editors (2008). *Piecewise-smooth Dynamical Systems*, volume 163 of *Applied Mathematical Sciences*. Springer London, London.

[45] Milton, J., Insperger, T., Cook, W., Harris, D., and Stepan, G. (2018). Microchaos in human postural balance: Sensory dead zones and sampled time-delayed feedback. *Physical Review E*, 98(2):022223.

[46] Nusse, H. E. and Yorke, J. A. (1996). Basins of attraction. *Science*, 271:1376–1380.

[47] Nusse, H. E. and Yorke, J. A. (1998). *Dynamics: Numerical Explorations*, volume 101 of *Applied Mathematical Sciences*. Springer-Verlag, New York.

[48] Popp, K. and Stelter, P. (1990). Stick-Slip Vibrations and Chaos. *Philosophical Transactions of the Royal Society A: Mathematical, Physical and Engineering Sciences*.

[49] Stepan, G., Milton, J., and Insperger, T. (2017). Quantization improves stabilization of dynamical systems with delayed feedback. *CHAOS*, 27:114306.

[50] Sun, Z. and Ge, S. S. (2005). *Switched Linear Systems*. Communications and Control Engineering. Springer, London.

[51] van der Spek, J. A. W. (1994). *Cell Mapping Methods: Modifications and Extensions*. PhD thesis, Eindhoven University of Technology, Eindhoven. PhD Thesis.

[52] Widrow, B. and Kollár, I. (2008). *Quantization Noise: Roundoff Error in Digital Computation, Signal Processing, Control, and Communications*. Cambridge University Press, Cambridge, UK.

[53] Xiong, F.-R., Qin, Z.-C., Xue, Y., Schütze, O., Ding, Q., and Sun, J.-Q. (2014). Multi-objective optimal design of feedback controls for dynamical systems with hybrid simple cell mapping algorithm. *Communications in Nonlinear Science and Numerical Simulation*, 19(5):1465–1473.

[54] Xiong, F.-R., Schütze, O., Ding, Q., and Sun, J.-Q. (2016). Finding zeros of nonlinear functions using the hybrid parallel cell mapping method. *Communications in Nonlinear Science and Numerical Simulation*, 34:23–37.

[55] Zou, H. and Xu, J. (2009). Improved generalized cell mapping for global analysis of dynamical systems. *Science in China Series E: Technological Sciences*, 52(3):787–800.

Appendices

7.1 Appendix A: Complexity of Simple Cell Mapping

Algorithm 8 Simple Cell Mapping

Input: Cell State space
Output: SCM solution — Number of execution, cost

1: $g \leftarrow 0$
2: **for** $z \leftarrow 0, n$ **do** — $n+1, 1$
3: **if** $state[z] =$ UNTOUCHED **then**
4: $processing \leftarrow True$
5: $sequence \leftarrow \emptyset \cup z$
6: $im \leftarrow z$
7: **while** *processing* **do** — $\sum_{z=0}^{n-1} t_z, 1$
8: **if** $state[im] =$ PROCESSED **then**
9: Tag cells in sequence as processed and transient — $\sum_{z=0}^{n-1} 1, s_z$
10: $processing \leftarrow False$
11: **else if** $state[im] =$ UNDER_PROCESSING **then**
12: ▷ New periodic group and possibily some transients found — $\sum_{z=0}^{n-1} 1, s_z$
13: Examine sequence, starting with im and tag cells as periodic,
14: assign group g and step 0
15: Tag remaining cells as transient, assign $group \leftarrow g$
16: and calculate *step* numbers
17: $g \leftarrow g + 1$
18: $processing \leftarrow False$
19: **else**
20: ▷ $state[im] =$ UNTOUCHED, continue along the *image* track — $\sum_{z=0}^{n-1} t_z, 1$
21: $state[im] \leftarrow$ UNDER_PROCESSING
22: $sequence \leftarrow sequence \cup im$
23: $im \leftarrow image[im]$
24: **end if**
25: **end while**
26: **else**
27: ▷ Skip this cell
28: **end if**
29: **end for**

The number of times of execution and cost for some lines are denoted at line endings. The **for** loop is executed $n+1$ times, let t_z be the number of times the **while** loop is executed for that value of z. Let s_z be the length of the sequence accumulated starting with cell z. By examining the algorithm, one can see, that $s_z = t_z$, since no branches of the **if-else**

structure append new cell to the sequence or terminates the **while** loop at the same time. New cells are only appended to the sequence in line 22, while the processing of a sequence is either terminated at line 10 (reaching an already determined destination) or at line 18 (finding a new PG and transient cells). Therefore the cost of the algorithm is

$$C_{\mathrm{SCM}} = n\,c_1 + \sum_{z=0}^{n-1}(2\,s_z + t_z\,c_2) = (2 + c_1)\,n + \sum_{z=0}^{n-1} t_z\,c_2 = O(n),$$

where the sum of the length of sequences $\sum_{z=0}^{n-1} s_z = n$, c_1 is the total cost of constant-cost operations in the **for** loop outside the **while** loop, and c_2 is the total cost of constant-cost operations within the **while** loop.